

REPORT DOCUMENTATION PAGE			Form Approved OMB No. 0704-0188	
<small>Public reporting burden for this collection of information is estimated to average 1 hour per response, including the time for reviewing instructions, searching existing data sources, gathering and maintaining the data needed, and completing and reviewing the collection of information. Send comments regarding this burden estimate or any other aspect of this collection of information, including suggestions for reducing this burden, to Washington Headquarters Services, Directorate for Information Operations and Reports, 1215 Jefferson Davis Highway, Suite 1204, Arlington, VA 22202-4302, and to the Office of Management and Budget, Paperwork Reduction Project (0704-0188), Washington, DC 20503.</small>				
1. AGENCY USE ONLY (Leave blank)		2. REPORT DATE April 1996		3. REPORT TYPE AND DATES COVERED Final Technical 25 Sep 93 - 24 May 96
4. TITLE AND SUBTITLE (U) Influence of Supercritical Conditions on Precombustion Chemistry and Transport Behavior of Jet Fuels			5. FUNDING NUMBERS PE - 65502F PR - 3005 SA - SS C - F49620-93-C-0067	
6. AUTHOR(S) N. Zhou and A. Krishnan				
7. PERFORMING ORGANIZATION NAME(S) AND ADDRESS(ES) CFD Research Corporation 3325 Triana Boulevard Huntsville AL 35805			8. PERFORMING ORGANIZATION AFOSR-TR-96 0319	
9. SPONSORING/MONITORING AGENCY NAME(S) AND ADDRESS(ES) AFOSR/NA 110 Duncan Avenue, Suite B115 Bolling AFB DC 20332-0001 NA			AGENCY REPORT NUMBER 93-C-0067	
11. SUPPLEMENTARY NOTES				
12a. DISTRIBUTION/AVAILABILITY STATEMENT Approved for public release; distribution is unlimited			12b. DISTRIBUTION CODE 19960626 158	
13. ABSTRACT (Maximum 200 words) An experimental/computational approach to model precombustion chemistry and transport behavior for hydrocarbon fuels under supercritical conditions was developed. Models for the computation of thermophysical properties of real fluids were incorporated into a general purpose computational fluid dynamics (CFD) code. The models were applied to analyze heat transfer in supercritical fluids over a range of flow conditions from the laminar to turbulent regimes. The effects of turbulence and buoyancy were studied in detail. Advanced thermal stability models for jet fuels were incorporated into the code. Model predictions were compared with deposition data in the literature and with a concurrent experimental study. Experiments were performed at the University of Iowa and at Wright Laboratory using jet fuels and sulfur hexafluoride.				
14. SUBJECT TERMS aviation fuels, supercritical fluids, heat transfer, thermal stability, computational fluid dynamics (CFD)			15. NUMBER OF PAGES 174	
			16. PRICE CODE	
17. SECURITY CLASSIFICATION OF REPORT Unclassified	18. SECURITY CLASSIFICATION OF THIS PAGE Unclassified	19. SECURITY CLASSIFICATION OF ABSTRACT Unclassified	20. LIMITATION OF ABSTRACT UL	

CFD Research Corporation

3325 Triana Blvd. • Huntsville, Alabama 35805 • Tel.: (205) 536-6576 • FAX: (205) 536-6590 • info@cfdr.com



INFLUENCE OF SUPERCRITICAL CONDITIONS ON PRECOMBUSTION CHEMISTRY AND TRANSPORT BEHAVIOR OF JET FUELS

An SBIR Phase II Final Report

by

N. Zhou and A. Krishnan

April 1996

CFDRC Report: 4241/6

prepared for

**Air Force Office of Scientific Research
Aerospace and Engineering Sciences Department
110 Duncan Ave, Suite B115
Bolling AFB, DC 20332-0001**

AFOSR Contract Monitor: Dr. Julian Tishkoff

Contract Number: F49620-93-C-0067

R&D Services and Software for Computational Fluid Dynamics (CFD)

Branch Office: 2 Lakeview Ave., Suite 200 • Piscataway, New Jersey 08854 • Tel.: (908) 424-9393 FAX: (908) 424-9399

TABLE OF CONTENTS

	<u>Page</u>
ACKNOWLEDGEMENTS	xiii
1. INTRODUCTION	1
1.1 Significance of the Topic	1
1.2 The Thermodynamic Critical State	2
1.3 Property Variations near the Critical State	3
1.4 Studies of Heat Transfer near the Critical Point	4
1.5 Pressure Oscillations Associated with Boiling and Supercritical Heating	7
1.6 Predictive Capabilities for Supercritical Fluids/Flows	9
1.7 Proposed Phase II Program	10
1.8 Summary of Accomplishments	11
1.9 Summary of Current Report	14
2. DESCRIPTION OF MODELS	15
2.1 Governing Equations	15
2.2 Models for Thermophysical Properties	18
2.3 Models for Turbulence	23
2.4 Models for Thermal Stability of Fuels	28
3. EXPERIMENTAL DEPOSITION STUDIES WITH JET FUELS	33
3.1 Apparatus	33
3.2 Procedure	37
3.3 Results and Discussion	38
3.4 Summary	46
4. EXPERIMENTAL HEAT TRANSFER STUDIES WITH A SIMULANT FLUID	48
4.1 Use of a Simulant	48
4.2 Experimental Setup	48
4.3 Procedure and Test Conditions	50

TABLE OF CONTENTS (Continued)

	<u>Page</u>
4.4 Experimental Results	51
4.4.1 Fluid Exit Temperature	53
4.4.2 Tube Wall Temperature	54
4.4.3 Pressure Oscillations	58
5. VALIDATION OF MODEL FOR THERMOPHYSICAL PROPERTIES	60
5.1 Properties of Carbon Dioxide	60
5.2 Properties of Propane	63
5.3 Properties of JP-5	65
5.4 Properties of SF ₆	68
5.5 Summary	70
6. ASSESSMENT OF TURBULENCE MODELS	71
6.1 Comparison of Fluid Flow Predictions	71
6.2 Comparison of Heat Transfer Predictions	83
7. COMPUTATIONAL RESULTS FOR FLOW AND HEAT TRANSFER	86
7.1 Boundary Conditions	86
7.2 Results for Laminar Heat Transfer	87
7.3 Discussion of Laminar Heat Transfer Results	90
7.4 Results for Turbulent Heat Transfer	91
7.5 Discussion of Turbulent Heat Transfer Results	95
7.6 Non-Dimensional Analysis of the Problem	99
8. ASSESSMENT OF THE THERMAL STABILITY/DEPOSITION MODEL	103
8.1 Jet-A Experiments	103
8.2 JP-5 Experiments	104
8.3 Conclusions	105

TABLE OF CONTENTS (Continued)

	<u>Page</u>
9. BENCHMARK VALIDATION STUDY FOR THE DEPOSITION MODEL	110
9.1 Description of the Computational Model	110
9.2 Model Predictions and Comparisons with Data	112
9.3 Discussion of Results	117
10. BENCHMARK VALIDATION STUDY FOR HEAT TRANSFER MODEL	124
10.1 SF ₆ Experiments	124
10.2 Computational Results	124
11. COMPUTATIONAL RESULTS FROM THE LES STUDY	130
11.1 Problem Definition	130
11.2 Results from the LES Study	130
11.3 Discussion	137
12. CONCLUSIONS	138
12.1 Summary of Phase II Work	138
12.2 Plans for Future Work	139
12.3 Publications Resulting from the Phase II Study	139
12.4 Conclusions	141
13. REFERENCES	142
APPENDIX A - SURFACE DEPOSITION DATA	A-1
APPENDIX B - EXIT FILTER DEPOSITION DATA	B-1
APPENDIX C - WALL TEMPERATURE DATA	C-1

LIST OF ILLUSTRATIONS

	<u>Page</u>
Figure 1-1. Phase Diagram	2
Figure 1-2. Characteristics of Temperature Profiles for a Typical Boiling Process	5
Figure 3-1. Schematic of the Experimental Setup	34
Figure 3-2. Furnace Temperature Profile	36
Figure 3-3. Deposition Profile at Flowrate of 100 ml/min	39
Figure 3-4. Wall Temperature Profile at Flowrate 100 ml/min	39
Figure 3-5. Deposition Profiles at System Pressure 400 or 650 psig	41
Figure 3-6. Wall Temperature Profiles at System Pressure 400 or 650 psig	41
Figure 3-7. Deposition Profile at System Pressure 400 psig	42
Figure 3-8. Wall Temperature Profile at Flowrate 200 ml/min	42
Figure 3-9. Wall Temperature and Deposition Profile at Flowrate 300 ml/min	44
Figure 3-10. Surface Deposition as a Function of Test Duration (Furnace Temperature at 2192°F)	44
Figure 3-11. Exit Filter Deposition as a Function of Test Duration (Furnace Temperature at 2192°F)	47

LIST OF ILLUSTRATIONS (Continued)

	<u>Page</u>
Figure 3-12. Wall Temperatures as a Function of Test Duration, Experiment #7/94-1	47
Figure 4-1. Experimental Setup	49
Figure 4-2. Furnace Dimensions	49
Figure 4-3. Heat Transfer Rates	52
Figure 4-4. Bulk Fluid Temperature at Exit, Horizontal Flow, $Re = 10,000$	54
Figure 4-5. Tube Temperature near the Exit, $Re \approx 10,000$	56
Figure 4-6. Tube Temperature near the Exit, $Re \approx 2,000$	59
Figure 5-1a. Variation of Density with Temperature for CO_2	61
Figure 5-1b. Variation of Viscosity with Temperature for CO_2	61
Figure 5-1c. Variation of Conductivity with Temperature for CO_2	62
Figure 5-1d. Variation of Enthalpy with Temperature for CO_2	62
Figure 5-2a. Variation of Density with Temperature for Propane	63
Figure 5-2b. Variation of Viscosity with Temperature for Propane	64
Figure 5-2c. Variation of Conductivity with Temperature for Propane	64
Figure 5-2d. Variation of Enthalpy with Temperature for Propane	65

LIST OF ILLUSTRATIONS (Continued)

	<u>Page</u>
Figure 5-3a. Variation of Density with Temperature for JP-5	66
Figure 5-3b. Variation of Viscosity with Temperature for JP-5	66
Figure 5-3c. Variation of Conductivity with Temperature for JP-5	67
Figure 5-3d. Variation of Enthalpy with Temperature for JP-5	67
Figure 5-4a. Variation of Density with Temperature for SF ₆	68
Figure 5-4b. Variation of Viscosity with Temperature for SF ₆	69
Figure 5-4c. Variation of Thermal Conductivity with Temperature for SF ₆	69
Figure 5-4d. Variation of Enthalpy with Temperature for SF ₆	70
Figure 6-1. A Schematic of the Computational Domain	72
Figure 6-2. Variation of Mean Velocity Across the Channel	72
Figure 6-3. Variation of Mean Turbulent Kinetic Energy Across the Channel	73
Figure 6-4. Mean Turbulent Velocity as Function of Pipe Radius	74
Figure 6-5. Mean Turbulent Kinetic Energy as a Function of Pipe Radius	74
Figure 6-6. A Schematic of the Backward-Facing Step Flow	75
Figure 6-7. Static Pressure Variation Along the Step Wall	77

LIST OF ILLUSTRATIONS (Continued)

	<u>Page</u>
Figure 6-8. Variation of Skin Friction Coefficient Along the Wall	77
Figure 6-9. A Schematic of the Turn Around Duct Flow	78
Figure 6-10. Static Pressure Variation Along the Inner and Outer Walls	78
Figure 6-11. Mean Turbulent Velocity Profile at	79
Figure 6-12. Mean Turbulent Velocity Profile at 90	79
Figure 6-13. Mean Turbulent Velocity Profile at 180	80
Figure 6-15. Axial Variation of radial Velocity	82
Figure 6-16. Axial variation of Tangential Velocity	82
Figure 6-17a. Comparison of Heat Flux Predictions from the Three Turbulence Models for Upward Flow in the 2-D channel with $T_w = 320^\circ\text{K}$	85
Figure 6-17b. Comparison of Heat Flux Predictions from the Three Turbulence Models for Upward Flow in the 2-D Channel with $q_w = 30\text{KW}/\text{M}^2$	85
Figure 7-1. Computational Geometry and Grid for the 2-D Channel Flow Problem	87
Figure 7-2. Predicted Profiles of Density, Velocity and Temperature in Channel for the Upward Flow ($\text{Re} = 1,000$)	89
Figure 7-3. Predicted Profiles of Density, Velocity and Temperature in the Channel for the Downward Flow ($\text{Re} = 10,000$)	89

LIST OF ILLUSTRATIONS (Continued)

Page

Figure 7-4.	Local Heat Flux Along the Channel Wall for the Upward Flow, the Downward Flow and the No-Gravity Case ($Re = 10,000$)	90
Figure 7-5.	Comparison of Measured and Predicted Heat Flux Values for Free Convection of Supercritical CO_2	91
Figure 7-6.	Comparison of Predictions of Heat Flux from Laminar and Turbulent Flow Models for $Re = 10,000$	93
Figure 7-7.	Turbulent Heat Flux Prediction Along Channel Wall at $Re = 100,000$	93
Figure 7-8a.	Comparison of Mean Velocity Profiles for the Upward Flow and the No-Gravity Cases for $Re = 100,000$	94
Figure 7-8b.	Comparison of Mean Velocity Profiles for the Downward Flow and No-Gravity Cases for $Re = 100,000$	94
Figure 7-9a.	Comparison of Turbulent Viscosity Profiles for the Upward Flow and No-Gravity Cases for $Re = 100,000$	96
Figure 7-9b.	Comparison of Turbulent Viscosity Profiles for the Downward Flow and No-Gravity Cases for $Re = 100,000$	96
Figure 7-10a.	Comparison of Temperature Profiles for the Upward Flow and No-Gravity Cases for $Re = 100,000$	97
Figure 7-10b.	Comparison of Temperature Profile for the Downward Flow and No-Gravity Cases for $Re = 100,000$	97

LIST OF ILLUSTRATIONS (Continued)

	<u>Page</u>
Figure 7-11a. Measured and Predicted Wall Temperatures in Pipe Flow of CO ₂	98
Figure 7-11b. Measured and Predicted Wall Temperatures in Pipe Flow of CO ₂	98
Figure 7-12. Predicted Heat Flux Values Along the Channel Wall for Re = 1,000,000	101
Figure 7-13. Illustration of the Coupling between Various Physical Phenomena	102
Figure 8-1a. Deposition Rate Distribution Along the Tube	106
Figure 8-1b. Species Concentration Distribution Along the Tube	106
Figure 8-2. Predicted and Measured Deposition in Near-Isothermal (458K) Heated Tube Experiment Using Two Different Bore Sizes	107
Figure 8-3a. Deposition Rate Distribution Along the Tube	108
Figure 8-3b. Wall Temperature Distributions Along the Tube	108
Figure 8-4a. Wall and Bulk Temperature Distributions Along the Tube	109
Figure 8-4b. Deposition Rate as a Function of Wall Temperature for Different Chemistry Models	109
Figure 9-1. Schematic of Furnace and Tube Geometry	111

LIST OF ILLUSTRATIONS (Continued)

	<u>Page</u>
Figure 9-2a. Predicted Wall Temperature for the (75x64) Grid and the(120x40) Grid	113
Figure 9-2b. Predicted Deposition Rates for the (75x64) Grid and the (120x90) Grid	113
Figure 9-3a. Comparison of Predicted Wall Temperatures for Case 7/94-6 with Data	114
Figure 9-3b. Predicted Deposition Rates for Case 7/94-6 with Data	114
Figure 9-4a. Predicted Wall Temperatures for Case 7/94-10	115
Figure 9-4b. Predicted Deposition Rates of Case 7/94-10	115
Figure 9-5a. Predicted Wall Temperatures for Case 7/94-2	116
Figure 9-5b. Predicted Deposition Rates for Case 7/94-2	116
Figure 9-6a. Wall/Bulk Fluid Temperatures Along the Tube	119
Figure 9-6b. Deposition Rate Along the Tube	119
Figure 9-7. Results for $q_w = 200 \text{ kW/m}^2$	120
Figure 9-8. Results for $q_w = 300 \text{ kW/m}^2$	121
Figure 9-9. Results for $q_w = 400 \text{ kW/m}^2$	122
Figure 9-10. Computational Results with 3 Different Surface Reaction Models	123

LIST OF ILLUSTRATIONS (Continued)

	<u>Page</u>
Figure 10-1. Schematic of Numerical Problem	126
Figure 10-2. Results for $p = 400$ psia and $Q = 150$ ml/min	126
Figure 10-3. Results for $p = 531$ psia and $Q = 150$ ml/min	127
Figure 10-4. Results for $p = 700$ psia and $Q = 150$ ml/min	127
Figure 10-5. Results for $p = 400$ psia and $Q = 450$ ml/min	128
Figure 10-6. Results for $p = 531$ psia and $Q = 450$ ml/min	128
Figure 10-7. Results for $p = 700$ psia and $Q = 450$ ml/min	129
Figure 11-1a. Schematic of the Problem	131
Figure 11-1b. Computational Grid (100x60) for the Problem	131
Figure 11-1c. Schematic of Monitoring Locations	131
Figure 11-2. Predictions of Heat Flux Along the Heated Wall of the Channel	133
Figure 11-3a. Temperature Distribution in the Channel	134
Figure 11-3b. Magnified View of Temperature Distribution Near the Heated Wall	134
Figure 11-4a. Density Distribution in the Channel	135
Figure 11-4b. Magnified View of Density Distribution Near the Heated Wall	135

LIST OF ILLUSTRATIONS (Continued)

	<u>Page</u>
Figure 11-5a. Transient Temperature Behavior at Locations (1, 2, and 3) 1 mm Above the Heated Wall	136
Figure 11-5b. Transient Temperature Behavior at Locations (4, 5, and 6) 0.1 cm Above the Heated Wall	136
Figure 11-5c. Transient Temperature Behavior at Locations (7, 8 and 9) 0.2 cm Above the Heated Wall	137

ACKNOWLEDGEMENTS

This project was a Phase II SBIR study (of two year duration) sponsored by the Air Force Office of Scientific Research (AFOSR). The authors thank Dr. Julian Tishkoff, the project monitor, for his support of this work.

The authors would also like to thank Dr. Mel Roquemore and Dr. Tim Edwards of Wright Laboratory for their guidance during the course of this work. All of the experimental work presented in this report were done by Dr. L.D. Chen and Mr. John Krieger of the University of Iowa. The assistance of Dr. Vish Katta of ISSI was valuable in the implementation of models for thermal stability of fuels. Dr. Ram Avva of CFDRC performed the assessment of turbulence flow models for application to supercritical fluids. Dr. M. Giridharan of CFDRC conducted extensive analysis in determining the validity of wall functions for supercritical fluid flows. Dr. Andrzej Przekwas, Vice President/Research of CFDRC, and Dr. Ashok Singhal, President & Technical Director of CFDRC, provided in-house guidance on the project. Finally, the authors would like to acknowledge the effort of Ms. J. Swann in preparing the necessary reports for this project.

1. INTRODUCTION

This report documents the work performed under a Phase II SBIR study (of 2 year duration) sponsored by AFOSR. The objective of the overall project (Phases I and II) is to develop an experimental/computational approach to model precombustion chemistry and transport behavior of hydrocarbons under supercritical conditions.

The model development and computations were performed at CFDRC and the parallel experimental effort was conducted by Prof. L.D. Chen at the University of Iowa (under a subcontract from CFDRC). The purpose of this report is to provide a recapitulation of the project objectives, overview of the technical approach and a detailed description of the progress made during the study.

1.1 Significance of the Topic

Modern military aircraft employ fuel as the primary heat sink medium for heat loads arising from sources such as the engine, the avionics, the environmental control system, and the air frame. It is expected that advances in engine technology for high performance aircraft are going to further increase the heat loads on the fuel. The increase in fuel temperature due to heating has several consequences. Some of these are:

- a. Current hydrocarbon fuels have a practical temperature limit beyond which the fuel will chemically decompose to form gums and insolubles that stick to fuel lines and valves. The fouling of heat exchangers and fuel nozzles can cause serious problems in the fuel system [1,2].
- b. Pressures in current fuel systems are generally above the critical pressure of the fuel. Large heat loads can cause the fuel temperature to increase beyond the critical temperature of the fuel. This necessitates the operation of the fuel in the supercritical regime. The supercritical properties of substances are not well understood. Thermophysical properties such as density, conductivity, viscosity and specific heat undergo large variations near the critical point. Furthermore, the understanding of fuel stability under supercritical conditions is almost nonexistent [3].

Therefore, efficient heat management in high performance aircraft will require good understanding of the transport and chemical properties of the fuel under supercritical conditions.

1.2 The Thermodynamic Critical State

The state of a simple, compressible substance can be determined by specifying two state variables--pressure and temperature, for example. For any such substance, the choice of these two variables determines its state (e.g., solid, liquid, or gas). The solid state is distinct from the two fluid states in that the substance maintains a constant shape (does not deform continuously when subjected to a shear stress). The transition from a solid to a fluid is marked by the loss of this property. At low pressures, the transition from one fluid state to the other is marked by a discontinuous change in properties at the boiling point. At high pressures, however, there is no distinct transition from a liquid to a gas, and properties vary continuously from one to the other. The relationship between pressure, temperature, and state for a typical substance (that contracts on freezing) is shown graphically in Figure 1-1.

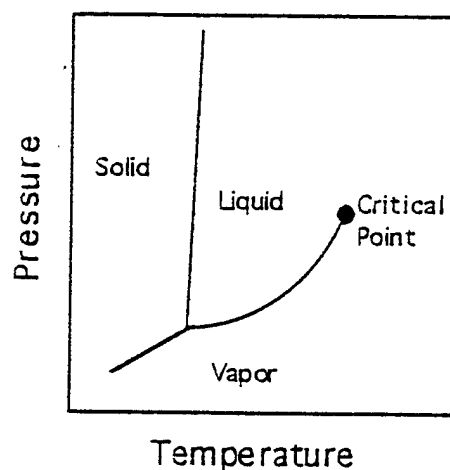


Figure 1-1. Phase Diagram

At low pressures, increasing the temperature of a liquid will cause it to boil at a certain temperature, known as the saturation temperature (T_{sat}). This process involves a discontinuous change of state from a liquid to a gas, with the accompanying discontinuous change in properties. As the pressure is increased, the boiling point increases also, and the difference between the properties of the liquid and gas becomes smaller. At a certain pressure, the boiling point reaches a maximum, and the difference between the properties of the liquid and gas becomes zero. At this pressure and temperature, the substance is in the critical state. At pressures higher than the critical pressure, boiling does not exist, and increasing temperature produces rapid, but continuous, property changes.

When dealing with near-critical fluids, state variables are commonly stated in relation to the critical point. The ratio of a property at a given state to the same property at the critical state is known as the reduced property. Also, supercritical means having a pressure greater than the critical pressure and a temperature greater than the critical temperature, or a reduced pressure and temperature greater than one, and subcritical means having a pressure less than the critical pressure and a temperature less than the critical temperature, or a reduced pressure and temperature less than one. Near-critical is taken to mean having a reduced pressure and temperature slightly greater or slightly less than one.

1.3 Property Variations near the Critical State

The most significant aspect of dealing with near-critical fluids is the fact that the thermodynamic and transport properties vary rapidly with temperature [4]. (Properties vary with pressure also, but in practical situations, variation due to pressure gradients is typically very small compared to variation due to temperature gradients.) Some properties can even become infinite exactly at the critical point. For example, density, thermal conductivity, and viscosity all decrease with increasing temperature, decreasing most rapidly near the critical point. Experimental work has revealed an anomaly in the thermal conductivity, however. Investigations involving many different fluids have revealed a large spike in the thermal conductivity near the critical point [5]. The specific heat at constant pressure also shows a large spike at near-critical conditions, becoming infinite exactly at the critical point. This infinity can be compared to the infinite specific heat

(slope of enthalpy vs. temperature) at subcritical boiling points. The supercritical temperature at which the specific heat is a maximum is known as the pseudocritical temperature (T_{pc}), similar to the subcritical boiling point. In addition to large property variations, another important aspect of near-critical fluids is that surface tension is very small at high subcritical pressures, and absent at supercritical pressures.

A central property of concern in fluid flow problems is specific enthalpy, defined as specific internal energy plus the product of pressure and specific volume. This is important because it accounts for flow work. If all other variations in energy (e.g. kinetic, gravitational, potential) are negligible, the variation in enthalpy of a fluid will simply equal the heat transfer to the fluid. In this case, the enthalpy at any point in an internal flow process will equal the enthalpy at the inlet plus the heat added between the inlet and the point in question.

1.4 Studies of Heat Transfer near the Critical Point

The majority of investigations of near-critical heat transfer phenomena have been concerned with flow through heated pipes. This type of flow is not necessarily forced convection, since it has been determined that buoyancy effects can play a large role in near-critical heat transfer (see e.g. [6]). Thus data on near-critical heat transfer are more properly separated into two categories: purely forced convection and mixed convection. For large flow rates in small pipes, buoyancy forces are negligible, and forced convection occurs. For larger pipes or lower flow rates, buoyancy forces begin to have a significant effect, and mixed convection occurs.

Hall and Jackson [6] cite several proposed criteria for determining whether or not buoyancy effects are important. They also note that all of the criteria possess the form of a ratio of Grashof number over Reynolds number. The Grashof number represents a comparison of buoyancy forces to viscous forces, and the Reynolds number represents a comparison of inertia forces to viscous forces. Thus the ratio represents a comparison of buoyancy forces to inertia forces. In a more recent publication, Polyakov [7] presents a more elaborate criterion, which compares the Grashof number, Reynolds number, and a number which accounts for thermal acceleration effects.

When buoyancy forces are negligible, the flow does not depend on the orientation with respect to gravity. In this relatively simple case, the heat transfer characteristics are perhaps easiest to understand. Heat transfer at near-critical conditions has been regarded as a region where boiling and convection merge [4]. Some aspects of near-critical forced convection may be understood by examining what happens as the critical pressure is approached from either side.

At highly subcritical pressure, the flowing fluid will change from liquid to vapor by passing through the well-known regimes of nucleate boiling, annular flow, and will eventually reach dryout. This is illustrated in Figure 1-2, which shows a simplified sketch of fluid and tube wall temperatures for a typical flow boiling process (constant heat flux, vertical flow) well below the critical point [8]. In the initial single-phase region, the two temperatures rise steadily with each other. As the liquid begins to boil, however, the wall temperature begins to decrease, while the fluid temperature remains constant at the boiling point. The wall temperature continues to decrease through the nucleate boiling and annular flow regimes. When annular flow dryout occurs, the wall temperature jumps sharply. When all of the liquid has evaporated, and the flow again enters single phase convection, the two temperatures rise steadily again.

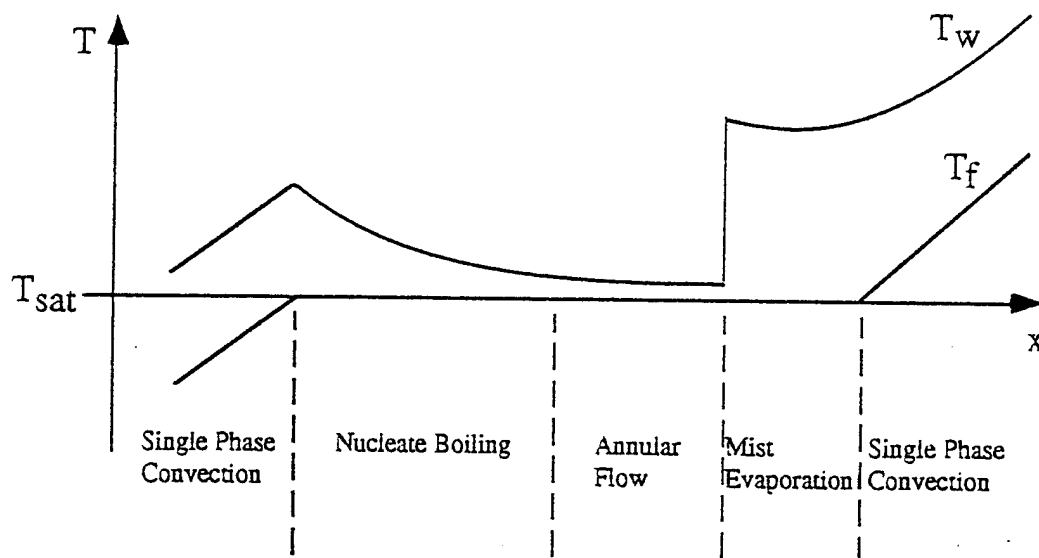


Figure 1-2. Characteristics of Temperature Profiles for a Typical Boiling Process

Single phase forced convection data are usually correlated in terms of a heat transfer coefficient. The validity of a heat transfer coefficient for fluids with widely varying properties has been questioned, however [6,9]. Increasing heat flux would increase the temperature gradient, and thus the property variation, within the boundary layer, affecting the heat transfer. Thus the heat transfer coefficient becomes a function of heat flux. The concept has nonetheless been widely used.

One feature of supercritical convection is that, in contrast to subcritical boiling, there is no heat transfer crisis. Another is that the heat transfer coefficient increases when the wall temperature is above the pseudocritical temperature, and the bulk fluid temperature is slightly below. Hall and Jackson [6] demonstrate that for fixed flow conditions and low heat fluxes (small property variations), the heat transfer coefficient will depend primarily on the specific heat of the fluid. If the fluid is near the pseudocritical temperature, where there is a peak in the specific heat, the heat transfer coefficient should have a peak also. Hall and Jackson also cite data showing that this is the case. However, the peak in the heat transfer coefficient decreases with increasing heat flux, which is consistent with a contracting layer of high specific heat fluid. Supercritical convection becomes much more complicated at higher heat fluxes, when variations in viscosity and thermal conductivity affect the flow and heat transfer processes.

Thus near-critical heat transfer in the absence of buoyancy effects seems to be a cross between film boiling and boundary layer flow with large property variations in the boundary layer. Heat transfer becomes more complicated when buoyancy forces begin to have a significant effect, and mixed convection occurs. In this case, one might expect heat transfer to be improved in upward flow, and degraded in downward flow, but in fact the opposite is true. A characteristic feature of buoyancy affected upward flow is increased wall temperatures, and a phenomenon known as the inlet wall temperature peak, in which the tube surface temperature near the inlet exhibits a sharp peak. Data also indicate a continuous improvement in heat transfer in buoyancy affected downward flow as buoyancy forces become progressively stronger [6].

A recent study by Kurganov and Kaptilnyi [10] has shed some light on these phenomena. Detailed measurements were made of velocity and temperature

profiles across a vertical tube under conditions of forced and mixed convection. For forced convection and downward mixed convection, the flow has the usual convex shape. For upward mixed convection, however, the flow develops an M-shaped velocity profile. There is a thin layer of low density, low viscosity fluid against the wall, which moves much more rapidly than the core of higher density fluid. As the flow progresses, the core temperature increases, and the M-shape smears out. It is the initial development of this M-shaped profile near the inlet which causes the temperature peak. It was concluded that the reduction or enhancement of turbulent transport plays a large role in buoyancy affected flows.

The effect of buoyancy in horizontal flow is to make the top of the tube hotter than the bottom. Experiments under these circumstances thus require temperature measurements around the perimeter of the tube to be useful.

1.5 Pressure Oscillations Associated with Boiling and Supercritical Heating

Experimental work on heat transfer to supercritical fluids has been proceeding for several decades, and a somewhat frequent occurrence is the phenomenon of thermo-acoustic oscillations [11]. These oscillations are characterized by large amplitude oscillations in fluid pressure, which are strong enough to be audible, and to sometimes fracture or even rupture the tubing. Most observed instances occur in forced flow, but they have been observed in free convection also. Pressure oscillations have been reported for internal flow conditions for a wide range of fluids, including hydrogen, helium, hydrocarbon fuels, and water.

The conditions under which these oscillations occur seem to be extremely high heat fluxes and that the pseudocritical temperature lie between the bulk fluid temperature and the wall temperature of the pipe. The oscillations have also been observed in a few instances of subcritical boiling [12], in which case the boiling point fell between the bulk fluid temperature and the tube wall temperature. These considerations seem to imply that the oscillations are associated with rapid property (or phase) change of the fluid near the wall.

The observed frequencies vary widely depending on experimental conditions, from fractions of Hertz to thousands of Hertz. Also, most researchers report improved

heat transfer accompanying the oscillations. Goldmann [9], for example, reports that oscillations in supercritical water were accompanied by a decrease in tube wall temperatures, indicating improved heat transfer. Hines and Wolf [13] also report increased heat transfer accompanying pressure oscillations.

Several attempts have been made to explain this phenomenon. In a 1961 paper [9] Goldmann pictured packets of dense, liquid-like fluid exploding into vapor-like fluid upon coming into contact with the wall, agitating the liquid-like core, and causing more packets to contact the wall, Malkina et. al. [14] described a process in which vapor or vapor-like bubbles depart from the wall and collapse again in the cooler space of the core. It seems likely at this point that the oscillations are due to resonance of acoustic waves in the pipes. Some experimental work such as that of Hines and Wolf [13], indicate that this is not the case, but there seems to be a large and growing body of work indicating that it is.

Stewart et al. [11], have written a paper in which they conduct a brief literature review concerning pressure oscillations before going on to describe their own experiments aimed specifically at studying this phenomenon. They first cite a study involving free convection in a vertical heated pipe which was part of a closed circulation loop. By varying the bulk fluid temperature (and thus the speed of sound), or the total length of the loop, and observing the resulting frequency of oscillation, the researchers found that the oscillations were consistent with standing pressure waves resonating in the loop. From their own experiments with supercritical water, Stewart et al. conclude that the pressure oscillations were due to longitudinal acoustic waves standing in the test section. Their experimental setup had voids in the flanges at both ends of the test section, and the acoustic waves were consistent with open-open pipe resonance. The researchers also calculate that the heat transfer coefficient is a minimum at locations where the pressure fluctuation is maximum, and the coefficient is a maximum at locations where the pressure fluctuation is a minimum. This may explain the discrepancy among previous reports of improved or degraded heat transfer. They also attribute the driving force behind the oscillations to alternating compression and expansion of the thin vapor-like layer adjacent to the wall, producing a net work output. The results of this work [11] are very encouraging, but still do not explain the full range of observed cases of thermo-acoustic oscillations.

A recent, very brief report by Kalbaliev and Verdiev [15] describes the results of tests performed with supercritical toluene. Correlations are given for heat transfer, wall temperature, and conditions for the onset of pressure oscillations, but no discussion is given on the applicability of these correlations to other fluids or flow conditions.

1.6 Predictive Capabilities for Supercritical Fluids/Flows

The efficiency of using fuel as an onboard coolant in military aircraft will depend on the heat transfer and chemical characteristics of the fuel. These phenomena, in turn, depend on the thermophysical properties of the fluid. It has already been emphasized that thermophysical properties undergo steep variations near the critical point. These variations are expected to significantly alter local heat transfer rates. Therefore, conventional heat transfer correlations, based on the assumption of uniform transport properties, will not be valid for supercritical environments. The use of ideal gas models for computing density and specific heat is not appropriate for the high pressure conditions in supercritical flows. Also, it is not clear how the mutual interactions between these properties will affect the overall transport process.

Experimentation with supercritical fluids has provided understanding on certain global aspects of the transport process. However, even the most detailed and sophisticated experiments are unable to provide knowledge of local effects and interactions in supercritical flows. Also, most experiments are done in simple configurations while the applications of these flows involve complex geometrical effects such as those encountered in heat exchanger coils, valves, etc. However, it is possible to account for these complex effects through the development of advanced models. The great advantage of modeling is that detailed parametric studies can be performed at a fraction of the time and cost associated with hardware experimentation. The model should possess the following features in order to be of practical utility in designing cooling systems for aircraft:

- a. The model should calculate all thermophysical properties locally as a function of pressure, temperature and composition. These properties should be input into a general purpose transport equation solver in order to account for mutual interactions between these effects.

- b. The transport equation solver should be able to account for complex geometrical effects. Flows through heat exchanger coils, fuel lines, nozzles and valves should be modeled efficiently and accurately.
- c. Additional complexities such as flow turbulence and chemical decomposition of the fuel should be modeled.
- d. The supercritical models and the transport equation solver should be validated against benchmark experiments.

A model with the above mentioned features will be a valuable tool in improving existing designs and developing new optimal designs for aircraft cooling systems.

1.7 Proposed Phase II Program

The main objective of the Phase II program is to produce an experimentally validated computational tool for designing heat management systems for high performance aircraft. The following developments and improvements were proposed for the Phase II study.

- a. **Computational Model Development:** The supercritical transport models developed during Phase I will be extended to include a range of hydrocarbon fuels. The models will then be incorporated into a multi dimensional, multi-block, time accurate CFD code.
- b. **LES Model Incorporation:** An LES model will be used to address issues of turbulence and unsteadiness in supercritical flows.
- c. **Chemistry Model Incorporation:** The chemistry models developed at Wright Laboratory (for studying thermal stability of fuels) will be incorporated into the code. These models will be further calibrated and refined for high pressure conditions based on data obtained during this program.
- d. **Experimental Testing:** Benchmark heat transfer experiments will be performed at the University of Iowa and Wright Laboratory. The

experiments at the University of Iowa will involve the use of a simulant fluid such as SF_6 while those at Wright Lab will involve experimentation with hydrocarbon fuels.

- e. **Validation and Parametric Studies:** After the code has been satisfactorily validated, it will be used to conduct a series of parametric studies to assess effects of various operating and boundary conditions on the transport process.
- f. **Customization/Documentation/Packaging of the Code:** The software capability developed in Phase II will be customized and packaged for design analysis studies. Detailed documentation will be provided for usage of the code along with technical descriptions of the models.

1.8 Summary of Accomplishments

The following tasks have been completed during the Phase II study and are discussed in greater detail in the following sections of this report:

1. Detailed validation studies were performed to assess the accuracy of the transport models developed in Phase I. Properties such as viscosity, conductivity, density and enthalpy were computed (as a function of temperature and pressure) for propane, carbon dioxide, JP-5 and SF_6 under sub-critical, critical and supercritical conditions. Good agreement was obtained with data over a range of pressure and temperature in the near critical regime. The models for thermophysical properties were incorporated into CFDR's general purpose Computational Fluid Dynamics code, CFD-ACE.
2. The transport model was applied to compute flow and heat transfer in generic engineering configurations for which reliable data was available. The following cases were considered:
 - (i) Laminar free convection flow of supercritical carbon dioxide over a flat plate.

- (ii) Laminar forced convection flow of supercritical carbon dioxide for a jet impinging on a flat plate.

The predicted heat transfer rates agreed well with experimental data and theoretical results for the above cases.

3. The two layer k - ϵ model for turbulence was incorporated into the code. It was tested on a number of benchmark problems (for incompressible flows) and the results were compared with those predicted by the standard k - ϵ model. The mean velocity profiles, turbulent kinetic energy, pressure coefficients and skin friction coefficients predicted by both models were in close agreement for all the cases considered.
4. The low Reynolds number k - ϵ model was used successfully to model heat transfer and chemistry in supercritical fluids. However, a few advanced features had to be incorporated into this model to account for steep property variations in the fluid. An advanced correlation was used to calculate the local turbulent Prandtl number to account for the "bursting" phenomenon observed in the sublayer. With this addition, the low Reynolds number model was able to resolve experimental features that could not be modeled using the standard k - ϵ model.
5. The two-layer k - ϵ model was tested for heat transfer applications. Its predictions were found to be less accurate than those of the standard k - ϵ model and the low Reynolds number model. This was mainly due to the lack of an appropriate heat transfer analog (of the momentum transfer model) for the two-layer model.
6. The models were used to simulate laminar and turbulent heat transfer in channel flows and tube flows in the supercritical regime. The simulations were done for carbon dioxide since a large amount of experimental data exists for the flow and heat transfer characteristics of supercritical CO_2 . The importance of buoyancy in influencing local heat transfer rates was investigated. The results predicted by the model were found to be in good

quantitative agreement with existing data. A detailed parametric study was conducted over a range of Reynolds and Grashof numbers to determine the effects of natural convection.

7. Experiments were performed at the University of Iowa (under the supervision of Prof. L.D. Chen) using SF_6 as a surrogate fuel. During the summer months (June to August, 1994), experiments were also performed at Wright Laboratory to obtain deposition data on fuels. This data was used for validation studies of the computational models developed during the Phase II program.
8. The Krazinski model for the auto-oxidation of fuel was incorporated into the code. The results predicted by the model were in agreement with data obtained by Marteney and Spadaccini as well as predictions by Krazinski et al.
9. Advanced multi-step models for thermal stability of hydrocarbon fuels (developed at Wright Laboratory) were incorporated into the code. In particular, a 9-step model (consisting of 6 gas phase and 3 surface reactions) developed at Wright Laboratory was used in the simulations. The model predictions of wall temperature and deposition rate were compared with data. Good agreement was observed between the model predictions and measured data.
10. Large Eddy Simulations (LES) of the flow of SF_6 in a rectangular channel was done to resolve the inherent unsteadiness (if any) in the flow of supercritical fluids. Results showed that unsteady behavior (induced solely by gravity) was present only for low Reynolds number flows and horizontal flow configurations. For higher Re and upward/downward flow configurations, the model converged to a steady state solution.
11. Heat transfer experiments were performed at the University of Iowa using supercritical SF_6 as a simulant fluid. Wall temperatures and exit fluid temperatures were measured for various flow rates and furnace temperatures corresponding to conditions ranging from the sub-critical state to the supercritical state.

12. The SF_6 heat transfer experiments were simulated using the computational model. Good agreement was obtained over a range of conditions.

The details of the above tasks are discussed in this report.

1.9 Summary of Current Report

Section 2 describes the models and the governing equations. Sections 3 and 4 describe the experimental work performed (at the University of Iowa and Wright Laboratory) during this study. Section 5 presents the results for the validation of the models for thermophysical properties. The validity of different turbulence models for application to supercritical fluid flow is discussed in Section 6. Section 7 presents the results for flow and heat transfer for supercritical CO_2 in the laminar and turbulent regimes. The thermal stability models for aviation fuels are assessed for generality and accuracy and the results are described in Section 8. The benchmark validation study of the models for wall deposition is described in Section 9. The results from the benchmark validation study for flow and heat transfer of SF_6 in a tube are discussed in Section 10. Section 11 presents the results for the LES study of supercritical SF_6 in a channel. Section 12 concludes with the summary of the Phase II work and describes plans for future work.

2. DESCRIPTION OF MODELS

This section describes the governing equations, the models for thermophysical properties of supercritical fluids flow, turbulence and thermal stability of aviation fuels.

2.1 Governing Equations

The governing equations for the flow, heat transfer and chemistry of supercritical fluids are as follows [16]:

Mass Conservation:

$$\frac{d\rho}{dt} + \nabla \cdot \rho \mathbf{u} = 0 \quad (1)$$

where ρ is the fluid density and \mathbf{u} the velocity vector.

Momentum Conservation:

$$\frac{d\rho \mathbf{u}}{dt} + \nabla \cdot \rho \mathbf{u} \mathbf{u} = -\nabla p + \nabla \cdot \boldsymbol{\tau} + \rho \mathbf{g} \quad (2)$$

$$\boldsymbol{\tau} = \mu_{\text{eff}} \left(\nabla \mathbf{u} + \nabla \mathbf{u}^T - \frac{2}{3} \nabla \cdot \mathbf{u} \mathbf{I} \right)$$

where

$$\mu_{\text{eff}} = \mu + \mu_t \quad (3)$$

where p is the hydrodynamic pressure, μ the dynamic viscosity, and \mathbf{g} the gravity vector. μ_t is the turbulent viscosity computed from the turbulence model and \mathbf{I} is the unit tensor.

Energy Conservation:

$$\frac{\partial \rho h}{\partial t} + \nabla \cdot \rho \mathbf{u} h = \nabla \cdot \lambda_{\text{eff}} \nabla T + \frac{dp}{dt} + \boldsymbol{\tau} : \nabla \mathbf{u} \quad (4)$$

where

$$\lambda_{\text{eff}} = \lambda + \lambda_t \quad (5)$$

where h is the static enthalpy, λ the thermal conductivity, and $\boldsymbol{\tau}$ the shear stress tensor. λ_t is the turbulent conductivity computed from μ_t using an appropriate turbulent Prandtl number (Pr_t).

Turbulent Kinetic Energy (k):

$$\frac{\partial \rho k}{\partial t} + \nabla \cdot \rho \mathbf{u} k = \nabla \cdot \left[\frac{\mu_{\text{eff}}}{\sigma_k} \nabla k \right] + \rho (P - \varepsilon - D) \quad (6)$$

Dissipation Rate (ε):

$$\frac{\partial \rho \varepsilon}{\partial t} + \nabla \cdot \rho \mathbf{u} \varepsilon = \nabla \cdot \left[\frac{\mu_{\text{eff}}}{\sigma_\varepsilon} \nabla \varepsilon \right] + C_{\varepsilon_1} f_1 \frac{\rho P \varepsilon}{k} - C_{\varepsilon_2} f_2 \frac{\rho \varepsilon^2}{k} + E \quad (7)$$

The standard values for the constants appearing in the turbulence model are:

$$C_\mu = 0.09$$

$$C_{\varepsilon_1} = 1.44$$

$$C_{\varepsilon_2} = 1.92$$

$$\sigma_k = 1.0$$

$$\sigma_\varepsilon = 1.3$$

The production rate of turbulence is given by:

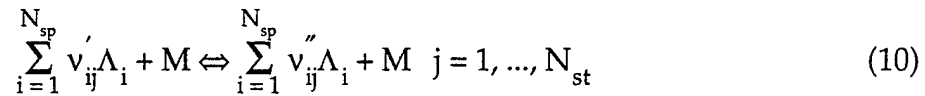
$$P = \frac{\mu_t}{\rho} \nabla \mathbf{u} \cdot (\nabla \mathbf{u} + \nabla \mathbf{u}^T) \quad (8)$$

Species Conservation:

$$\frac{\partial \rho Y_i}{\partial t} + \nabla \cdot \rho \mathbf{u} Y_i = \nabla \cdot D_i \nabla Y_i + \dot{\omega}_i, \quad i = 1, \dots, N_{sp} \quad (9)$$

where Y_i is the species mass fraction, D_i is the mass diffusivity, $\dot{\omega}_i$ are the reaction rate terms (computed as shown below) and N_{sp} is the number of species.

For a general chemical reaction with 3rd body [17]:



the reaction rate can be expressed in the form:

$$\dot{\omega}_j = \left\{ \sum_{i=1}^{N_{sp}} c_{ij} [\Lambda_i]^{b_{ij}} \right\} \left\{ K_{f,j} \prod_{i=1}^{N_{sp}} [\Lambda_i]^{a'_{ij}} - K_{b,j} \prod_{i=1}^{N_{sp}} [\Lambda_i]^{a''_{ij}} \right\} \quad (11)$$

where v'_{ij} , v''_{ij} , Λ_i , $[\Lambda_i]$ are forward and reverse stoichiometric coefficients, molecular symbol and concentration of i th species, respectively and N_{st} is the number of reaction steps. c_{ij} , b_{ij} are coefficients of the 3rd-body efficiency. $K_{f,j}$, $K_{b,j}$, a'_{ij} , a''_{ij} are the rate constants and concentration exponents of reaction rate, and the $K_{f,j}$ (or $K_{b,j}$), can be expressed in Arrhenius form:

$$K_{f,j} = A_j T^{n_j} \exp \left(\frac{E_{a,j}}{R_u T} \right) \quad (12)$$

For reactions obeying mass action law:

$$\begin{aligned} b_{ij} &= 1 \\ a'_{ij} &= v'_{ij} \\ a''_{ij} &= v''_{ij} \end{aligned} \quad (13)$$

The reverse rate constant is derived from:

$$K_{b,j} = \frac{K_{f,j}}{K_{eq,j}} \quad (14)$$

with equilibrium constant:

$$K_{eq,j} = \left(\frac{p_o}{R_u T} \right)^{\sum_{i=1}^{N_{sp}} (v_{ij}'' - v_{ij}')} \exp \left\{ - \frac{\sum_{i=1}^{N_{sp}} (v_{ij}'' - v_{ij}') g_i}{R_u T} \right\} \quad (15)$$

where p_o is 1 atm and Gibbs free energy, $g_i = h_i - Ts_i$.

The final form of production rate for i th species is obtained as:

$$\dot{\omega}_i = M_i \sum_{j=1}^{N_{st}} (v_{ij}'' - v_{ij}') \dot{\omega}_j \quad (16)$$

This value is substituted into the transport equation for species i .

2.2 Models for Thermophysical Properties

The properties such as ρ , μ , λ , and η in the above equations have to be calculated for the supercritical regime. Ideal gas approximations are not valid due to steep variations (in these properties) across the critical point. The following sections present a detailed formulation for the estimation of these properties.

Calculation of Viscosity: The low pressure viscosity is calculated from the expression by Chung, et al. [18]

$$\eta^\circ = 40.785 \frac{F_c (MT)^{1/2}}{V_c^{2/3} \Omega_v} \quad (17)$$

η° = low pressure viscosity, μP

M = Molecular Weight, g/mol

T = Temperature, $^\circ\text{K}$

V_c = critical volume, cm^3/mol

Ω_v is a collision integral of the form:

$$\Omega_v = [A (T^*)^{-B}] + C [\exp (-DT^*)] + E [\exp (-FT^*)] \quad (18)$$

where

$T^* = kT/\epsilon$, $A = 1.16145$, $B = 0.14874$

$C = 0.52487$, $D = 0.77320$, $E = 2.16178$, $F = 2.43787$

k = Boltzmann Constant

ϵ = characteristic energy of interaction between molecules

The collision integral is based on a Lennard-Jones potential function of the form,

$$\psi(r) = 4\epsilon \left[\left(\frac{\sigma}{r} \right)^{12} - \left(\frac{\sigma}{r} \right)^6 \right] \quad (19)$$

where σ is the collision diameter of the molecule.

The factor ϵ/k can be expressed as:

$$\frac{\epsilon}{k} = \frac{T_c}{1.2593} \quad (20)$$

where T_c is the critical temperature. Therefore,

$$T^* = 1.2593 T_r \quad (21)$$

where $T_r = T/T_c$ is the reduced temperature.

The factor F_c is calculated as:

$$F_c = 1 - 0.2576 \omega + 0.059035 \mu_r^4 + k \quad (22)$$

where ω is an acentric factor dependent on the polarity of the molecule, μ_r is a dimensionless dipole moment and k is a correction for highly polar molecules.

The high pressure viscosity using the Chung formulation is given by:

$$\eta = \eta^* \frac{36.344 (MT_c)^{1/2}}{V_c^{2/3}} \quad (23)$$

where

$$\eta^* = \frac{(T^*)^{1/2}}{\Omega_V} \{F_c [(G_2)^{-1} + E_6 y]\} + \eta^{**}$$

$$y = \frac{V_c}{6V}; \quad V = \text{molecular (cm}^3/\text{mol)}$$

$$G_1 = \frac{1 - 0.5y}{(1-y)^3}$$

$$G_2 = \frac{E_1 \{ [1 - \exp(-E_4 y)]/y \} + E_2 G_1 \exp(E_5 y) + E_3 G_1}{E_1 E_4 + E_2 + E_3}$$

$$\eta^{**} = E_7 y^2 G_2 \exp [E_8 + E_9 (T^*)^{-1} + E_{10} (T^*)^{-2}]$$

The constants E_1 through E_{10} are tabulated in the following table.

Table 2-1. Constants for Viscosity Model

$$E_i = a_i + b_i w + c_i \mu_r^4 + d_i k$$

i	a_i	b_i	c_i	d_i
1	6.234	50.412	-51.680	1189.0
2	1.210×10^{-3}	-1.154×10^{-3}	-6.257×10^{-3}	0.03728
3	5.283	254.209	-168.48	3898.0
4	6.623	38.096	-8.464	31.42
5	19.745	7.630	-14.354	31.53
6	-1.900	-12.537	4.985	-18.15
7	24.275	3.450	-11.291	69.35
8	0.7972	1.117	0.01235	-4.117
9	-0.2382	0.06770	-0.8163	4.025
10	0.06863	0.3479	0.5926	-0.727

4240/1 11

The above formulation for calculating dense fluid viscosities shows good agreement with experimental data and the errors are usually less than 5%.

Calculation of Thermal Conductivity: The high pressure thermal conductivity of a substance is given by the expression of Chung et al. [18].

$$\lambda = \frac{31.2\eta^0\Psi}{M'} (G_2^{-1} + B_6 y) + q B_7 y^2 T_r^{1/2} G_2 \quad (24)$$

λ = thermal conductivity, W/(m - °K)

η^0 = Low pressure gas viscosity, N · S/m²

M' = Molecular weight, Kg/mol

$q = 3.586 \times 10^{-3} (T_{c/M})^{1/2} / V_c^{2/3}$

The factor Ψ is given as:

$$\Psi = 1 + \alpha \{ [0.215 + 0.28288\alpha - 1.061\beta + 0.26665Z] / [0.6366 + \beta Z + 1.061\alpha\beta] \} \quad (25)$$

where

$$\alpha = \frac{C_v}{R} - \frac{3}{2}; (C_v = C_p - R)$$

$$\beta = 0.7862 - 0.7109\omega + 1.3168 \omega^2$$

$$z = 2.0 + 10.5 T_r^2$$

C_v = Specific heat at constant volume

C_p = Specific heat at constant pressure

R = Universal gas constant

$$G_1 = \frac{1 - 0.5y}{(1 - y)^3}$$

$$G_2 = \frac{\frac{B_1}{y} [1 - \exp(-B_4 y)] + B_2 G_1 \exp(B_5 y) + B_3 G_1}{B_1 B_4 + B_2 + B_3}$$

the coefficients B_1 to B_7 are tabulated below:

Table 2-2. Constants for the Thermal Conductivity Model

$B_i = a_i + b_i \omega + c_i \mu_r^4 + d_i k$				
i	a_i	b_i	c_i	d_i
1	2.4166 E+0	7.4824 E-1	-9.1858 E-1	1.2172 E+2
2	-5.0924 E-1	-1.5094 E+0	-4.9991 E+1	6.9983 E+1
3	6.6107 E+0	5.6207 E+0	6.4760 E+1	2.7039 E+1
4	1.4543 E+1	-8.9139 E+0	-5.6379 E+1	7.4344 E+1
5	7.9274 E-1	8.2019 E-1	-6.9369 E-1	6.3173 E+1
6	-5.8634 E+0	1.2801 E+1	9.5893 E+0	6.5529 E+1
7	9.1089 E+1	1.2811 E+2	-5.4217 E+1	5.2381 E+2

The ideal gas specific heat, C_p , is calculated from the JANNAF data for each species as a function of temperature.

Calculation of Density: The Corresponding States principle is used to calculate the density of the fluid,

$$Z = \frac{PV}{RT} \quad (26)$$

where Z is the compressibility factor. Z is obtained as:

$$Z = Z^{(0)}(T_r, P_r) + \omega Z^{(1)}(T_r, P_r) \quad (27)$$

The function $Z^{(0)}$ would apply to spherical molecules and $Z^{(1)}$ is a deviation function. $Z^{(0)}$ and $Z^{(1)}$ are tabulated as a function of T_r and P_r in Tables 3-2 and 3-3 of Reference 18, respectively.

Calculation of Enthalpy: For a pure substance, the zero limit of pressure signifies the enthalpy of an ideal gas, h^* . The real gas enthalpy ' h ' at any temperature can be obtained from the following relationship as a function of T_r and P_r :

$$\frac{h^* - h}{RT_c} = F^{(0)} + \omega F^{(1)} \quad (28)$$

where $F^{(0)}$ and $F^{(1)}$ are tabulated as functions of T_r and P_r in Tables 5-2 and 5-3 of Reference 18, respectively. The ideal gas enthalpy h^* is obtained from the JANNAF data. It is observed the dependence of ' h ' on the temperature is highly non-linear. An iterative process is adopted to obtain the temperature from the enthalpy at any given point in the computational domain.

2.3 Models for Turbulence

Most of the turbulence models either explicitly or implicitly assume the presence of a logarithmic layer near the wall. Fortunately, the logarithmic layer is shown to persist in various wall-attached flows such as flow in adverse pressure gradient, compressible flows etc. This is to be expected because, far away from the wall, turbulence production dominates over dissipation and very close to the wall (in the laminar sublayer), dissipation is dominant. However, in some region close to the wall, the turbulence production will be of the same order as dissipation. This region is called the logarithmic layer. From the law of the wall, the turbulent velocity and temperature profiles may be expressed as:

$$\begin{aligned}
u_+ &= \frac{1}{k} \ln(Ey_+) \\
T_+ &= \frac{(T_w - T) \sqrt{\frac{\tau_w}{\rho}}}{\dot{q}_w / \rho C_p}
\end{aligned} \tag{29}$$

where

$$\begin{aligned}
y_+ &= \frac{\sqrt{\rho \tau_w} y}{\mu} \\
u_+ &= \frac{u}{\sqrt{\tau_w / \rho}} \\
k &= 0.4034 \\
E &= 9.7
\end{aligned} \tag{30}$$

ρ is the fluid density, C_p is the specific heat, T_w is the wall temperature, T is the fluid temperature, \dot{q}_w is the wall heat flux, τ_w is the wall shear stress, y is the normal distance from the wall, and u is the fluid velocity.

Standard k- ϵ Model: In the standard k- ϵ turbulence models, the k and ϵ equations are not integrated up to the wall. Instead, the shear stress and the heat transfer are calculated using wall functions. Hence the center of the first grid cell near the wall is required to be approximately located in the logarithmic layer ($y_+ > 30$) and the computational grid will be relatively coarse near the wall. The wall functions used in the CFD-ACE code are given below:

$$\rho \frac{U_{rel}}{\tau_w} C_\mu^{1/4} k^{1/2} = \frac{1}{k} \ln \left[\rho E y \frac{(C_\mu^{1/2} k)^{1/2}}{\mu} \right] \tag{31}$$

$$\frac{(T - T_w) C_p \rho C_\mu^{1/4} k^{1/2}}{\dot{q}_w} = \frac{P_{r_t}}{k} \ln \left[\frac{\rho E y (C_\mu^{1/2} k)^{1/2}}{\mu} \right] + P_{r_t} \frac{\pi/4}{\sin \pi/4} \left(\frac{A}{K} \right)^{1/2} \left(\frac{P_{r_t}}{P_{r_i}} - 1 \right) \left(\frac{P_{r_t}}{P_{r_i}} \right)^{1/4} \tag{32}$$

where A is the van Driest's constant take to be 26.0. Pr_1 and Pr_t are the laminar and turbulent Prandtl numbers, respectively.

Two-Layer Turbulence Model: As mentioned above, in the standard k - ϵ model the shear stress and heat transfer are calculated from k and ϵ values at the first grid point near the wall using wall functions. It has been shown that these predictions are sensitive to the location of the near-wall grid point especially for supercritical fluid flows. To circumvent these difficulties, a two-layer model was proposed. In this approach, the near-wall region is divided into two layers: (1) an inner layer in which the viscosity length scale is obtained from a Van Driest type correlation; and (2) an outer layer in which the standard k - ϵ model is used. The interface between these two layers is identified by a matching criteria. The major advantage of this approach is that substantially fewer grid cells are required in the inner layer than those required for a low Reynolds number model. The mathematical details of the two-layer model are described below and the results obtained using this model are presented in Section 6.

In the outer layer, the standard k - ϵ equations govern the transport of turbulence and the eddy viscosity is computed as:

$$\mu_t = \rho C_\mu \frac{k^2}{\epsilon} \quad (33)$$

where C_μ is taken to be 0.09. In the inner layer, the molecular viscosity is either dominant or comparable to the eddy viscosity. Hence the above equation is replaced by:

$$\mu_t = \rho C_\mu \sqrt{k} \ell_\mu \quad (34)$$

where ℓ_μ is a viscosity length scale. It is determined using the following Van Driest type correlation:

$$\ell_\mu = C_\ell y \left[1 - \exp \left(-\frac{Re}{a} \right) \right] \quad (35)$$

where Re is a local Reynolds number based on the turbulent kinetic energy given by

$$Re = \frac{\rho \sqrt{k} y}{\mu} \quad (36)$$

and the C_μ is constant. To satisfy the log law near the wall, C_μ is taken to be

$$C_\mu = \frac{\kappa}{C_\mu^{3/4}} \quad (37)$$

where κ is the Von Karman constant. In the outer layer, the ϵ equation is replaced by an algebraic length scale equation:

$$\epsilon = \frac{k^{3/2}}{\ell_\epsilon} \quad (38)$$

where the dissipation length scale is modeled as:

$$\ell_\epsilon = \frac{C_\mu y}{\frac{1+b}{Re}} \quad (39)$$

In the CFD-ACE code, the values for constants a and b appearing in the above equations are taken to be [19]:

$$a = 50.5 \text{ and } b = 5.3$$

The ratio between the viscous and dissipation length scales is given by:

$$f_\mu = \frac{\ell_\mu}{\ell_\epsilon} = \frac{1 - \exp(-Re/a)}{1 / (1 + 5.3 / Re)} \quad (40)$$

Note that f_μ is only a function of Reynolds number. The two-layer model is based on the premise that the viscosity length scale is smaller than the dissipation length

scale inside the inner layer and approaches unity towards the outer layer. Though several criteria have been used to identify the interface between the layers, the location where f_μ becomes unity is identified as the interface in the CFD-ACE code.

Low Reynolds Number Model: In the case of near- or super-critical flows, the transport properties such as molecular viscosity and thermal conductivity are strong functions of local conditions. Consequently, the constants used in the law of the wall may not be constants and could vary for different fluids. Hence the standard k - ϵ model may not be appropriate for supercritical fluids. Moreover, since the grid will be relatively coarse near the wall, the local property variation cannot be taken into account. The low Reynolds number model requires the grids to be very fine near the wall ($y^+ < 1$). In the low Reynolds number model, the eddy viscosity is given by [20]:

$$\mu_t = \rho C_\mu f_\mu \frac{k^2}{\epsilon}$$

where f_μ is given by [20]:

$$f_\mu = 1 - \exp(-0.0115 y^+) \quad (41)$$

The function f_1 , f_2 , E used in the ϵ equation are given by:

$$E = -2\rho\mu \left(\frac{\epsilon}{y^2}\right) \exp(-0.5 y^+) \text{ and } f_1 = 1.0 ; f_2 = 1 - 0.22 \exp\left(-\left(\frac{Re}{6}\right)^2\right) \quad (42)$$

In the standard k - ϵ model, the turbulent Prandtl number is taken to be constant (0.7). For supercritical fluids, however, this assumption does not yield accurate results. It has been observed that the turbulent Prandtl number close to the wall increases due to the sublayer "bursting" phenomenon. In order to account for these effects, the following correlation is used in the present calculations [21]:

$$P_{rt} = \left[\frac{1}{2P_{r_{ta}}} + CP_{e_t} \sqrt{\frac{1}{P_{r_{ta}}}} - (CP_{e_t})^2 \left(1 - \exp\left(-\frac{1}{CP_{e_t} \sqrt{P_{r_{ta}}}}\right) \right) \right]^{-1} \quad (43)$$

where P_{e_t} is the turbulent Peclet number given by:

$$P_{e_t} = \left(\frac{\mu_t}{\mu} \right) P_{r_t} \quad (44)$$

and $P_{r_{tr}}$ is the turbulent Prandtl number far away from the wall, an experimentally determined constant and C is an experimental constant. For the results shown in the next section, C is taken to be 0.2 and $P_{r_{tr}}$ is taken to be 0.86.

2.4 Models for Thermal Stability of Fuels

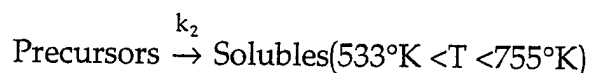
The process of thermal decomposition of fuels that leads to surface deposition consists of a series of complex reaction mechanisms. The reaction initiation depends on the temperature of the fuel. For fuel temperatures less than about 540°K, the primary mechanism for deposition is the oxidation of fuel by the dissolved oxygen, i.e., auto-oxidation. For fuel temperatures greater than 750°K, thermal pyrolysis of hydrogen molecules and the scission of hydrogen atoms from carbon atoms become the dominant processes. In the intermediate temperature range, deposition occurs through the formation of precursors which decompose at the wall to give rise to the deposit.

Thermal stability of jet fuels has received considerable attention over the last decade. Recent studies have focused on the identification and modeling of various reaction mechanisms for thermal decomposition of fuels. Two models, the 4-step model and the 9-step model are described below.

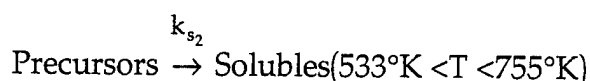
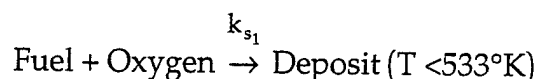
4-Step Model: Krazinski et al. [22] proposed the following global fuel deposition mechanism for bulk fuel and surface reactions at the wall. The auto-oxidation of the fuel with the dissolved oxygen can be expressed as:



The precursor may either lead to direct deposition at the wall or to the formation of solubles at higher temperatures:



The reactions at the wall may be expressed as:



For fuel temperatures less than 533°K , the first surface reaction controls the deposition process without the formation of precursors. For temperatures between 533°K and 755°K , precursor formation (and transformation to solubles) according to gas phase reaction 1 and 2 is the controlling mechanism. The deposit formation at the wall occurs due to the decomposition of the precursor at the wall according to the second surface reaction. For temperatures greater than 755°K , fuel pyrolysis becomes the dominant process.

The rates for the above reactions are written as:

$$k_1 = 10^{11} \exp\left(-\frac{15.1 \times 10^3}{T}\right) \frac{\text{m}^3}{\text{kg} \cdot \text{mol}}$$

$$k_2 = 3 \times 10^{15} \exp\left(-\frac{17.6 \times 10^3}{T}\right) \text{sec}^{-1}$$

for surface reactions at the wall,

$$D_{\text{O}_2} \left. \frac{\partial [\text{O}_2]}{\partial n} \right|_w = k_{s_1} [\text{Fuel}]_w [\text{O}_2]_w$$

$$k_{s_1} = 6.34 \times 10^{-5} \exp\left(-\frac{4.022 \times 10^3}{T}\right) \frac{\text{m}^4}{\text{kg} \cdot \text{mol}} \quad (45)$$

The precursor is assumed to decompose at the wall with a reaction probability of one, i.e., the precursor concentration on the wall can be set to zero and the precursor flux can be directly translated into an equivalent deposition rate, i.e.,

$$[P_r]_w = 0 \quad (46)$$

In the present study, transport equations were solved for oxygen and precursor concentration in the field using the rate expressions given above. Since oxygen and the precursors exist as trace species in the fuel, their impact on bulk flow and heat transfer characteristics are ignored. Therefore, the flow field and the heat transfer are calculated using the single component (i.e., the fuel) approximation and the oxygen and precursor concentrations are treated as passive scalars.

The total deposition rate is calculated as:

$$\dot{m} = (M_{\text{fuel}} + M_{\text{O}_2}) \left[D_{\text{O}_2} \frac{\partial [\text{O}_2]}{\partial y} \Big|_w + D_{\text{Pr}} \frac{\partial [\text{Pr}]}{\partial y} \Big|_w \right] \quad (47)$$

where M is the molecular weight and \dot{m} is the mass flux to the surface.

9-Step Model: A more advanced model, developed at Wright Laboratory by Katta et. al. [23] was also incorporated into CFD-ACE. This chemistry mechanism is illustrated below:

<u>Reaction</u>	<u>Activation Temperature (°K)</u>	<u>Pre-Exponential</u>
<u>Gas Phase:</u>		
$F + O_2 \xrightarrow{k_1} R00^\circ$	16.1×10^3	$2.5 \times 10^{10} (\text{kmol}/\text{m}^3 \text{sec})$
$R00^\circ + F \xrightarrow{k_2} \text{Solubles}$	5.04×10^3	$1 \times 10^4 (\text{sec}^{-1})$
$R00^\circ + F_s \xrightarrow{k_3} P$	7.55×10^3	$8.0 \times 10^9 (\text{sec}^{-1})$

$R00^\circ + F \xrightarrow{k_4} D_{\text{bulk}}$	5.04×10^3	$2.0 \times 10^2 (\text{sec}^{-1})$
$P + F \xrightarrow{k_5} \text{Solubles}$	15.1×10^3	$3.2 \times 10^{12} (\text{sec}^{-1})$
$D_{\text{bulk}} + F \xrightarrow{k_6} 2D_{\text{bulk}}$	0.0	$1.0 \times 10^{-3} (\text{sec}^{-1})$

Surface:

$O_2 + F \xrightarrow{k_7} P$	6.04×10^3	5.2×10^{-3}
$P \xrightarrow{k_8} D_{\text{wall}}$	8.56×10^3	260.0 (m/sec)
$D_{\text{bulk}} \xrightarrow{k_9} D_{\text{wall}}$	5.04×10^3	0.80 (m/sec)

The deposition rate is calculated as:

$$D \frac{\partial D_{\text{wall}}}{\partial n} = \frac{c}{\tau_w^{0.7}} \{ [P]_{\text{wall}} A_8 \exp(-T_{a8}/T) + [D_{\text{bulk}}]_{\text{wall}} A_9 \exp(-T_{a9}/T) \} \quad (48)$$

During the computations, it was found that the above model agreed with data only under certain restrictive conditions (See explanation in Section 8). In order to improve the generality of the model, the surface reactions were recalibrated. The recalibrated model is described below.

Recalibrated 9-Step Model: The gas phase reactions are the same as the original 9-step model. The surface reactions are recalibrated as follows:

<u>Reaction</u>	<u>Activation Temperature (°K)</u>	<u>Pre-Exponential</u>
-----------------	------------------------------------	------------------------

Surface:

$O_2 + F \xrightarrow{k_7} D_{wall}$	4.03×10^3	$2.0 \times 10^{-5} \text{ (m}^4/\text{kmol-sec)}$
--------------------------------------	--------------------	--

$P \xrightarrow{k_8} D_{wall}$	8.56×10^3	40 (m/sec)
--------------------------------	--------------------	----------------------

$D_{bulk} \xrightarrow{k_9} D_{wall}$	5.04×10^3	0.8 (m/sec)
---------------------------------------	--------------------	-----------------------

and the deposition rate is given by:

$$D \frac{\partial [D_{wall}]}{\partial n} = \left\{ A_7^n \exp \frac{(-T_{a7})}{T} [F]_{wall} [O_2]_{wall} + A_8 \exp \frac{(-T_{a8})}{T} [P]_{wall} + A_9 \exp \frac{(-T_{a9})}{T} [D_{bulk}]_{wall} \right\} \quad (49)$$

For JP-5 , the constants are recalibrated as:

$$A_7 = 6.3 \times 10^{-5} \left(\frac{\text{m}^4}{\text{kmol} - \text{sec}} \right) \text{ and } A_8 = 400 \text{ m/s}$$

These constants are closer to the values used by the original Krazinski model.

3. EXPERIMENTAL DEPOSITION STUDIES WITH JET FUELS

This section describes the experiments (conducted at Wright Laboratory) with jet fuels over a range of operating conditions. The objective of the experiments is to establish a data base of temperature and deposition during the heating of jet fuel to a near thermodynamic critical state.

To study deposition by jet fuel at high temperatures, fuel was pumped through a long heated test section at various flow rates, pressures, and heat fluxes, and for various lengths of time, and the amount of deposition measured as a function of location along the tube. Flow rates of 100, 200, and 300 ml/min were used, at pressures of 650 and 400 psig. (The ambient pressure was assumed to be standard condition and the reduced pressure as typically higher than 1.3.) Heat flux was controlled through the wall temperature of the radiant furnace, which was set at either 2192 or 1832°F (1200 or 1000°C). Test duration was typically 5 or 10 hours.

3.1 Apparatus

The experimental setup is shown in Figure 3-1. Air-saturated Jet A 2926 was used as the fuel in most cases. The fuel was pumped from a supply tank through a pulsation damper and a 0.5 μm filter into the heated test section of stainless steel tubing. The tube was heated by a radiant heater having a maximum wall temperature of 2192°F (1200°C). After emerging from the test section, the fuel passed through a cooling heat exchanger, a 2 μm filter to collect particulate debris resulting from the heat stress, a needle valve to control the pressure, and finally into a collection tank. Pressure was measured at the furnace inlet and at the back pressure valve in psig. A three-way valve located at the collection tank allowed the flow to be diverted for flow rate measurements.

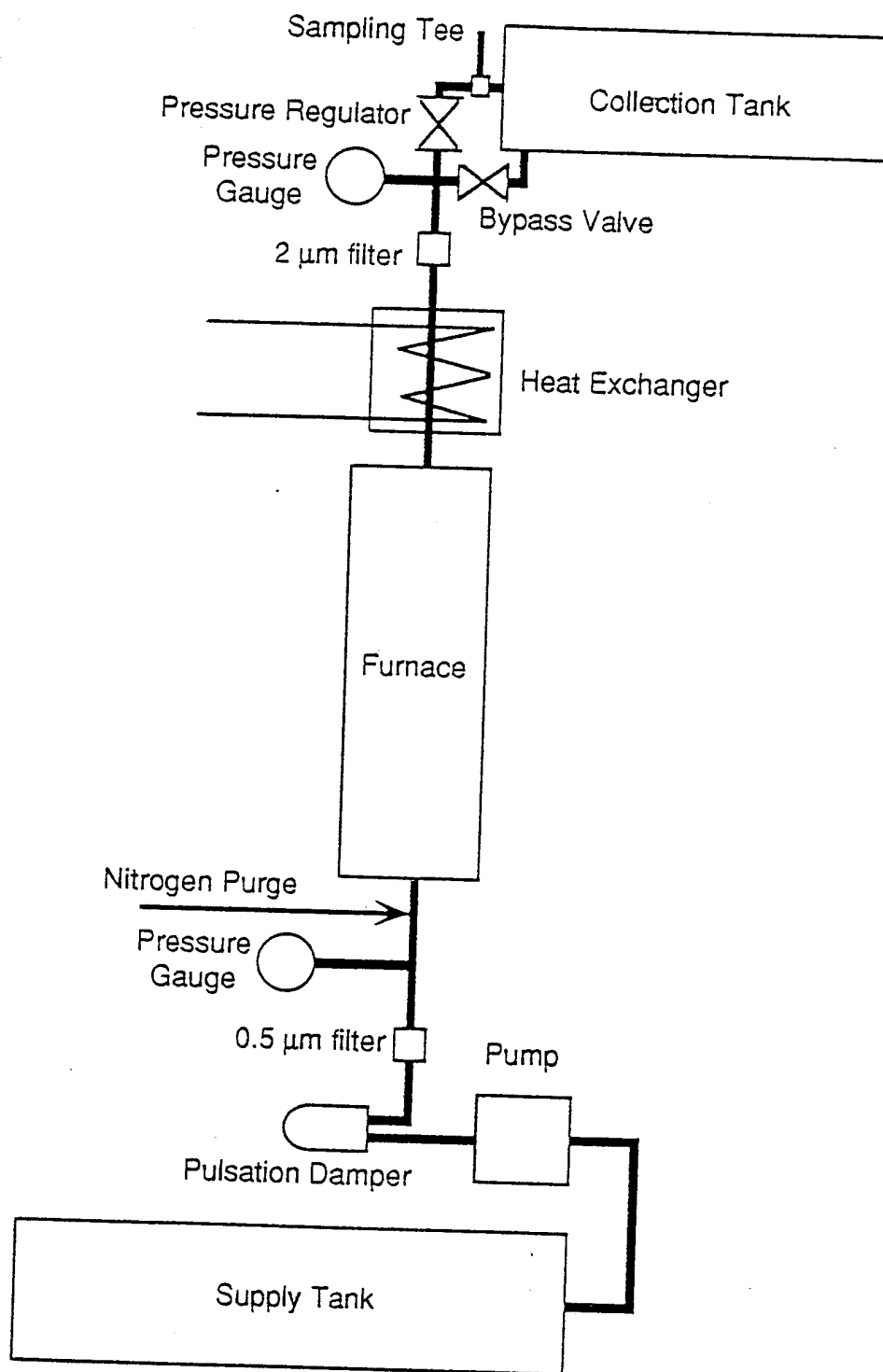


Figure 3-1. Schematic of the Experimental Setup

Saturation of the fuel with either air or nitrogen was achieved by using the appropriate gas from the building supply and bubbling it through the fuel in the supply tank. In the case of nitrogen, the tank was also sealed except for a small vent, and left overnight prior to the test, to ensure the removal of all oxygen from the fuel.

The pump (American Lewa Model EK-01) used was a reciprocating pump with a variable stroke length. The stroke length was set to 8-mm in all cases, and the speed of the motor varied with the electronic controller. The electronic package controlled the motor (rotational) speed, not the flow rate. As a result, flow rates needed to be measured manually. This was done by diverting the exit flow from the collection tank into a graduated cylinder. A manually pre-determined calibration curve was used to approximate the motor speed necessary to achieve a desired flow rate.

The chamber of the pulsation damper (Liquid Dynamics Model Pulsetwin) was filled with nitrogen to 560 psig for the 650 psig tests, and 320 psig for the 400 psig tests. The damper usually worked well, resulting in no noticeable pressure variations on the analog gauges. If the system pressure dropped below the nitrogen chamber pressure, the system pressure began to pulsate severely. This only occurred during start-up and shut-down, however.

The tubing used in all cases was thick-walled AISI 316 stainless steel tubing having 1/8" O.D., and 0.055" I.D., although the second heat exchanger used thin walled tubing, having an I.D. of 0.085". An important note is that the 200 and 300 ml/min tests were not evenly heated, due to multiple passes through the furnace. Continuous tubing was used in all cases, but the U-shaped bends in the tube rested just inside the collars at the ends of the furnace, where the heating was not as intense.

Test section wall temperature measurements were made with K-type thermocouples spot-welded onto the outer surface of the tube at known distances from the beginning of the tube. The exit fuel temperature was measured with a thermocouple probe housed in a T-connector at the end of the test section. The final wall temperature thermocouple was spot-welded onto the outer surface of this T-connector. The beginning of the tube was located about two inches outside one end

of the furnace, and in all but the first couple of tests, the exit T-connector was located completely within the collar at the other end of the furnace. The furnace was a radiant heater (Lindberg Model #55662) with a maximum wall temperature of 2192°F (1200°C). To check the symmetry of heating, the wall temperature profile of a tube carrying only a slow flow of nitrogen was measured. The results are shown in Figure 3-2, along with the dimensions of the furnace. The results demonstrate that the heating is significantly lessened within about five inches of the furnace collars, but it is otherwise quite even. It should be mentioned that there existed errors in furnace temperature readouts as indicated by Figure 3-2 that the measured tube wall temperature was higher than the furnace (wall) temperature.

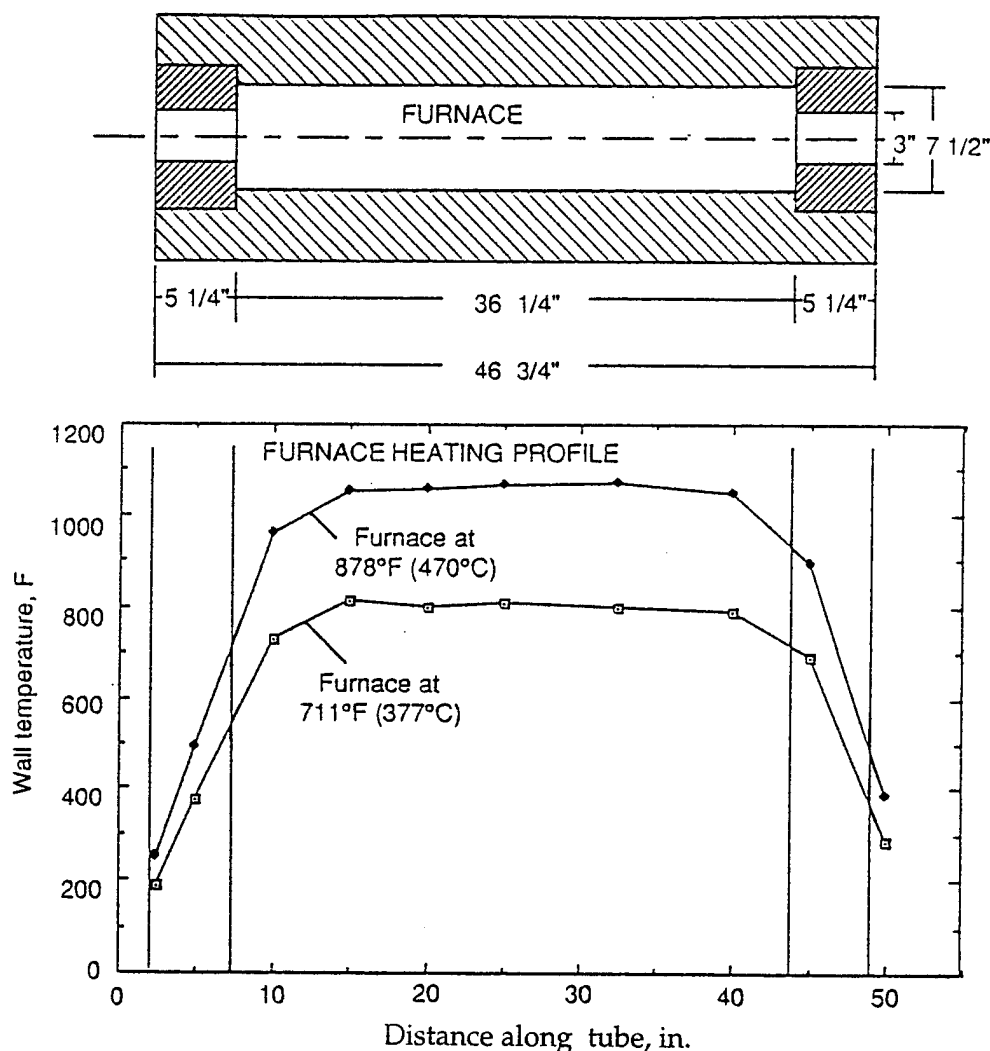


Figure 3-2. Furnace Temperature Profile

The heat exchanger used in the first two tests consisted of several feet of large coaxial tubing, fitted around the primary tubing, and through which water was pumped. This arrangement was not efficient, and was replaced. The second heat exchanger consisted of roughly 15 feet of tubing which was coiled to fit inside a reservoir of water.

Carbon deposition was measured by carbon burn-off (Leco Model RC-412 Multiphase Carbon Determinator). A 0.001g sample weight and an oven temperature of 650°C were used. The accuracy of the determinator is specified by the vendor as $\pm 3\%$ of the answer, or $\pm 0.02\%$ of the sample weight, whichever is greater. Calibration samples were occasionally run, and yielded agreement within a few percent.

3.2 Procedure

After installing the test section and fresh filters, and attaching the thermocouples, fuel was pumped through the system at the operating pressure to check for leaks. Once the system was determined to be leak-free, the furnace was closed and layers of insulation were placed over the openings at the ends of the furnace.

When the test was ready to begin, the pump was turned on and set to the pre-determined speed, and the needle valve was adjusted until the desired pressure was reached. The furnace was then turned on and allowed to warm up for 10 minutes. From this point, the equipment was left to operate for the desired test time. During this time, the temperatures and flow rate were monitored; the pressure system was adjusted or the fuel supply tank replenished, if it became necessary.

Roughly 20 minutes were needed for the temperatures to stabilize after the furnace was turned on. In an attempt to account for this initial warm-up time, 10 minutes were added to the duration of each run, so that a 5 hour run would last 5 hours and 10 minutes from the time the furnace was turned on, to the time it was turned off. Also of note is that tests longer than 5 hours were usually divided into several runs on successive days, with no changes made to the system except for the replacement of the exit filter.

After the furnace was turned off, the insulation covering the openings was removed, and the furnace was allowed to cool to roughly 950°F (which took 5 to 10 minutes), at which time the furnace was opened, and the temperatures began to drop very rapidly. When the furnace walls dropped to roughly 350°F (at which point the tube walls were roughly 100°F, and the fuel temperature was even lower) the fuel flow was stopped, and nitrogen from the building supply was blown through the system to purge it of fuel, and eliminate any further reactions in the tube.

After the test section was sufficiently cool, it was removed, sanded, and cut into 2-inch sections. The sections were then rinsed in hexane to remove any remaining fuel, and dried in a vacuum oven in preparation for being analyzed in the carbon determinator. The filters were similarly rinsed and dried. Occasionally, small flakes of black material would be noticed in the exit filter housing. These were included, to the best effort, in the filter analysis.

3.3 Results and Discussion

Surface deposition data are tabulated in Appendix A. The exit filter deposition rates are presented in Appendix B. Wall temperature data are tabulated in Appendix C. Profiles of deposition and temperature along the tubes are presented in graphic form beginning with the 100 ml/min tests in Figures 3-3 and 3-4. The 100 ml/min tests all show a similar profile. There is an early region of relatively light deposition, followed by a large peak, and a decline to very light deposition again. These two regions apparently represent two different modes of deposition, and the end of the deposition presumably occurs where the oxygen has been completely consumed. The exception to the pattern is the low heat flux run with the furnace set at 1832°F (or 1000°C noted in the figure) instead of 2192°F. In this case, the early region has disappeared, and the deposition peak has moved downstream, reflecting the increased time required to heat the fuel to the temperature at which the heavy deposition begins. Two tests not shown ended with a power failure to the pump. The furnace was quickly opened and the system purged with nitrogen, but the tube became very hot nevertheless. The deposition profiles in these cases were surprisingly similar in general shape to the others, but they are a bit more jagged. It is believed that the pulsation damper provided a limited amount of fuel flow even

after the pump lost power, helping to preserve the deposition until the nitrogen could be started.

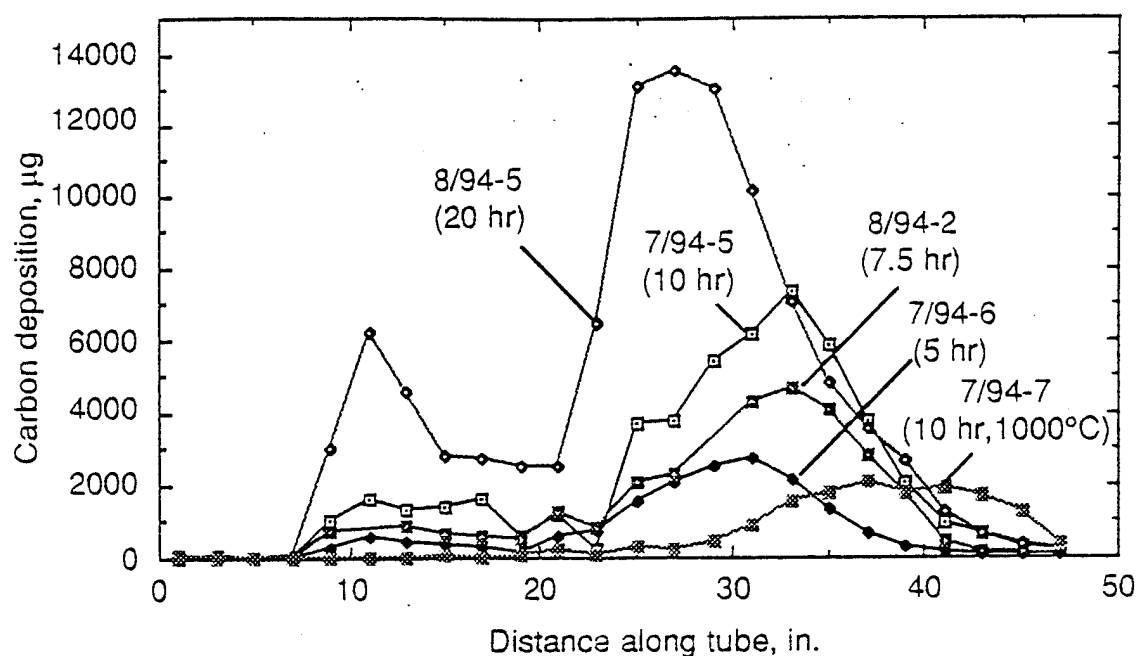


Figure 3-3. Deposition Profile at Flowrate of 100 ml/min

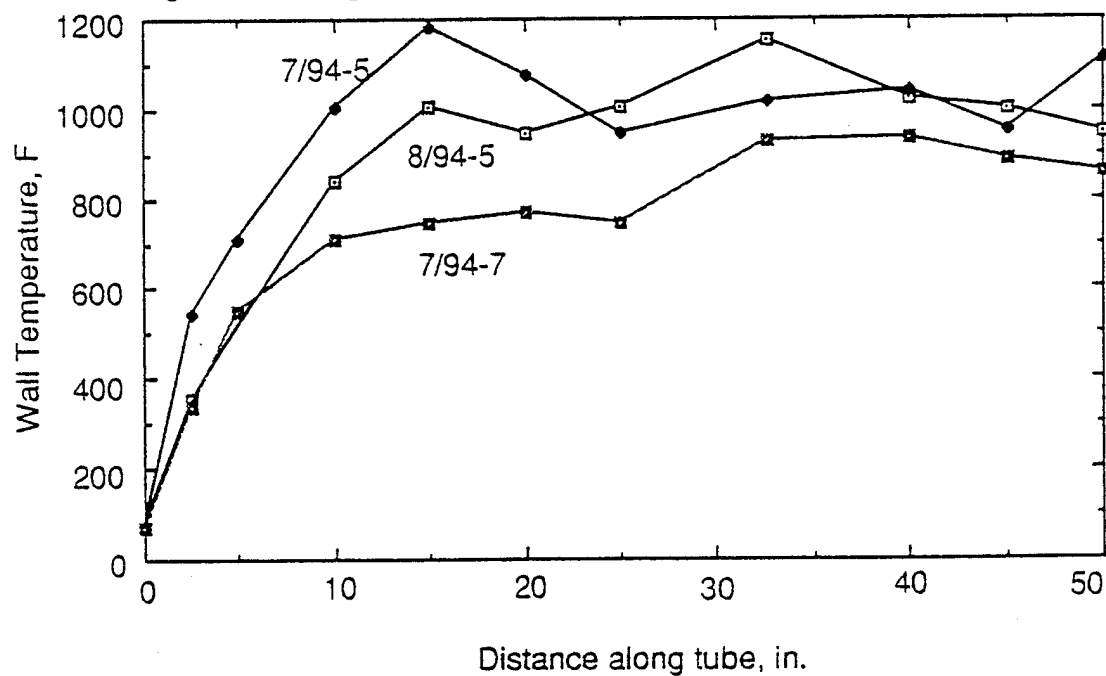


Figure 3-4. Wall Temperature Profile at Flowrate 100 ml/min

The test at 400 psig (#7/94-10), resulted in a deposition profile nearly identical to the corresponding test at 650 psig (#7/94-6), except that the peak was shifted downstream about 8 inches, e.g., see Figure 3-5. The temperature profile (Figure 3-6) shows that the 650 psig test reached higher temperatures than the 400 psig test. The higher temperature may be responsible for the earlier peak observed in the 650 psig test case (#7/94-6). If this is the case, then the results suggest that the pressure (or criticality) effect on deposition profile is not significant. The nitrogen-saturated test (#7/94-11) was conducted under identical conditions to the previous test, except that the fuel was sparged with nitrogen rather than air. Under this condition, the carbon deposition is orders of magnitude below that of the air-saturated test case as shown in Figure 3-5; therefore, it can be deduced that the dissolved oxygen in jet fuel is a major contributor to carbon deposition.

Certain similarities and differences can be seen between the 200 ml/min tests and the 100 ml/min tests, e.g., by comparing Figure 3-7 to 3-3. First, the deposition is separated more clearly into two regions: the early region of light deposition, and the second region composed of a large peak. In this case the second region has begun to split as well, showing two peaks, and suggesting different deposition mechanisms. In the two cases of high heat flux, the second peak occurs shortly after the wall temperature has passed 1000°F, (see Figure 3-8) and lies near a wall temperature peak of about 1100°F. Pyrolytic deposition is one possible explanation for this second peak, but it doesn't explain the second peak in the low flux case. Also, the second region has moved a considerable distance downstream. This is presumably due to the increased distance required for the fuel to heat up to the necessary temperature, although there is no clear, single temperature at which the deposition begins. The reason the five-hour deposition lies farther downstream than the 10-hour deposition can be found in the temperature profiles. The 200 ml/min tests were passed through the furnace twice, and in the case of the five-hour test, the bend in the tube projected significantly into the cooler space of the furnace collar, thus increasing the distance required to heat the fuel. In both cases, the peak begins after the fuel has passed through the bend and where the wall temperature rises through roughly 900°F.

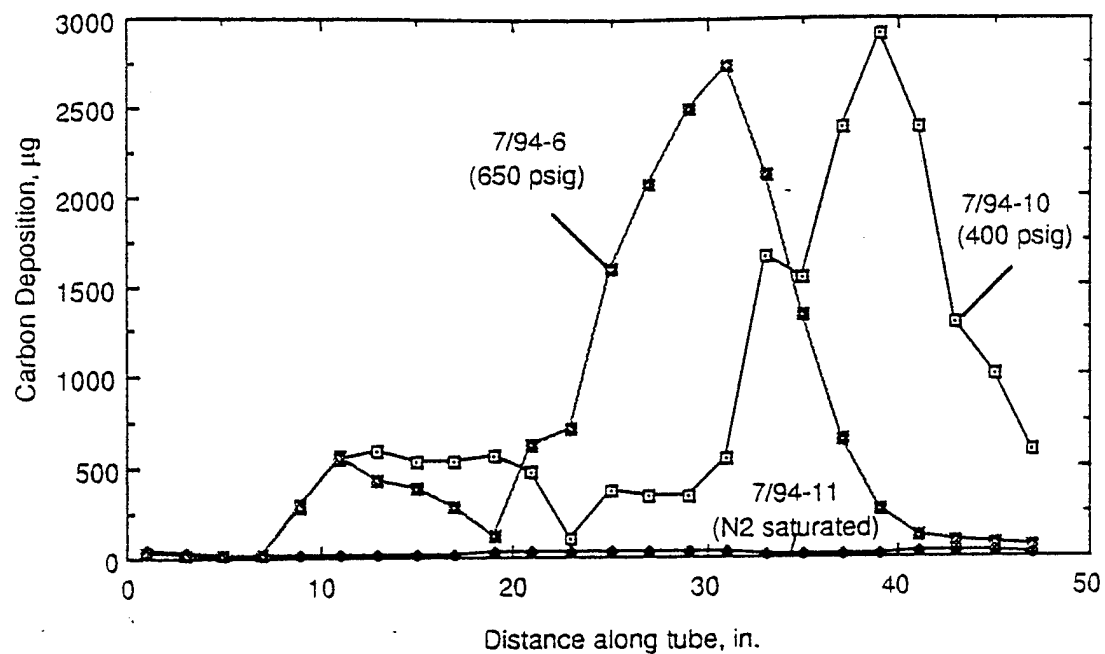


Figure 3-5. Deposition Profiles at System Pressure 400 or 650 psig

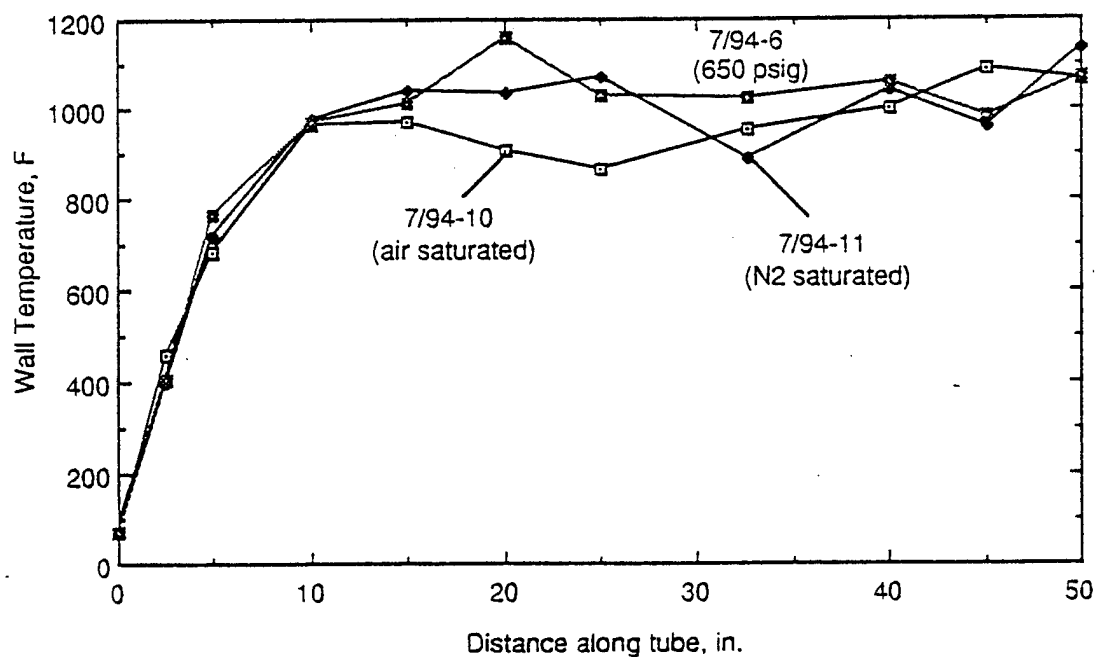


Figure 3-6. Wall Temperature Profiles at System Pressure 400 or 650 psig

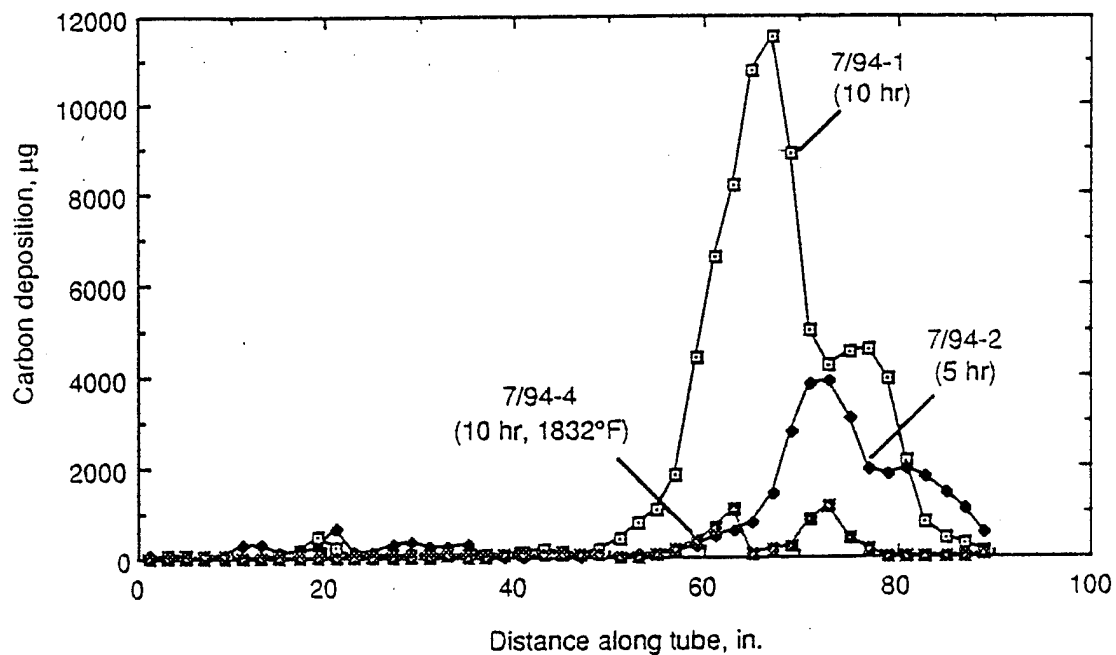


Figure 3-7. Deposition Profile at System Pressure 400 psig

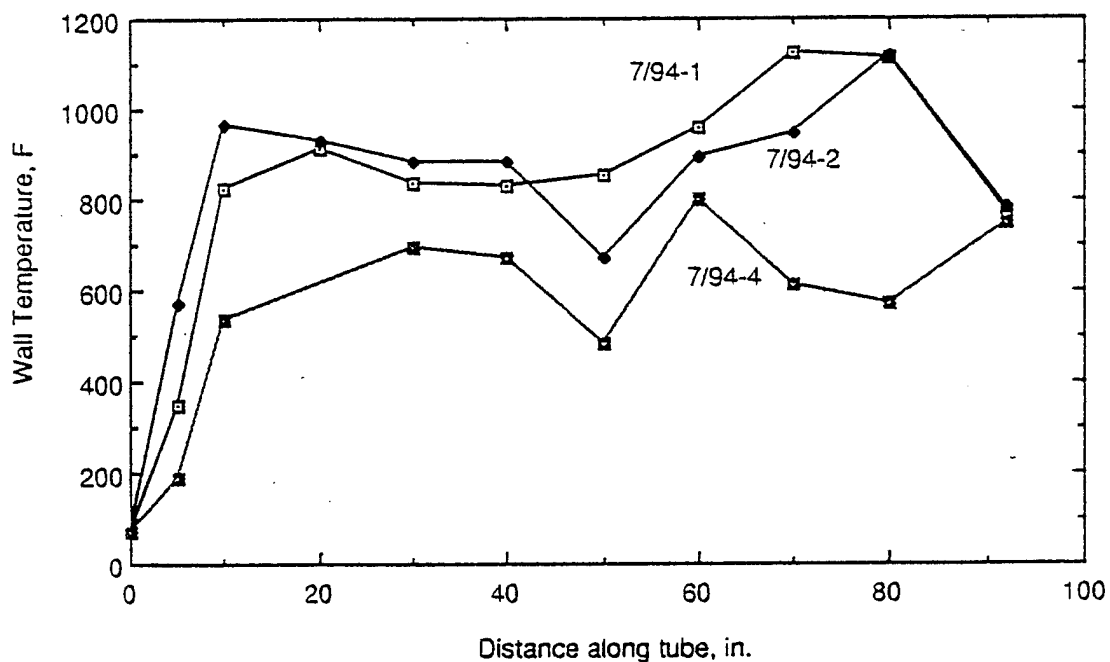


Figure 3-8. Wall Temperature Profile at Flowrate 200 ml/min

In comparison to the slower tests, the first region of deposition in the 300 ml/min test has almost disappeared, cf. Figure 3-9. Unfortunately, even three passes through the furnace was not enough for this flow rate, and the test section was not long enough to collect much of the heavy deposition. However, the deposition began early enough to show that it began at roughly the point where the wall temperature exceeded 900°F.

Summarizing the deposition profiles, it seems that several different mechanisms are at work, accounting for different regions of deposition. A rough estimate for the minimum temperature required for all deposition encountered here is 900°F. In most cases, deposition occurs only where the wall temperature is at or above roughly 900°F. The first region of deposition increases in strength with increasing temperatures (decreasing flow rate), and is spread out along the tube, suggesting that this mechanism may consist of deposits forming at the wall, due to wall temperature alone. The second region, possibly created by more than one mechanism, begins after the fuel has passed through a certain thermal history. Perhaps in this case a minimum bulk fluid temperature is required, which would suggest that the deposits form in the fluid and are transferred to the walls by convection (e.g., by turbulence). All deposition vanishes with the removal of dissolved oxygen, as demonstrated by the de-oxygenated run.

Following the profile graphs are graphs showing the total surface deposition and filter deposition as a function of test duration. If the two tests which ended in a power failure are neglected, as well as the low heat flux test, the 100 ml/min tests show a linear surface deposition rate (Figure 3-10), beginning after a two hour lag time which is probably the time required to coat the metal completely with deposits. This indicates that deposits form on metal much less readily than on other deposits, and that the nature of the deposits doesn't change in time. Since two data points can always be used to form a straight line, the 200 ml/min data is inconclusive. If such a line is drawn, however, it agrees nicely with the 100 ml/min data. The deposition in this case begins after about 2 1/2 hours, and rises at roughly twice the rate as in the 100 ml/min tests. The 300 ml/min data point is not included, since the deposition profile shows that the fuel at the exit had not yet consumed all of the dissolved oxygen. The two tests indicated with an asterisk include estimated data

points in the deposition profile. These data points are missing because the 2-inch tube sections which would have provided them were saved for surface morphology and composition studies. Three sections were saved in each case, and the deposition on them was estimated by taking the average of the two adjacent sections.

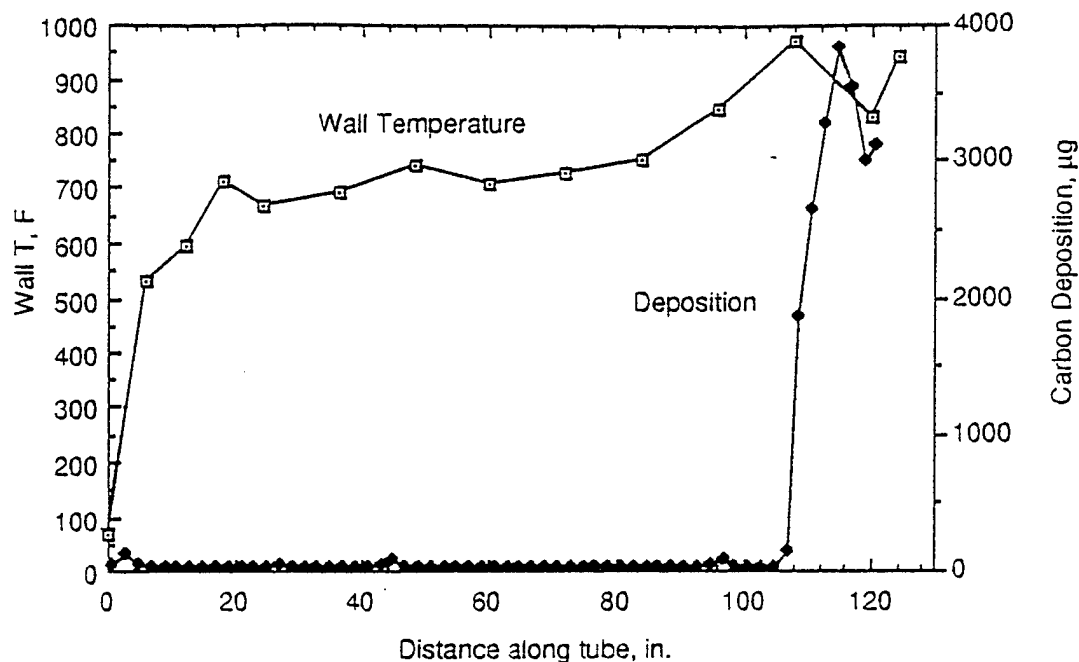


Figure 3-9. Wall Temperature and Deposition Profile at Flowrate 300 ml/min

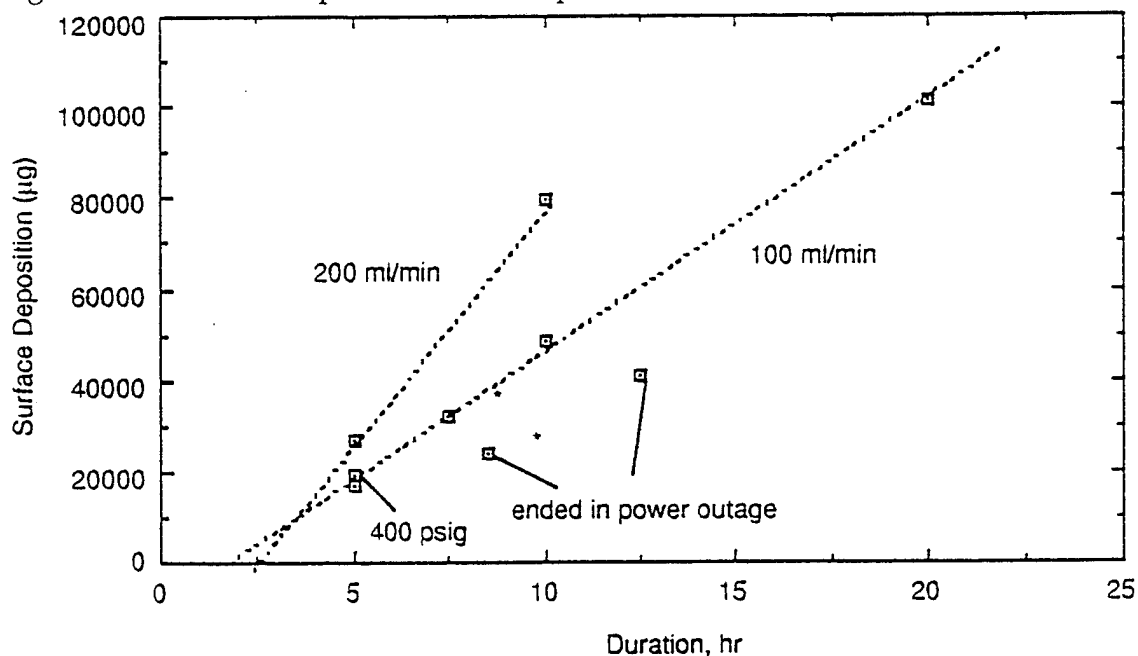


Figure 3-10. Surface Deposition as a Function of Test Duration (Furnace Temperature at 2192°F)

Exit filter deposition as a function of test time is shown in Figure 3-11. A general increase of deposition with time can be seen, but no clear pattern can be discerned. The exit filter deposition occurred after the fuel had passed through the 15-ft length of the heat exchanger, and is probably influenced by factors other than the controlled test conditions. One clear influence, however, is the amount of oxygen consumption in the test section. In the case of the 300 ml/min test, which did not undergo complete oxygen consumption, a 7 μ m filter was used, rather than the usual 2 μ m filter, and large amounts of deposits were collected anyway. In the case of the two lower flux tests, the exit filters collected so much deposition that they began to clog every few hours, after which the pressure drop across the filter, as measured by the difference between the two pressure gauges, would rise steadily, and fairly quickly.

Finally, the behavior of the pressures and temperatures should be noted. After the initial brief temperature rise following the activation of the furnace, all temperatures would generally decline slightly for about 1-1/2 to 2 hours. After this, temperatures in the first half of the tube would stay fairly constant, whereas temperatures farther on, where deposition was usually occurring, rose steadily. A typical example of this is shown in Figure 3-12. The distances given are distances from the beginning of the tube. Temperatures would also vary somewhat from day to day, as well as with varying pressure. The temperatures shown in the profile graphs are the temperatures at the end of test. Temperatures well within the furnace would also frequently exhibit a small oscillation, with a period of 7-8 seconds, and an amplitude of several degrees Fahrenheit. In some of the later tests, thermocouples would sometimes give unreasonably high temperatures, or none at all. In some cases this was due to poor contact or complete loss of contact between the thermocouple wires and the test section. Also, the furnace heating profile graph shows that test section wall temperature measurements were significantly higher than the furnace wall temperature. It is not known how the test section measurements could be in error, and the only explanation available is that the furnace thermocouple may have been pushed a small distance into the insulation of the furnace wall, and gave lower temperature readings as a result. Also, the high temperatures in the furnace caused significant corrosion damage to the thermocouple wires, and this may have contributed to the erroneous measurements. The pressure was generally quite stable. It became somewhat

difficult to control, however, in the case of high flow or low heat flux, which caused very large build-up of deposition in the exit filter.

3.4 Summary

The results of these tests of supercritical fuel deposition show several general features. First, deposition depends on dissolved oxygen and cannot occur without it. Next, pressure has a relatively insignificant effect on deposition over the range of test conditions examined in this study (which have a reduced pressure higher than 1.3). The dominant factor is temperature, both tube wall temperature and bulk fluid temperature. Heat flux and flow rate have an effect, but their effect is not obvious apart from their influence on the temperatures. The effect of test time is straightforward. Deposition continues to build up as time goes on, with a very linear rate in the case of surface deposition. Due to the complexity of deposition, and the large number of factors involved, these results are not easily generalized, and much more work needs to be done before a comprehensive understanding of deposition mechanisms is gained.

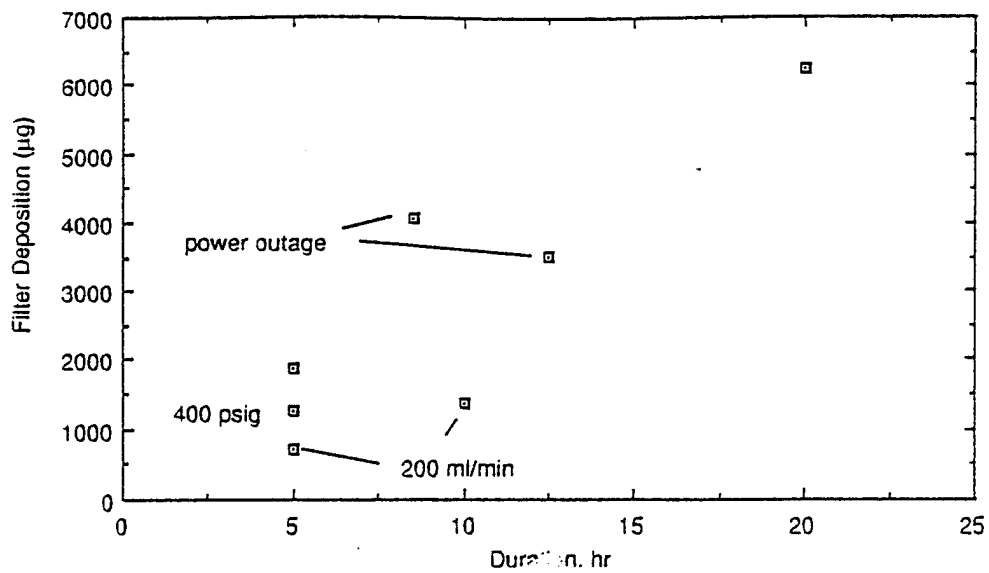


Figure 3-11. Exit Filter Deposition as a Function of Test Duration (Furnace Temperature at 2192°F)

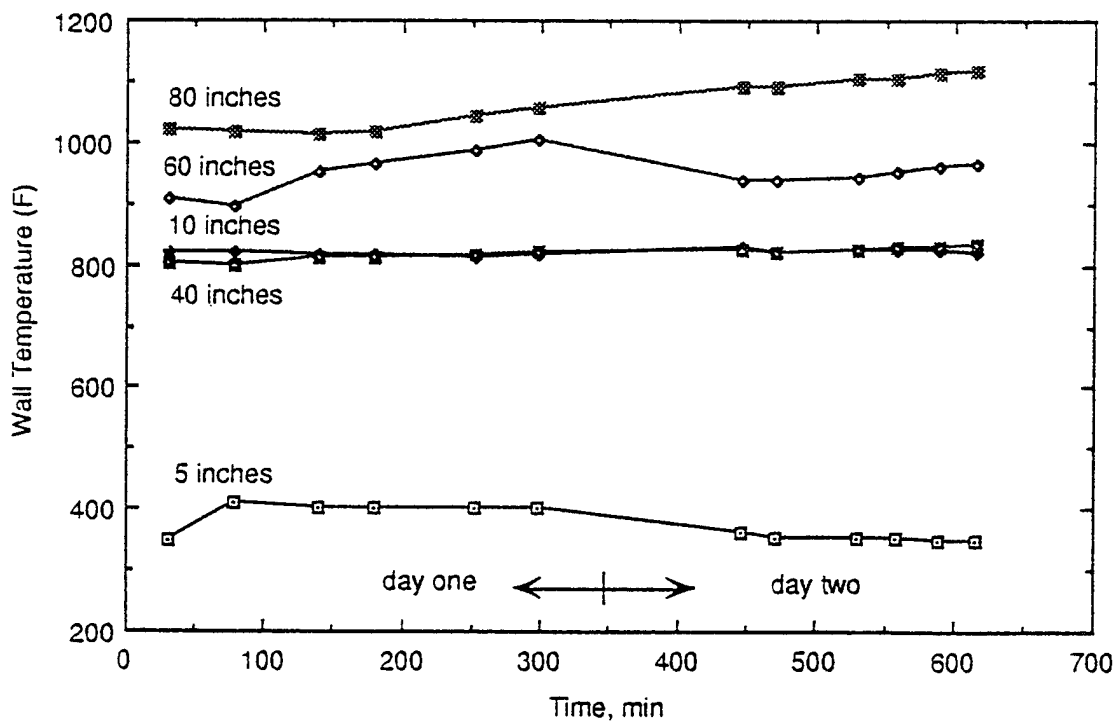


Figure 3-12. Wall Temperatures as a Function of Test Duration, Experiment #7/94-1

4. EXPERIMENTAL HEAT TRANSFER STUDIES WITH A SIMULANT FLUID

This section describes the experiments performed at the University of Iowa with a simulant fluid (SF_6).

4.1 Use of a Simulant

This study was aimed at exploring the heat transfer characteristics of a supercritical fluid, and evaluating whether or not pressure oscillations occur during the heating, without the complication of multiple components, chemical reactions, and deposition. As a simulant for other more complex and more hazardous fluids, such as jet fuel, the working fluid chosen was sulfur hexafluoride (SF_6). This was chosen for its relatively low critical properties (45.54°C and 37.6 bar), and its lack of safety hazards.

4.2 Experimental Setup

A diagram of the experimental setup is shown in Figure 4-1. SF_6 is pumped from a small storage tank at 20.9 bar (the vapor pressure of SF_6 at room temperature) by a reciprocating pump. There is no direct measurement of the flow rate, but a theoretical value can be calculated from the speed of the pump motor, which is given by the electronic controller, and this value can then be modified by an efficiency factor supplied by the vendor. In the earlier experiments using jet fuel, the measured flow rates matched the calculated values to within about 8%. The experimental setup also includes a pulsation damper.

After leaving the pulsation damper, the fluid passes into the test section, which is heated by a radiant furnace. The furnace (Mellen model TC-12) has a heating length of 66 cm (26 "), and a maximum wall temperature of 1200°C . The wall temperature is measured with a thermocouple installed in the interior. A diagram of the furnace is shown in Figure 4-2. The heated test section consists of blackened stainless steel tubing having an outer diameter of 6.4 or 9.5 mm ($1/4$ " or $3/8$ "), and an inner diameter of 4.6 or 7.9 mm (0.18 " or 0.31 "). Five K-type thermocouples are spot-welded along the length of the test section to measure the tube surface temperature.

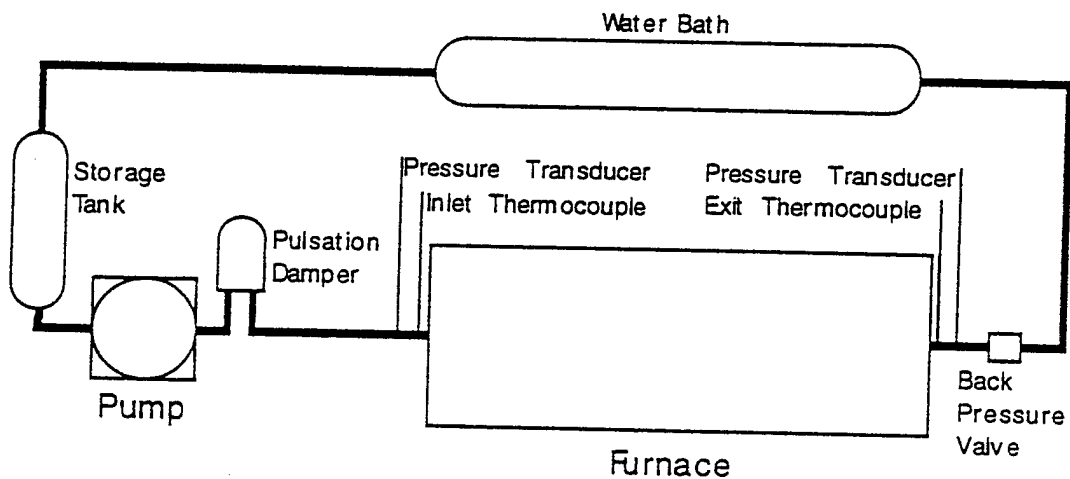


Figure 4-1. Experimental Setup

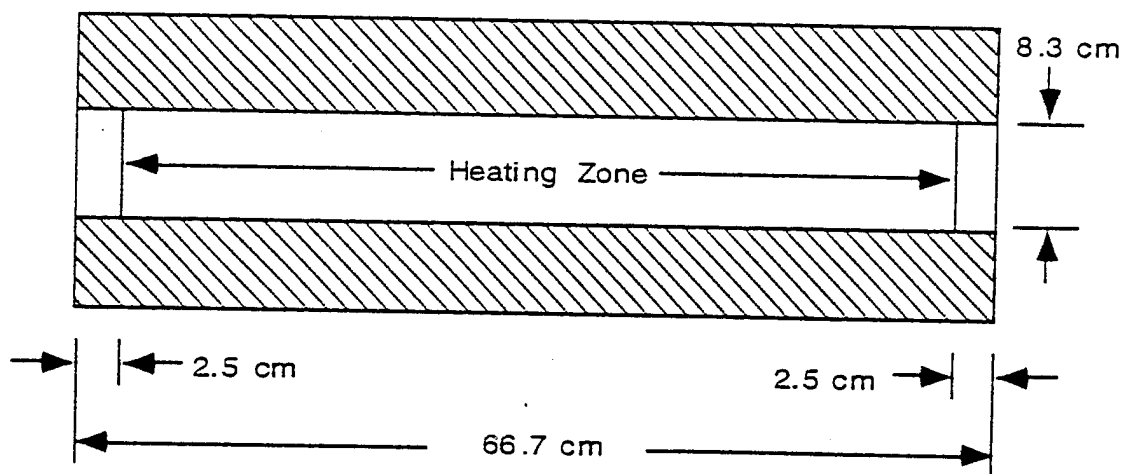


Figure 4-2. Furnace Dimensions

A back pressure valve near the furnace exit allowed the system pressure to be regulated. The hot fluid from the furnace is then passed through a water-bath heat exchanger to cool it down to room temperature, and finally back into the storage tank.

Direct measurements were made of the fluid pressure and temperature, as well as tube temperature and furnace wall temperature. The system pressure was measured with a static pressure transducer (Omega model PX 800-900GV) at the furnace inlet, and a second transducer (PCB Piezotronics model 113A24) at the furnace exit which measures dynamic behavior. Bulk fluid temperature is measured with fine-wire thermocouples inserted into the flow at the furnace inlet and exit. All measurements were taken by a computer based data acquisition system (Apple IIci with National Instruments MIO boards and software).

4.3 Procedure and Test Conditions

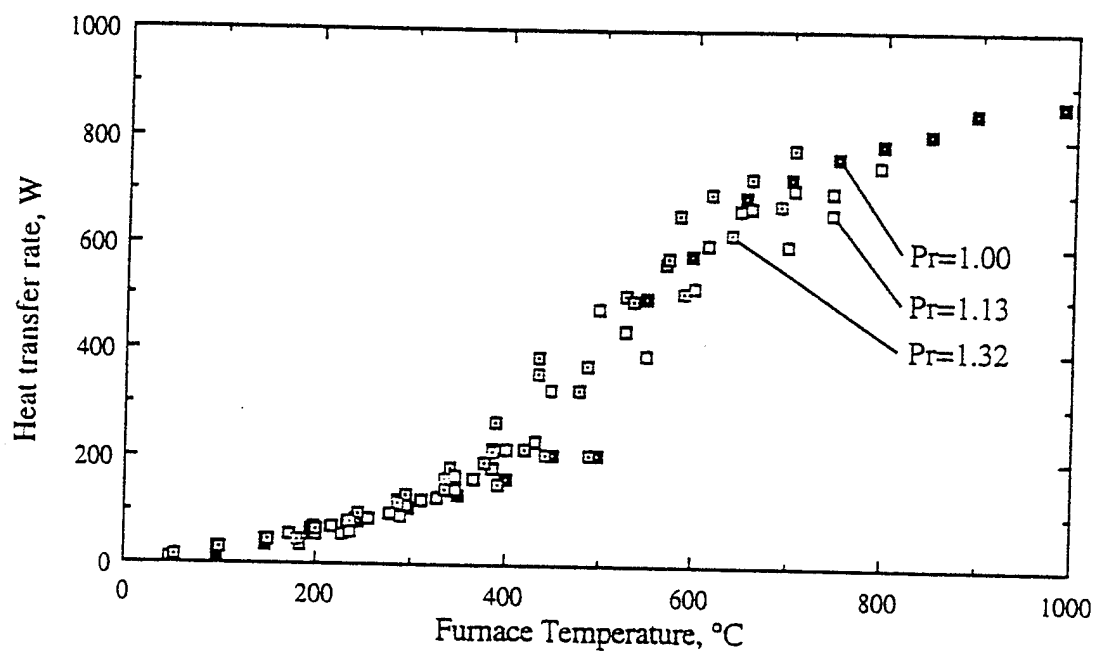
Tests were conducted by setting the flow rate and system pressure, and raising the furnace temperature in increments. Measurements of pressure and temperature were taken continuously by the computer, and once it had been determined that the system had reached steady-state, one set of measurements was stored in the data file. Once it was discovered that this process could be significantly accelerated by taking measurements of all pressures for a given furnace setting, the tests were conducted accordingly.

Two flow rates were used: 150 ml/min with the 7.9 mm I.D. tubing, and 450 ml/min with the 4.6 mm I.D. tubing. These flow rates correspond to inlet Reynolds numbers of about 2,000 and 10,000, respectively. Measurements were usually taken at pressures from 27.6 to 55.1 bar (400 to 800 psig), in increments of 6.9 bar (100 psig), in addition to a measurement at the critical pressure, 37.6 bar (531 psig). The highest furnace temperature used was 1000°C, which resulted in an average heat flux of about 90 kW/m² at a flow rate of 450 ml/min. Most tests were ended at a furnace temperature of around 800°C. Tests were conducted with both horizontal flow and upward flow.

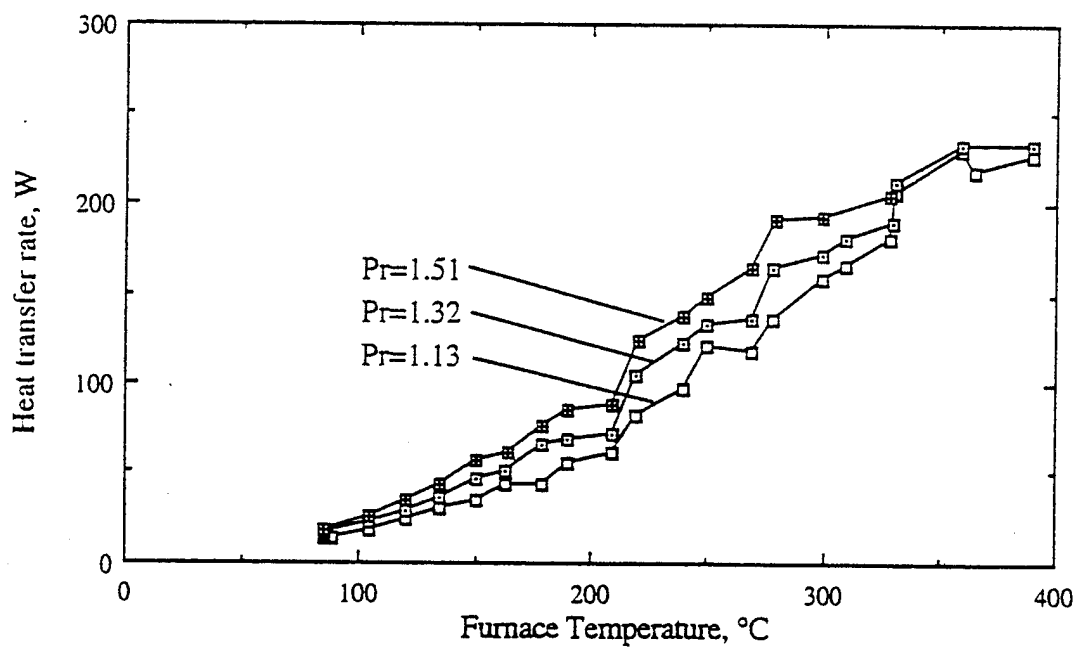
4.4 Experimental Results

The heat transfer results for the present experiments are presented as function of furnace wall temperature, rather than heat flux. The reason for this is as follows. The heat flux was controlled in these experiments through the furnace wall temperature. The magnitude of the heat flux was not known, however. Rough values could be calculated with radiation and convection correlations for concentric cylinders, but it was found that the heat flux was not uniform, due to a number of factors. Also, as with the jet fuel experiments, it is now believed that the simple model of a smooth, isothermal surface is inadequate for the real furnace wall, as the wall is composed of alternating rows of heating coils and ceramic wall material.

In order to compare heat transfer rates for various conditions, the rates were calculated based on the enthalpy increase of the fluid, and plotted versus furnace temperature. Figure 4-3a shows the results for an inlet Reynolds number of 10,000, various pressures, and the two flow directions. The data has a significant amount of scatter and shows no clear dependence on pressure or flow direction. Figure 4-3b shows the results for an inlet Reynolds number of 2,000. The data for the two different flow directions were similar, and were combined together. There is a slight dependence on pressure, however. A comparison between the two graphs show a slight, if any, influence of Reynolds number on the heat transfer rate. These results show that the furnace temperature is the dominating factor in determining heat transfer, but other factors, such as pressure and Reynolds number, could influence the rate for a given furnace temperature.



(a) $Re = 10,000$



(b) $Re = 2,000$

Figure 4-3. Heat Transfer Rates

4.4.1 Fluid Exit Temperature

The enthalpy increase of a heated fluid in a simple forced flow situation is equal to the heat added to the fluid. Thus, assuming a known and constant pressure, the temperature rise of the fluid will be directly related to the heat transfer through the enthalpy. For a given tube diameter and length, and a constant inlet temperature, the fluid exit temperature will be function only of the heat flux. The form of this function will be the same as that for fluid temperature versus enthalpy.

Figure 4-4 shows the fluid exit temperature versus furnace temperature for the conditions of horizontal flow at the rate of 450 ml/min through a 4.5 mm inner diameter tube. At very low heat fluxes, exit temperatures at all pressures increase steadily and there is little difference between pressures. At intermediate heat fluxes and low pressures, the exit temperature remains approximately constant and equal to the boiling point at each pressure. At supercritical pressures, the exit temperature increases steadily with increasing heat flux. At high heat fluxes, the exit temperature increases rapidly with increasing heat flux. Thus there is good qualitative agreement between the observed exit temperature and the calculated enthalpy of the fluid. Except for the critical point and the boiling points, which agree adequately, the data cannot be compared quantitatively because the heat flux is not known.

This relationship between fluid temperature and heat flux has led some researchers of supercritical heat transfer to present their results in the form of graphs of wall temperature vs. bulk enthalpy. This has the advantage of reducing two variables (heat flux and distance along the tube) into one.

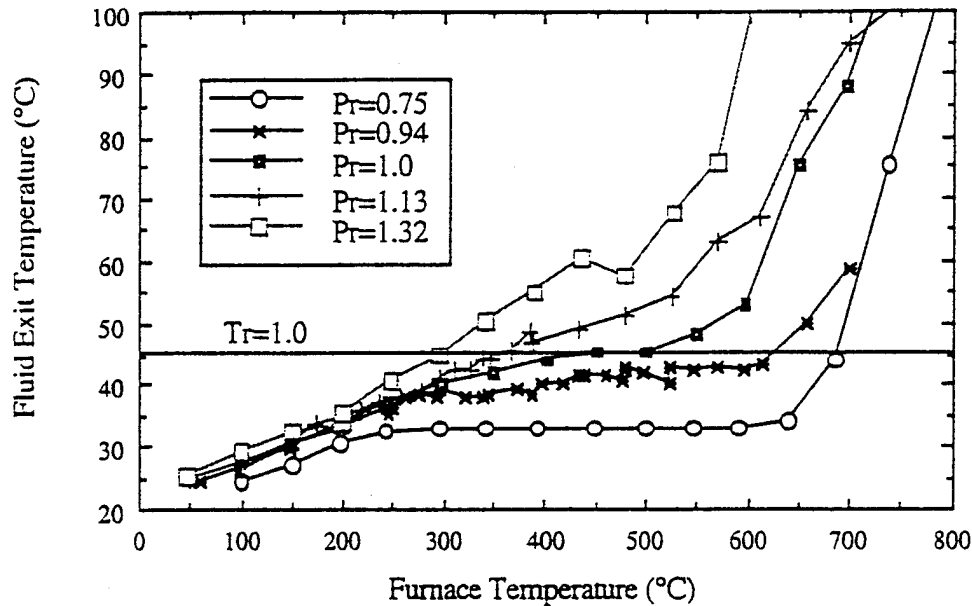


Figure 4-4. Bulk Fluid Temperature at Exit, Horizontal Flow, $Re = 10,000$

4.4.2 Tube Wall Temperature

The principal measurement of interest in determining the effectiveness of heat transfer under supercritical pressures is the tube surface temperature. Unfortunately, it is believed that local heat-flux-dependent errors were introduced into the tube surface temperature measurement by the thermocouples, especially with the smallest tubing. The wire thickness was fairly large (20 gauge), and the insulation covering the wires had a tendency to become frayed at the ends, exposing the wires. It is believed that these factors led to significant amounts of heat conduction to the tube through the thermocouple wires. These errors were minimized as much as possible, but were to a certain extent unavoidable, particularly with the smaller tubing.

These temperature errors were evident in jagged tube temperature profiles, rendering them of little value. However, if the tube temperature at a given location is plotted versus heat flux (bulk enthalpy), this may substitute for a plot of surface temperature versus distance. The closest surface thermocouple was 19 cm from the exit fluid thermocouple, but if these two measurements are compared under various conditions, a few qualitative observations can be made.

In comparing the results from horizontal and vertical flow, it will be useful to have an estimate of whether buoyancy effects are negligible. Hall and Jackson [6] cite the following experimentally determined criterion for negligible buoyancy effects in supercritical CO₂:

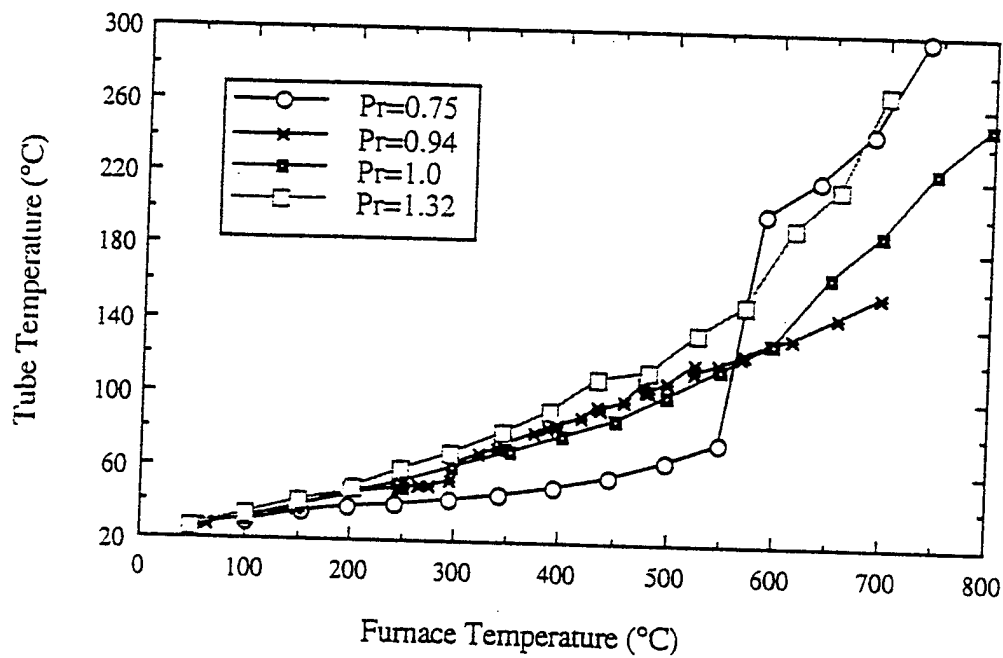
$$Gr_b/Re_b^{2.7} < 2.4 \times 10^{-5}$$

$$\text{where } Re_b = VD/\nu,$$

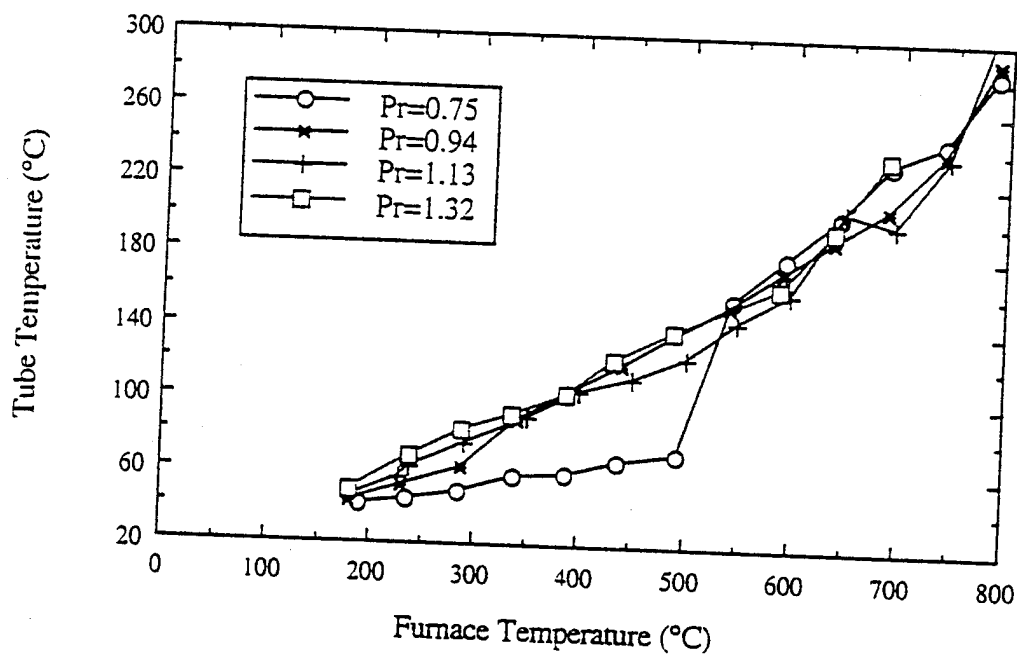
$$\text{and } Gr_b = (\rho_b - \rho_w)D^3g/\rho_b\nu^2$$

Calculating this property ratio is difficult because of the limited property data available for SF₆, but an estimate using a flow rate of 450 ml/min and a tube inner diameter of 4.6 mm, and property estimates at temperatures near the beginning of the tube, yields a value of about 2×10^{-4} , which indicates that buoyancy may play a role. On the other hand, a similar calculation using a flow rate of 150 ml/min, and a tube inner diameter of 7.9 mm yields a value of about 9×10^{-2} , indication with much more certainty that buoyancy should have an effect under these conditions. These two calculations correspond to inlet Reynolds numbers of 10,000 and 2,000, respectively.

Figure 4-5 shows a graph of the final tube surface measurement for the two sets with an inlet Reynolds number of 10,000. The horizontal flow graph corresponds to Figure 4-4. All of the temperatures increase fairly steadily for the most part. An important point is that for given flow conditions, the tube temperature will generally be higher for higher pressures. In cases where the wall temperature and fluid temperature span the pseudo-critical temperature, the increase of tube temperature with pressure could be due to the decrease of the peak in specific heat with increasing pressure. Under other conditions, the general increase in thermal conductivity may also play a role, allowing for greater heat transport across the boundary layer. However the viscosity increases in a similar manner to conductivity, and may decrease the turbulent transport.



(a) Horizontal Flow



(b) Upward Flow

Figure 4-5. Tube Temperature near the Exit, $Re \approx 10,000$

The exception to the trend is post-crisis subcritical heat transfer. At subcritical pressures, the tube temperatures exhibit a sharp increase, indicating some form of heat transfer crisis. Heat transfer after the subcritical crisis is probably determined by film boiling. If this is the case, it implies that the vapor layer against the wall provides lower levels of heat transport than the corresponding supercritical boundary layers.

At high heat fluxes (furnace temperature above about 600°C), Figure 4-4 shows that at all pressures for which data exist, the fluid exits the tube in a gas or gas-like state. Figure 4-5a for the same range shows that the tube wall temperature generally increases with increasing pressure, in conjunction with the increasing fluid temperature, which is consistent with single-phase convection. The data for $P_r = 0.75$, however, are higher than all of the rest in this range. As indicated above, this may be due to poorer heat transfer properties in subcritical vapor-like fluid. The data for $P_r = 0.94$ show a similar behavior at lower heat fluxes, but data at both subcritical pressures seem to increase more slowly than the supercritical data. Perhaps this is due to slower property variations with temperature in vapor than in vapor-like fluid.

At subcritical pressures, the tube surface starts out at lower temperatures than it does at higher pressures, but eventually jumps up to higher temperatures, giving evidence of a heat transfer crisis (cf. Figure 4-5). The tube surface in these low temperature regions is somewhat higher than the boiling point and tends to increase with increasing heat flux. This is especially noticeable at $P_r = 0.75$. Also, the jump at $P_r = 0.94$ occurs at almost the same time that boiling begins, suggesting that a heat transfer crisis occurs at low qualities. However, if nucleate boiling is occurring in the low temperature regions before the heat transfer crisis, the tube temperature should remain approximately constant at the boiling point. Perhaps this discrepancy is due to increasing thermocouple conduction error with increasing heat flux.

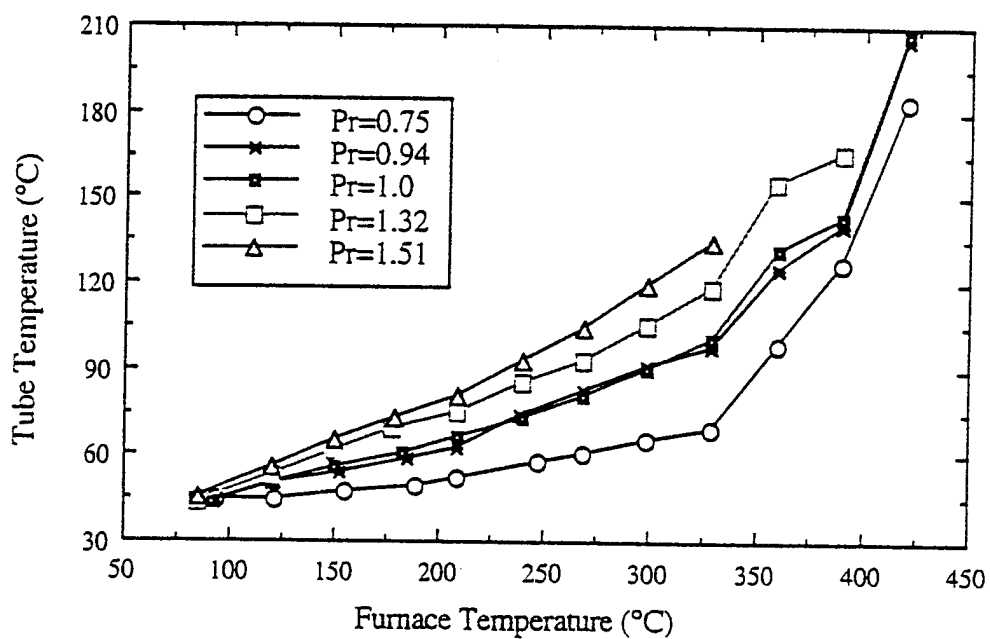
Figure 4-5b shows the results of a test under similar conditions as those for Figure 4-5a, except that the flow direction is vertically upward. Due to the high degree of scatter in the data, the results are difficult to interpret, but they generally are similar to the horizontal test. The temperatures for the upward test are slightly higher,

however. This agrees with the majority of existing data which indicate that heat transfer is degraded in buoyancy affected upward flow, but the results in this case may also be due to the hot air in the furnace tending to accumulate at the upward (exit) end of the furnace, where the last surface thermocouple was located.

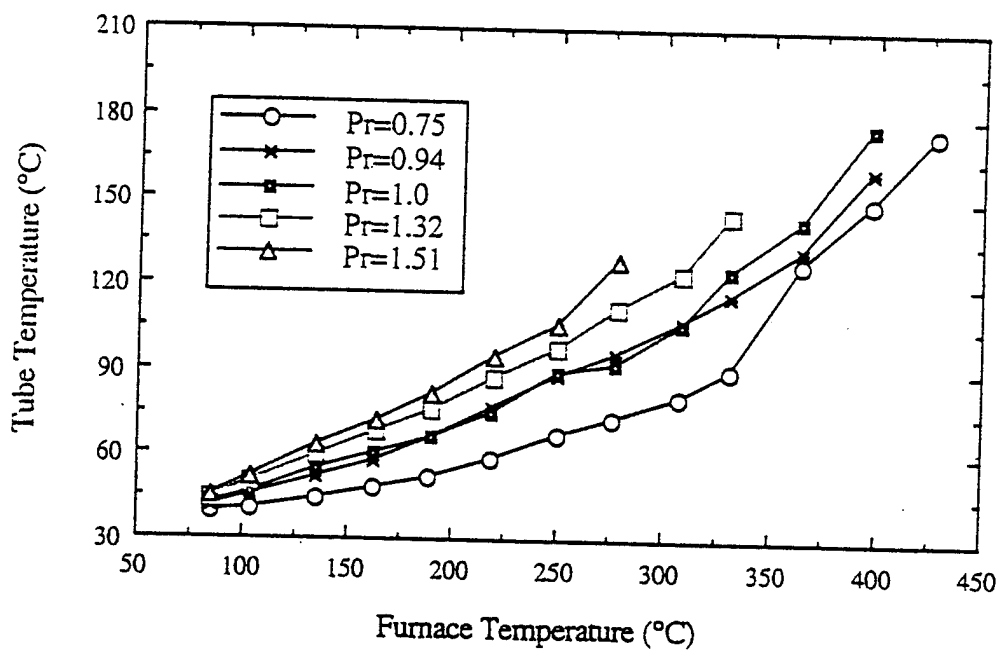
Figure 4-6 shows the results of tests with larger tubing and a slower flow rate ($Re=2,000$). The results are similar in general form, but the temperatures are much higher for a given furnace setting, due to the lower flow rate. Also, the heat transfer crisis seems to be much more gentle. It is not known why this would be, but perhaps it has something to do with buoyancy forces causing bubbles against the wall to rise and coalesce, allowing a smoother transition from nucleate to film boiling. The temperatures in the vertical test are noticeably higher than those for the horizontal test, in agreement with the prediction of significant buoyancy effects. Again, however, part of this increase may be due to increased air temperatures at the top of the furnace.

4.4.3 Pressure Oscillations

As with the jet fuel tests, no pressure oscillations other than those caused by the pump were observed. A calculation based on the enthalpy data for SF_6 indicates that the highest average heat flux achieved in these tests was about 90 kW/m^2 . Virtually all pressure oscillations recorded in the literature with non-cryogenic fluids occurred at heat fluxes greater than 1 MW/m^2 . Thus it is likely that the heat fluxes in the present tests were insufficient to cause the oscillations.



(a) Horizontal Flow



(b) Upward Flow

Figure 4-6. Tube Temperature near the Exit, $Re \approx 2,000$

5. VALIDATION OF MODEL FOR THERMOPHYSICAL PROPERTIES

The property model for calculating the viscosity, thermal conductivity, compressibility factor (for density calculation) and the real enthalpy of the fluid were incorporated into the code. This facilitates the computation of these quantities (as a function of reduced pressure and temperature) for a range of fluids in a general purpose manner. Also, a database consisting of a number of hydrocarbon species (with the respective properties) has been implemented. The code was used to perform calculations for a series of problems. The results are compared with experimental data from the literature. The description of each of these cases is provided below.

5.1 Properties of Carbon Dioxide

The critical point properties of carbon dioxide are:

$$p_c = 7.38 \text{ MPa}$$

$$T_c = 304.1^\circ\text{K}$$

The comparison for carbon dioxide is shown in Figure 5-1. The properties (density, viscosity, conductivity and enthalpy) of carbon dioxide (predicted by the model) are plotted as functions of temperature and pressure. It is observed that the properties predicted by the model are in close agreement with the data [7, 18, 24].

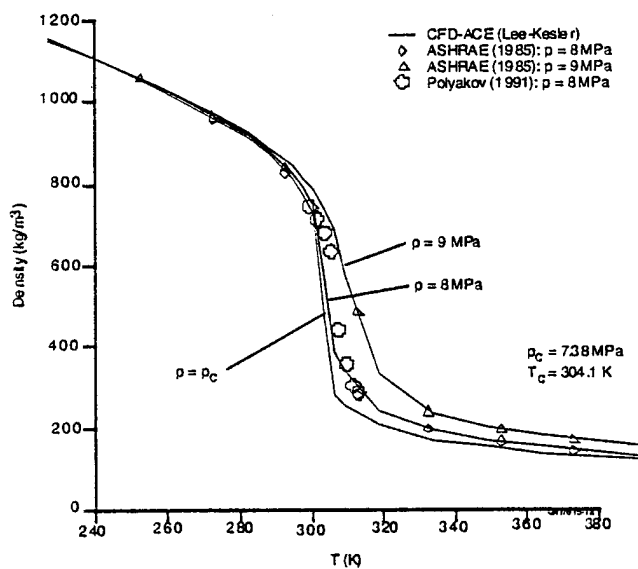


Figure 5-1a. Variation of Density with Temperature for CO₂

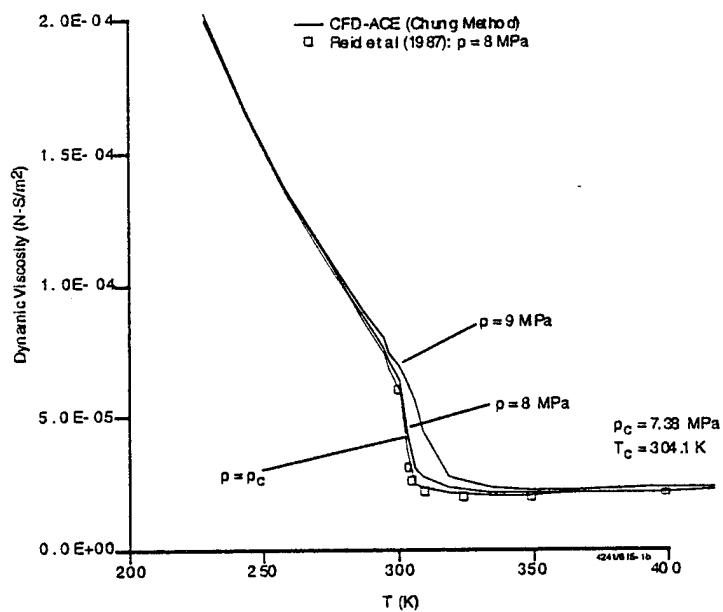


Figure 5-1b. Variation of Viscosity with Temperature for CO₂

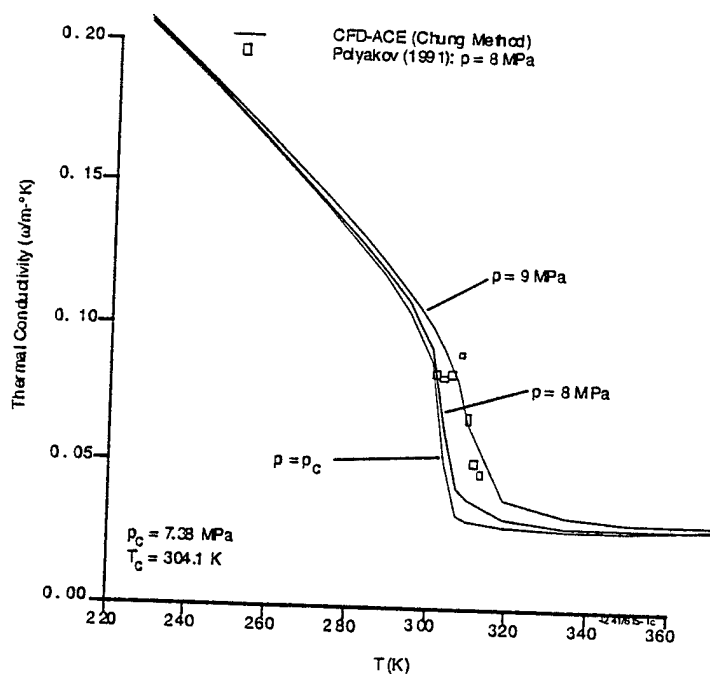


Figure 5-1c. Variation of Conductivity with Temperature for CO₂

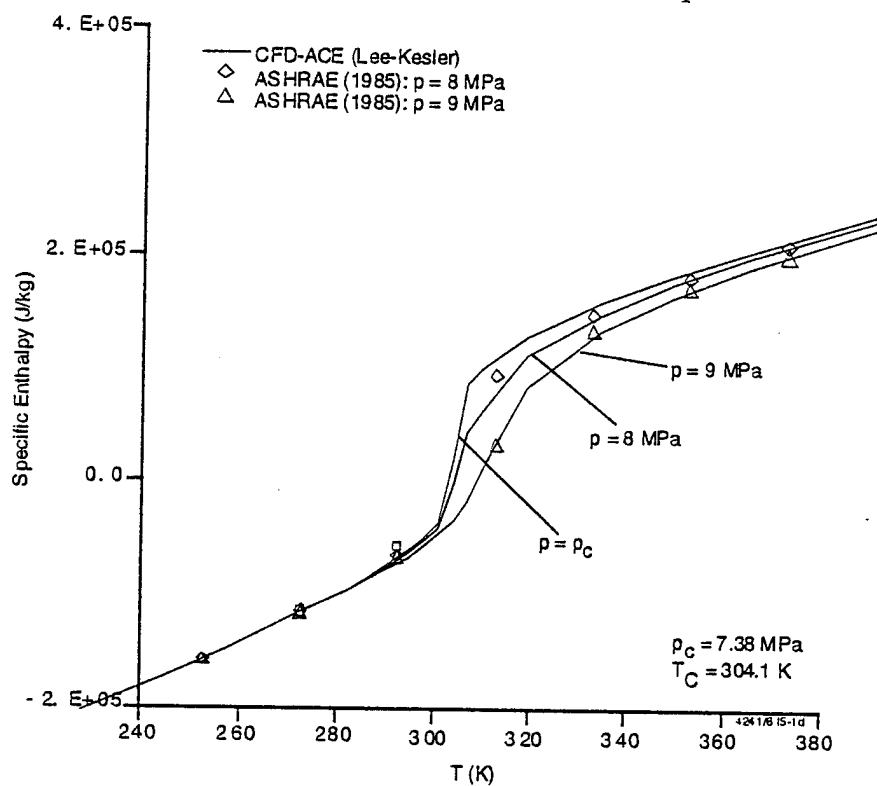


Figure 5-1d. Variation of Enthalpy with Temperature for CO₂

5.2 Properties of Propane

The critical point properties of propane are:

$$p_c = 4.25 \text{ MPa}$$

$$T_c = 369.8^\circ\text{K}$$

The properties (density, viscosity, conductivity and enthalpy) of propane (predicted by the model) is plotted as a function of temperature and pressure and is compared with data [18, 24] on propane (see Figure 5-2). It is observed that good agreement with data is obtained over the entire range of temperature and pressure.

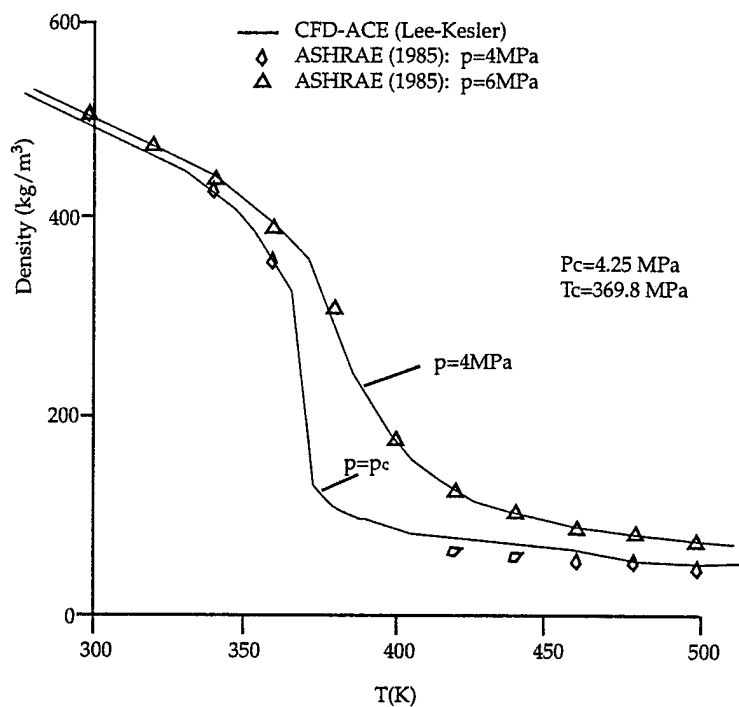


Figure 5-2a. Variation of Density with Temperature for Propane

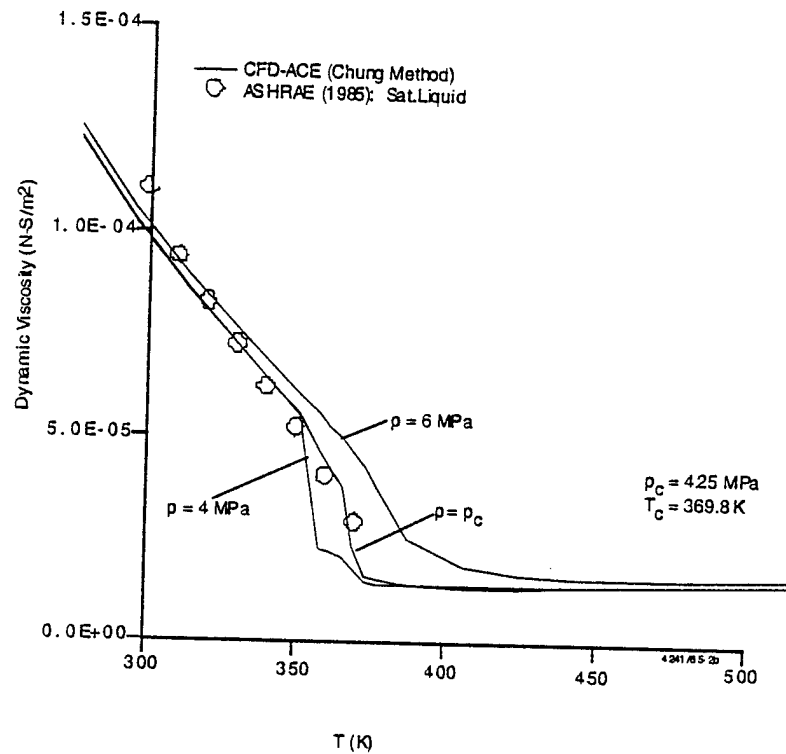


Figure 5-2b. Variation of Viscosity with Temperature for Propane

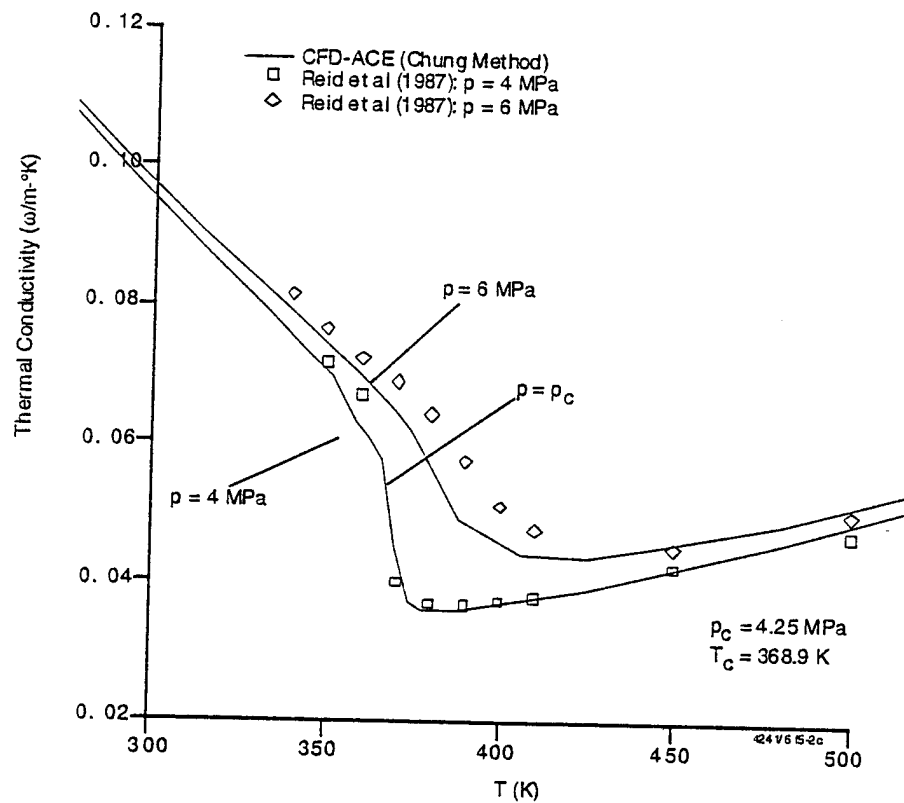


Figure 5-2c. Variation of Conductivity with Temperature for Propane

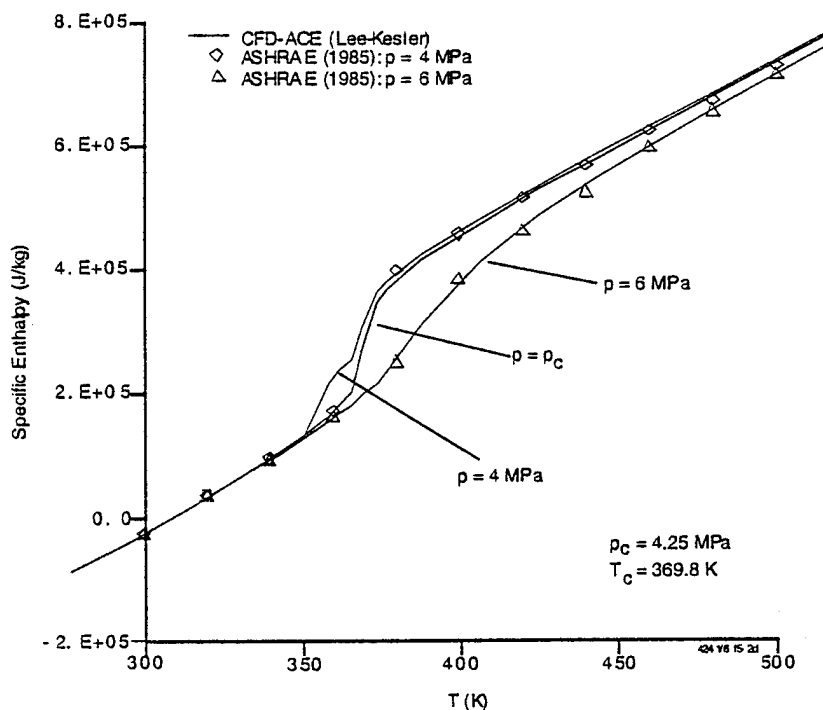


Figure 5-2d. Variation of Enthalpy with Temperature for Propane

5.3 Properties of JP-5

The critical point properties of JP-5 are:

$$p_c = 22.8 \text{ MPa}$$

$$T_c = 685^\circ\text{K}$$

The Comparisons for JP-5 are shown in Figure 5-3. Again, it is observed that the model prediction are in reasonable agreement with experimental data [25]. Deviation of model prediction for thermal Conductivity from data is observed for the high temperature regime.

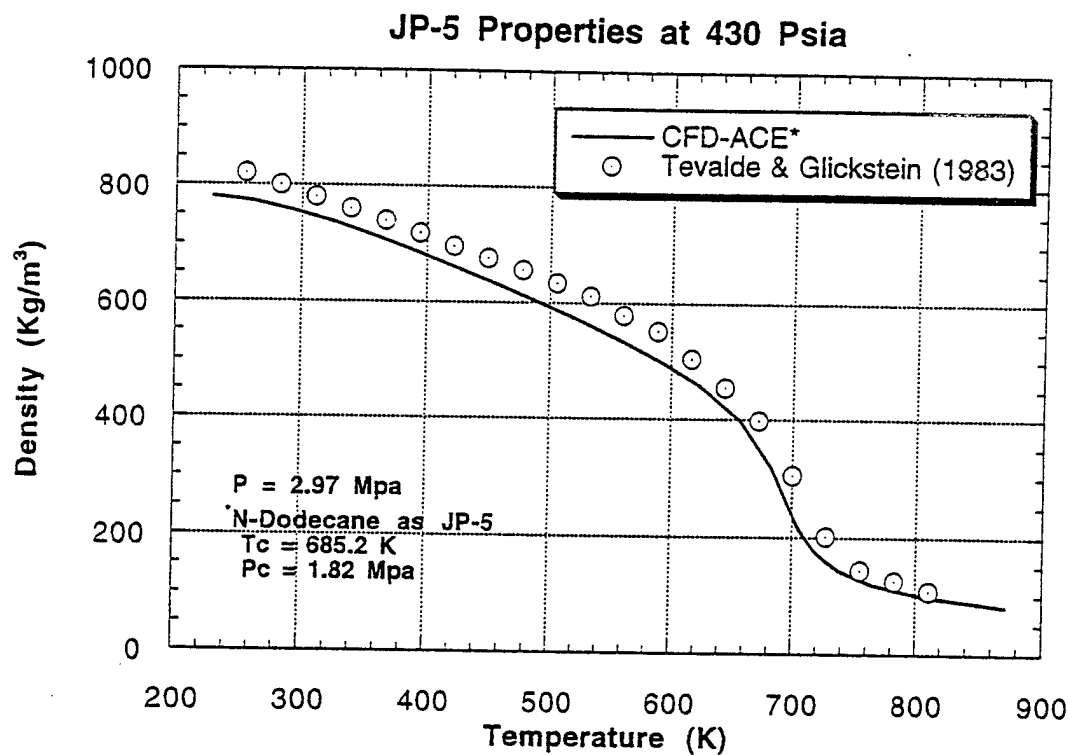


Figure 5-3a. Variation of Density with Temperature for JP-5

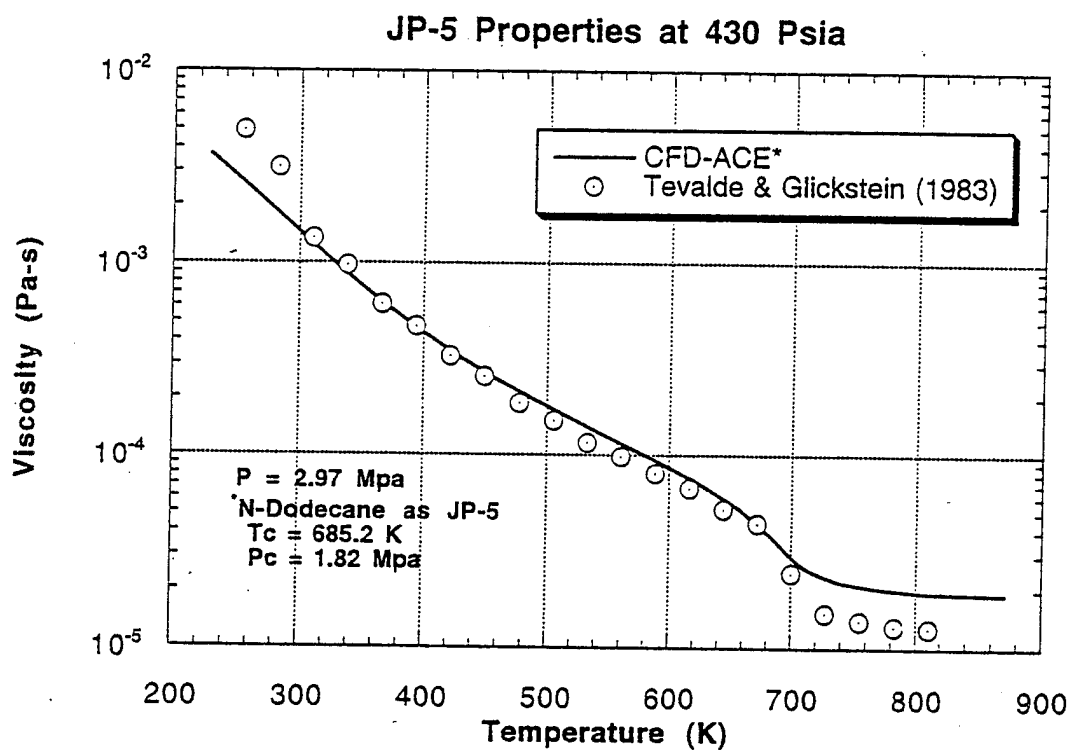


Figure 5-3b. Variation of Viscosity with Temperature for JP-5

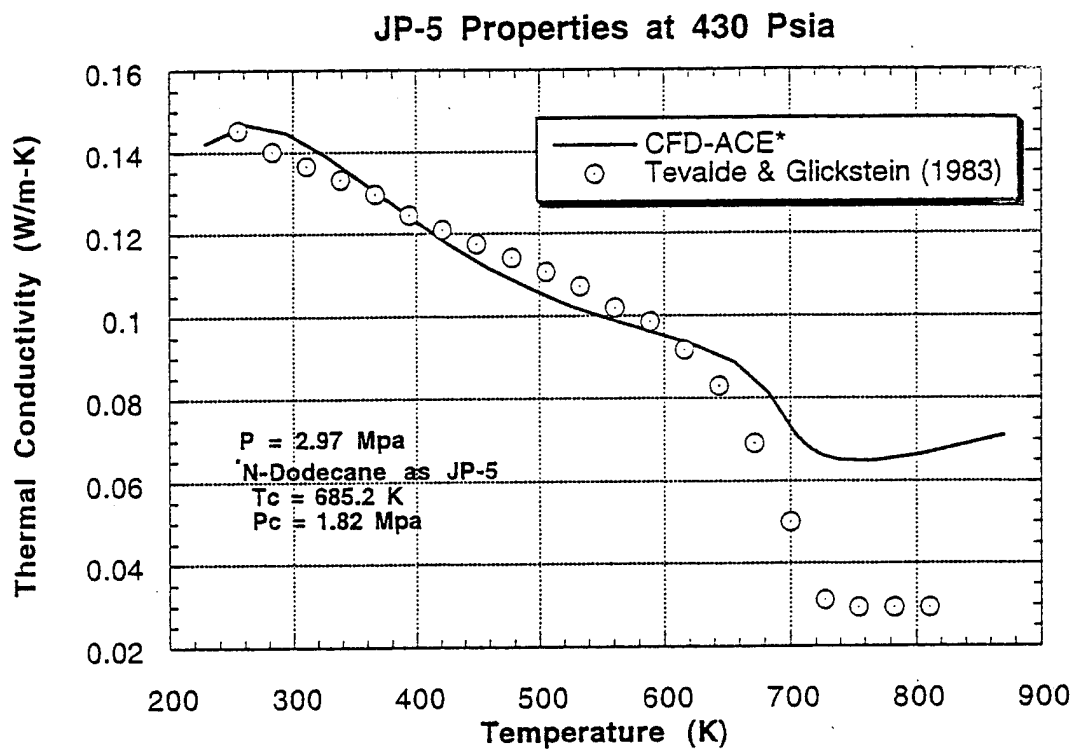


Figure 5-3c. Variation of Conductivity with Temperature for JP-5

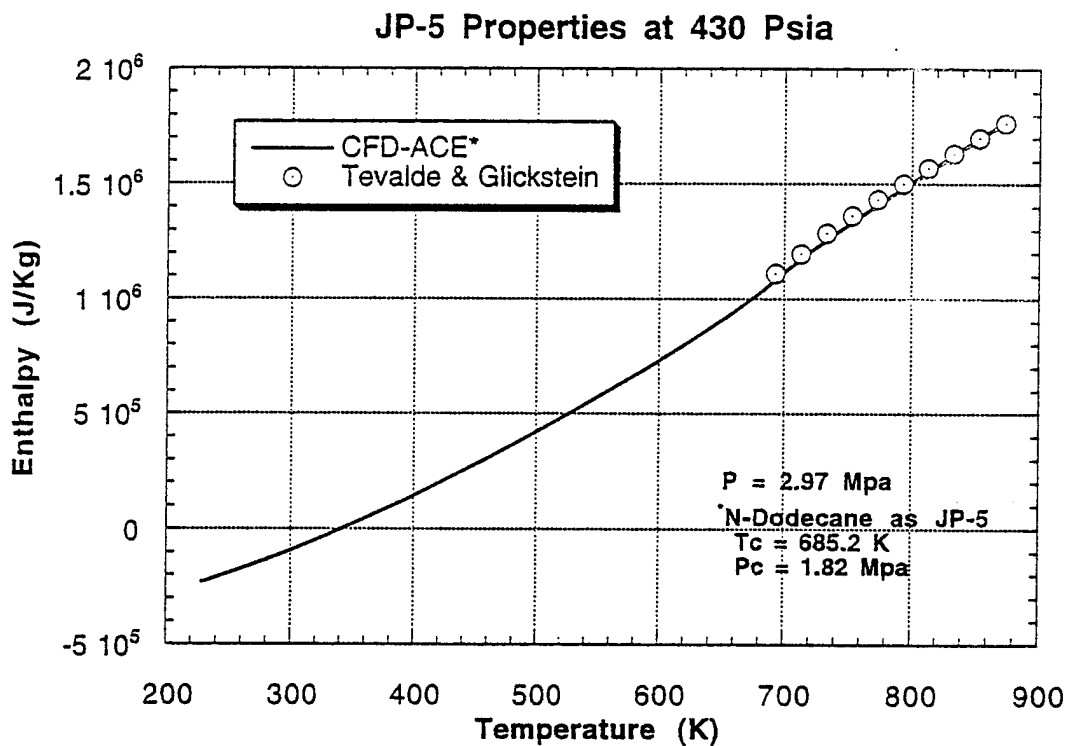


Figure 5-3d. Variation of Enthalpy with Temperature for JP-5

5.4 Properties of SF₆

The critical point properties of SF₆ are:

$$p_c = 37.6 \text{ MPa}$$

$$T_c = 318.7^\circ\text{K}$$

The comparisons for SF₆ with data [26] are shown in Figure 5-4.

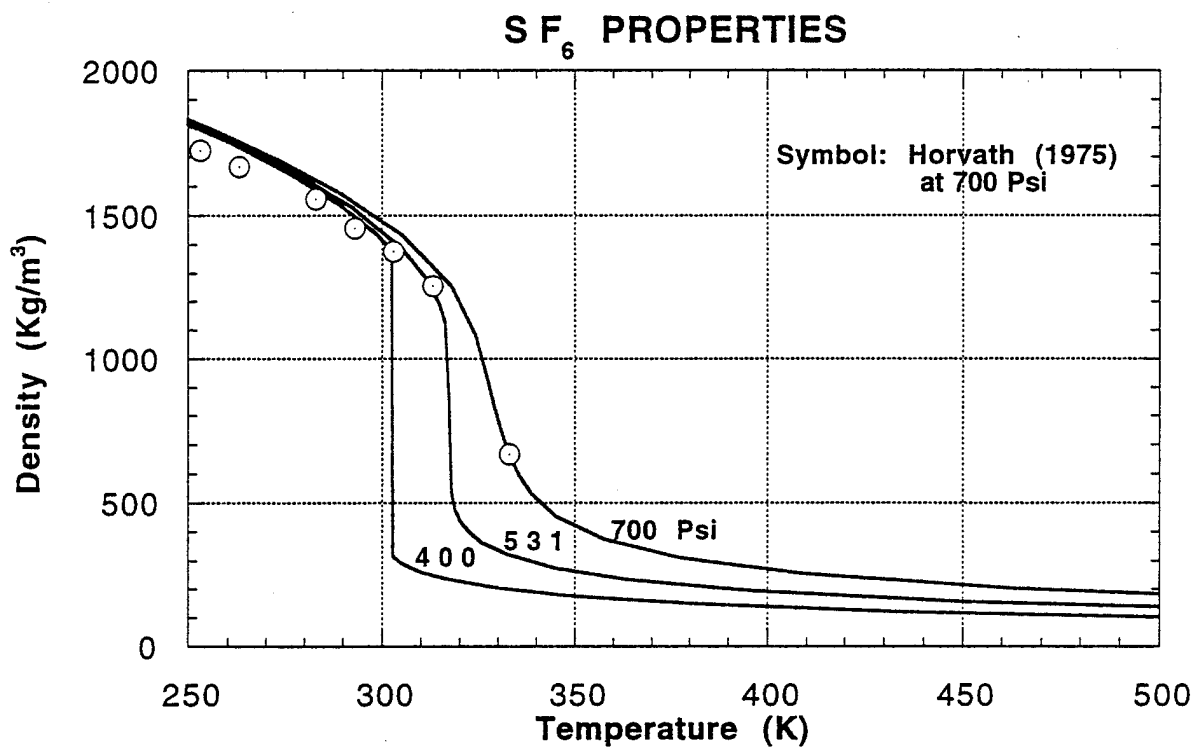


Figure 5-4a. Variation of Density with Temperature for SF₆

SF₆ Properties

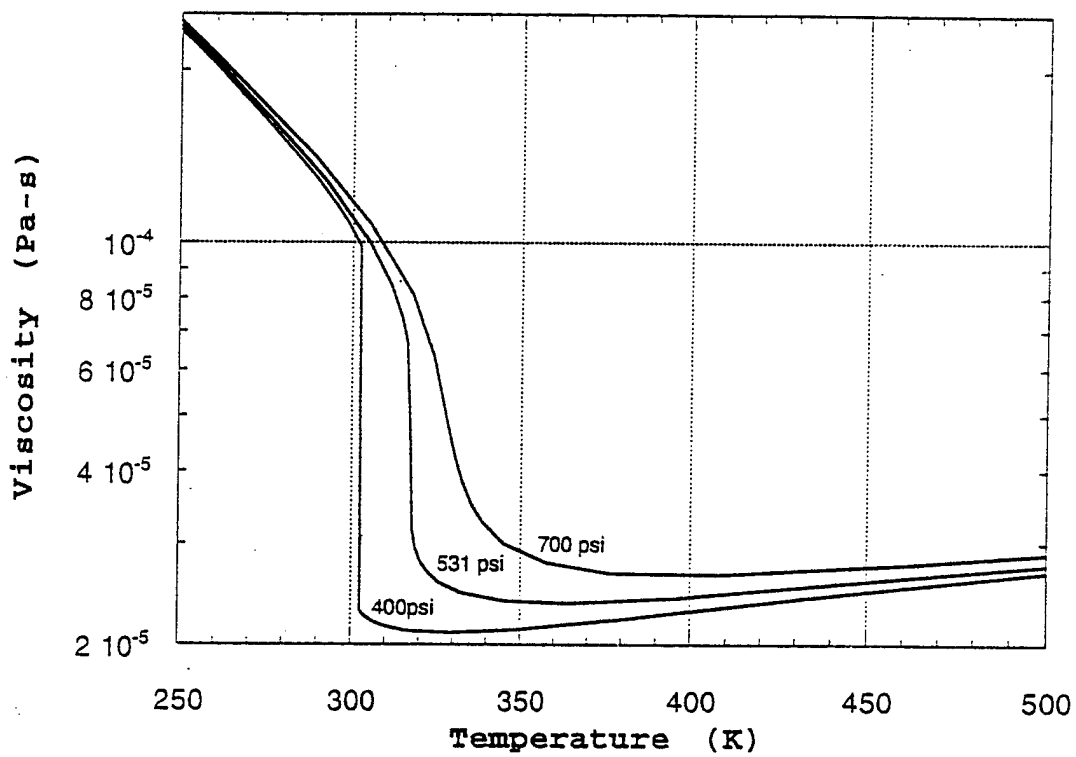


Figure 5-4b. Variation of Viscosity with Temperature for SF₆

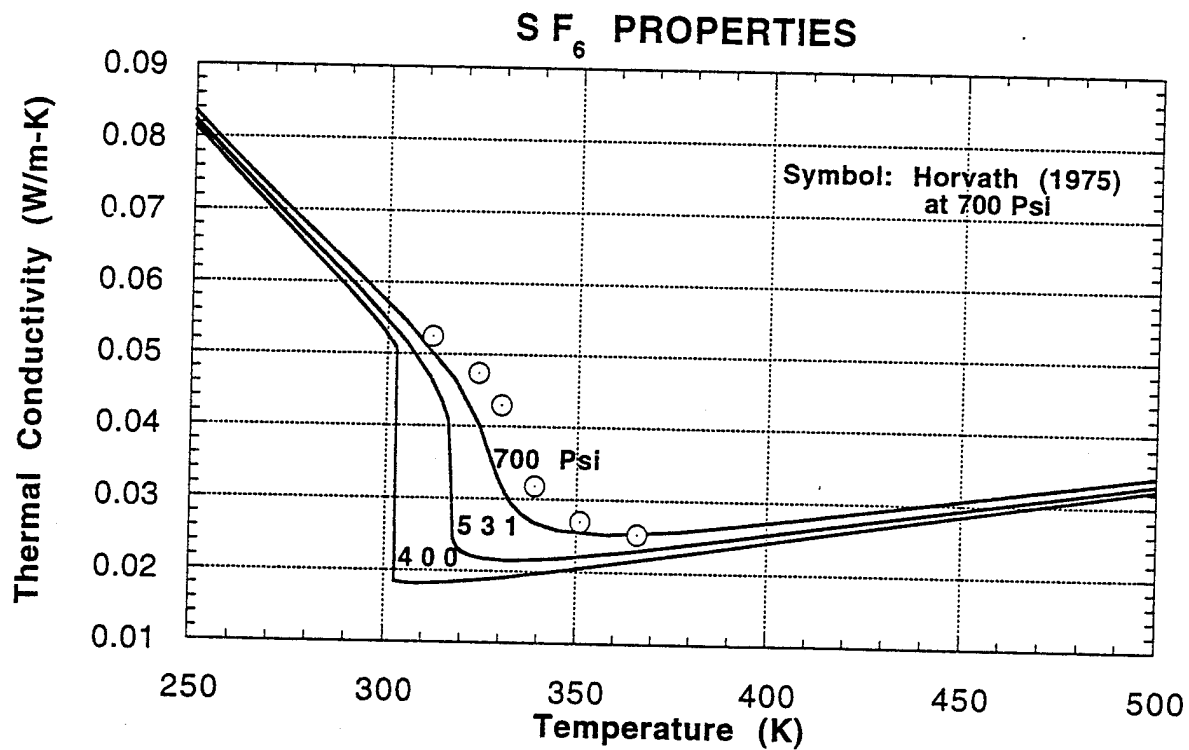


Figure 5-4c. Variation of Thermal Conductivity with Temperature for SF₆

SF₆ Properties

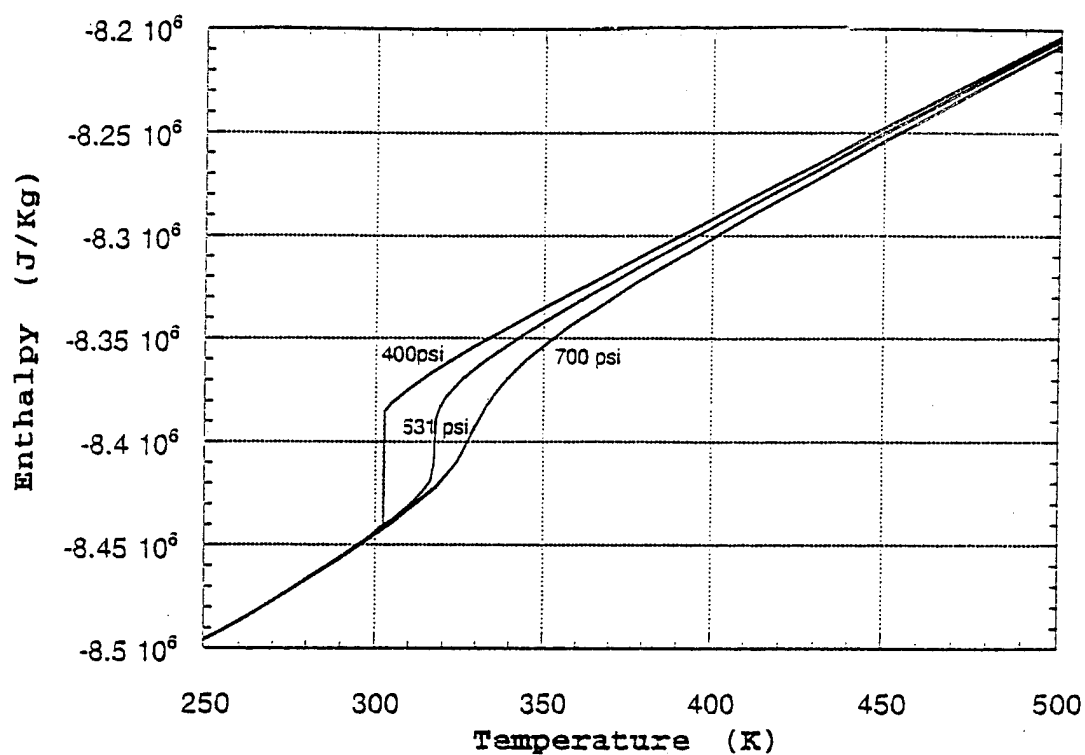


Figure 5-4d. Variation of Enthalpy with Temperature for SF₆

5.5 Summary

It is observed that the model is able to predict the quantitative trend in thermophysical properties as a function of temperature and pressure for a range of fluids. It is especially important to resolve the density variation since it influences the fluid dynamics significantly. Conductivity variations in the laminar sublayer have a significant influence on wall heat transfer.

6. ASSESSMENT OF TURBULENCE MODELS

The two layer model discussed in Section 2 is expected to provide better accuracy than the standard k - ϵ model without having to incur the computational expense of the low Reynolds number model. A series of test cases were simulated to assess the accuracy of the two-layer model against that of the standard k - ϵ model. Comparisons with experimental data are also presented. The first set of cases present the comparisons between the model for various fluid flow problems. The second set of cases focus on heat transfer predictions. For all the test cases considered, the near-wall grid clustering was maintained so that the first grid point away for the wall lies in the logarithmic layer for the standard k - ϵ model and in the laminar sublayer for the two-layer and low Reynolds number models.

6.1 Comparison of Fluid Flow Predictions

Fully Developed Channel Flow: The first case considered is the fully developed flow in a channel. The experimental data obtained by Laufer [27] is selected since it provides mean velocity as well as the turbulence quantities at three Reynolds number: 12300, 30800, and 61600. The Reynolds number is based on the centerline velocity and half-channel height. Only the results for the highest Reynolds number are presented here.

A schematic of the flow and the computational domain is shown in Figure 6-1. The velocity data is integrated to obtain the average velocity which is specified as the uniform velocity at the channel inlet. Thus the mass flow rates in the experiment and computation are maintained same. The channel is long enough for the flow to become fully developed. Though a 50X40 grid is used for both the models, the grid is uniform in both directions for the k - ϵ model and clustered near the wall for the two-layer model. Figures 6-2 and 6-3 show the mean velocity and turbulent kinetic energy across the channel. As can be seen, the agreement between the predictions and data is very good for the mean velocity. The peak turbulent kinetic energy, however, is significantly overpredicted by the two-layer model. This is consistent with predictions of most low Reynolds number models that integrate the k and ϵ equations up to the wall.

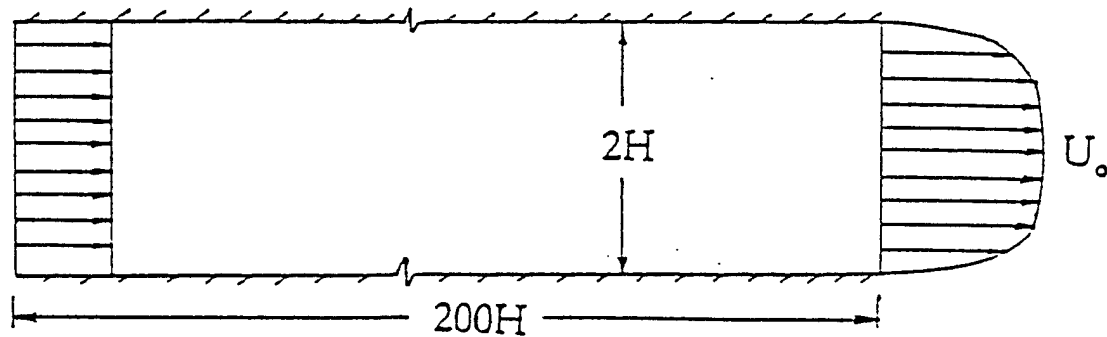


Figure 6-1. A Schematic of the Computational Domain

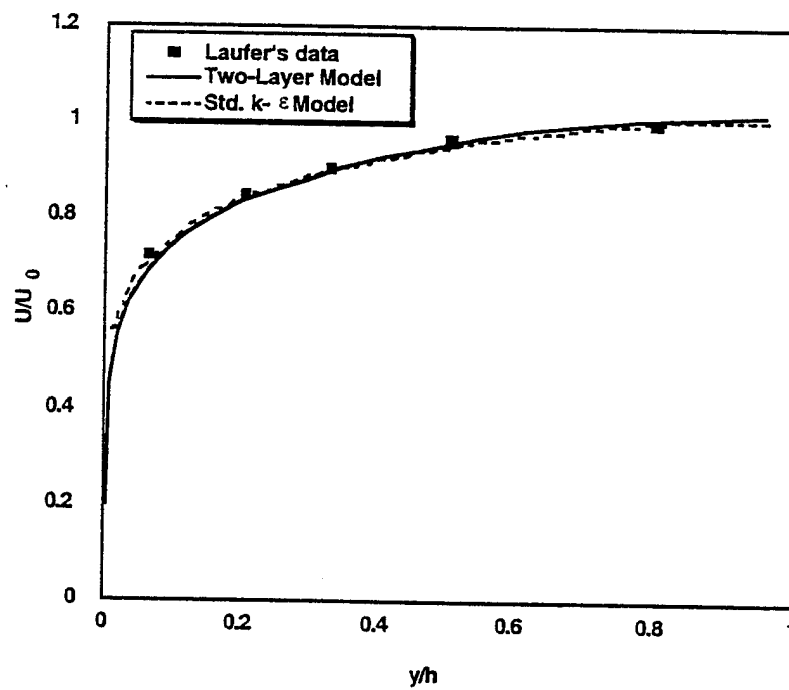


Figure 6-2. Variation of Mean Velocity Across the Channel

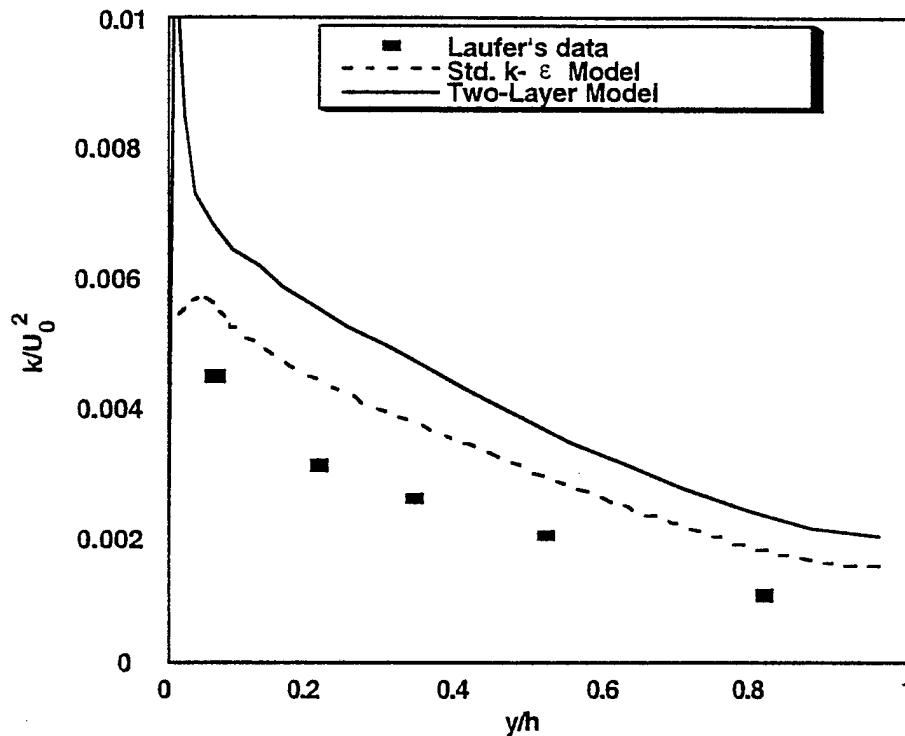


Figure 6-3. Variation of Mean Turbulent Kinetic Energy Across the Channel

Fully Developed Pipe Flow: The experimental data obtained by Laufer [28] is again used for validating the predictions. The grids used for this case are the same as those used in the previous case. Figures 6-4 and 6-5 compare the mean velocity and turbulent kinetic energy predictions with the data. Both the models predict the mean velocity accurately. The peak turbulent kinetic energy predicted by the k-ε model is lower than that predicted by the two-layer model. However, both models underpredict the kinetic energy compared to experimental data.

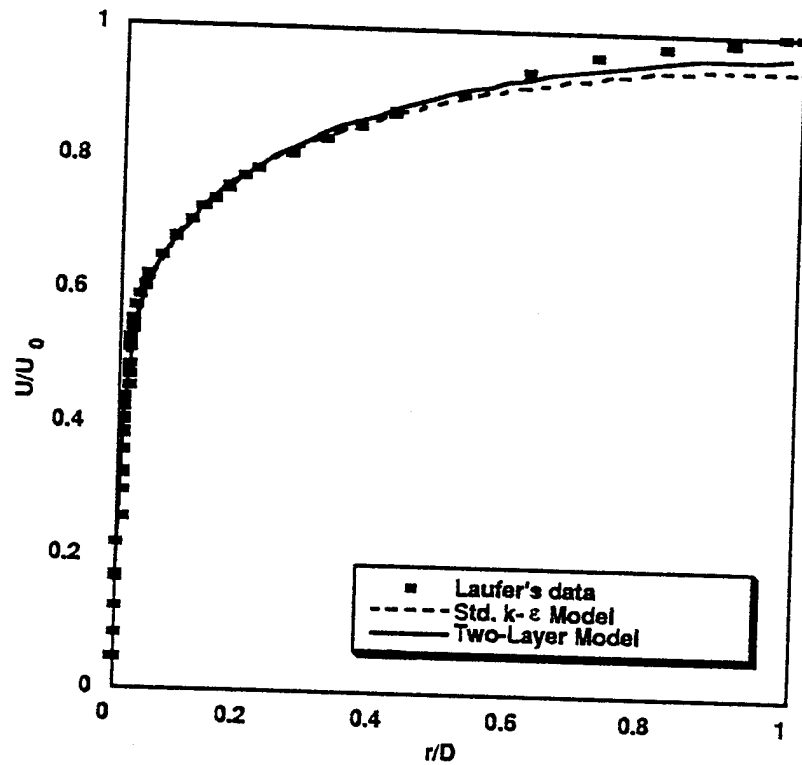


Figure 6-4. Mean Turbulent Velocity as Function of Pipe Radius

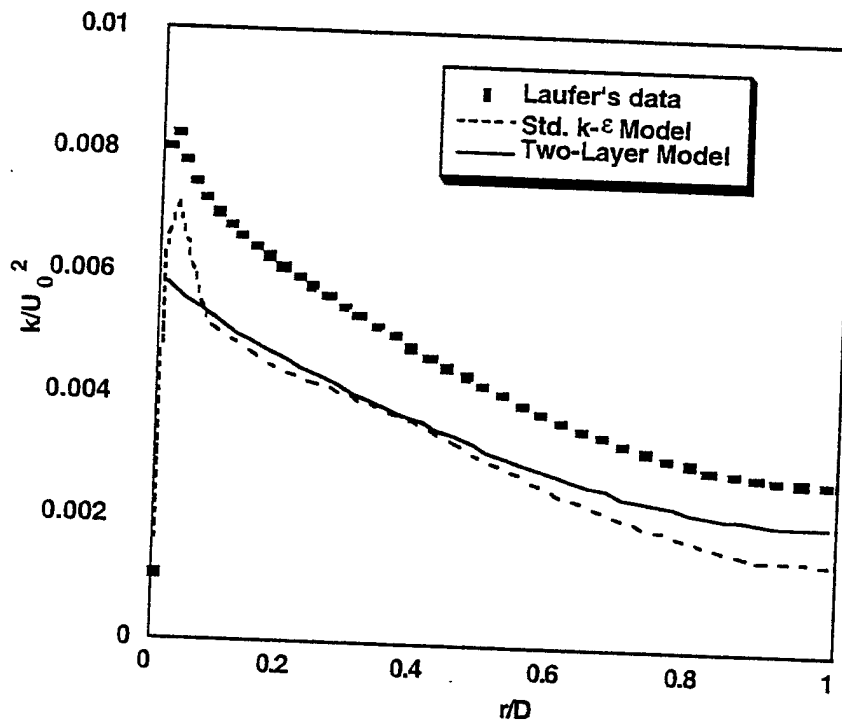


Figure 6-5. Mean Turbulent Kinetic Energy as a Function of Pipe Radius

Flow in Backward-Facing Step: The flow in backward-facing step has become a standard benchmark problem to validate the turbulence models since the 1980-81 AFOSR-HTTM Stanford Conference on Complex Turbulence Flows. The data obtained by Driver and Seegmiller [29] is used for validation. A schematic of the flow is shown in Figure 6-6. The expansion ratio (ratio of downstream channel height to upstream channel height) is 1.125 and the Reynolds number based on the step height is about 36000.

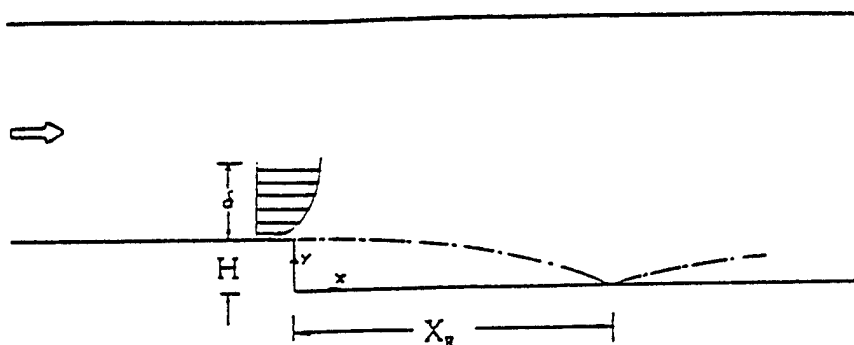


Figure 6-6. A Schematic of the Backward-Facing Step Flow

A 80X60 grid with clustering around the step is used. The clustering near the walls is finer for the two-layer model. The comparison of predicted reattachment length with the data is shown below in Table 6-1. Clearly, the two-layer model prediction of the attachment length is closer to the data.

Table 6-1. Comparison of Predicted Reattachment Length Using Various Turbulence Models with Data.

Model	Reattachment Length
Experimental Data	6.0
Standard k-ε	5.2
Two-Layer	5.6

Figures 6-7 and 6-8 show the static pressure and skin friction along the step wall. The static pressures predicted by both the models are identical. The discrepancy between the predictions and the data may be attributed to the underprediction of reattachment length. The predictions of skin friction by the models differ significantly. The two-layer model predicts the minimum value of skin friction in the recirculation region more accurately. However, it overshoots the data downstream of the reattachment point.

Flow in 180 Turnaround Duct: Flow in turnaround duct (TAD) is a popular validation case for CFD codes with body-fitted coordinate (BFC) capabilities. Flow in TAD is very useful for validating turbulence models because the flow contains boundary layers subjected to both convex and concave curvatures. Thus both the stabilizing and destabilizing effects of curvature on turbulence can be studied.

A schematic of the TAD is shown in Figure 6-9. The Reynolds number based on duct height and the bulk velocity is about 86000. The data obtained by Sandborn [30] is used for validation. Uniform flow is prescribed at the inlet and a constant pressure is specified across the exit. A 80X60 grid with clustering around the bend is used. Figure 6-10 shows the static pressure variation along the inner and outer walls. Pressure recovery downstream of the bend is captured better by the two-layer model. Figures 6-11 through 6-13 show the mean velocity profiles at 0, 90, and 180 around the bend. Note that the two-layer model predicts separation at the inner wall at 180 position, a feature not captured by the standard k- ϵ model.

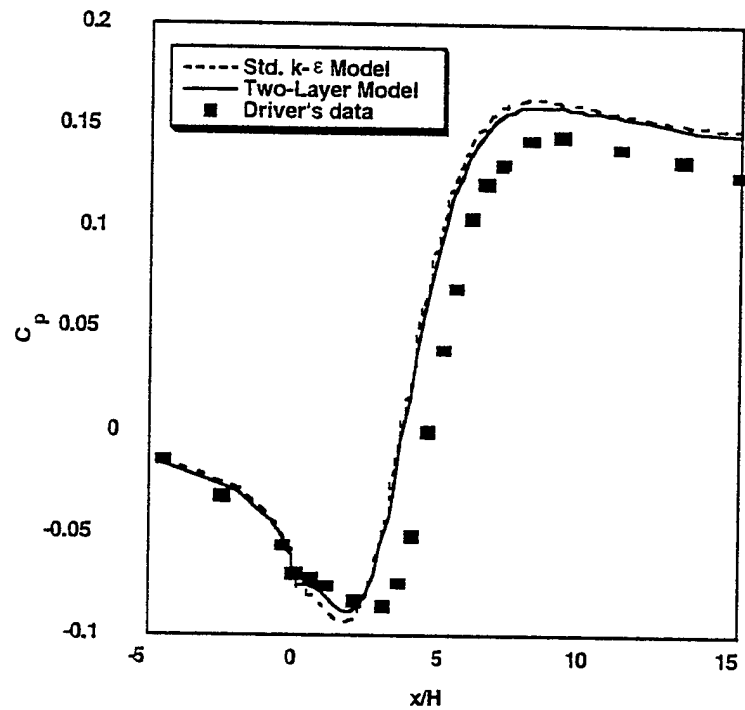


Figure 6-7. Static Pressure Variation Along the Step Wall

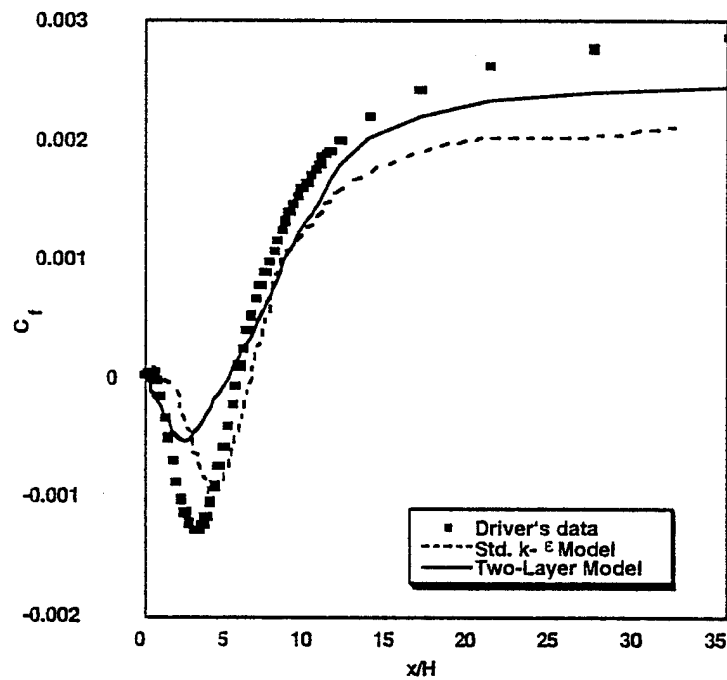


Figure 6-8. Variation of Skin Friction Coefficient Along the Wall

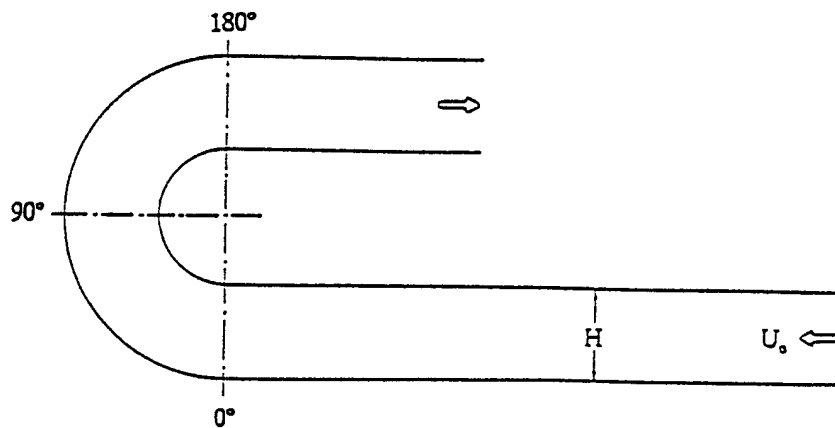


Figure 6-9. A Schematic of the Turn Around Duct Flow

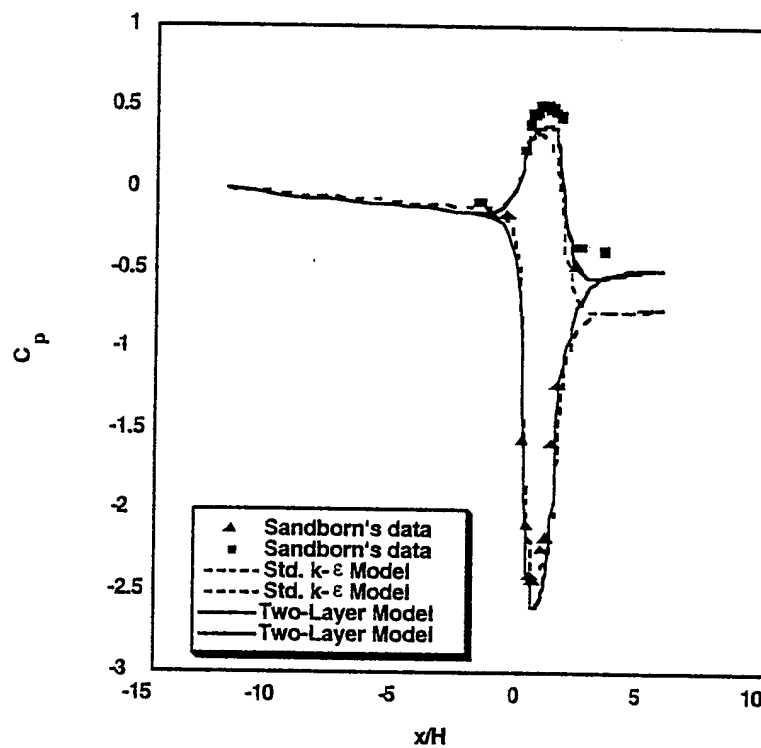


Figure 6-10. Static Pressure Variation Along the Inner and Outer Walls

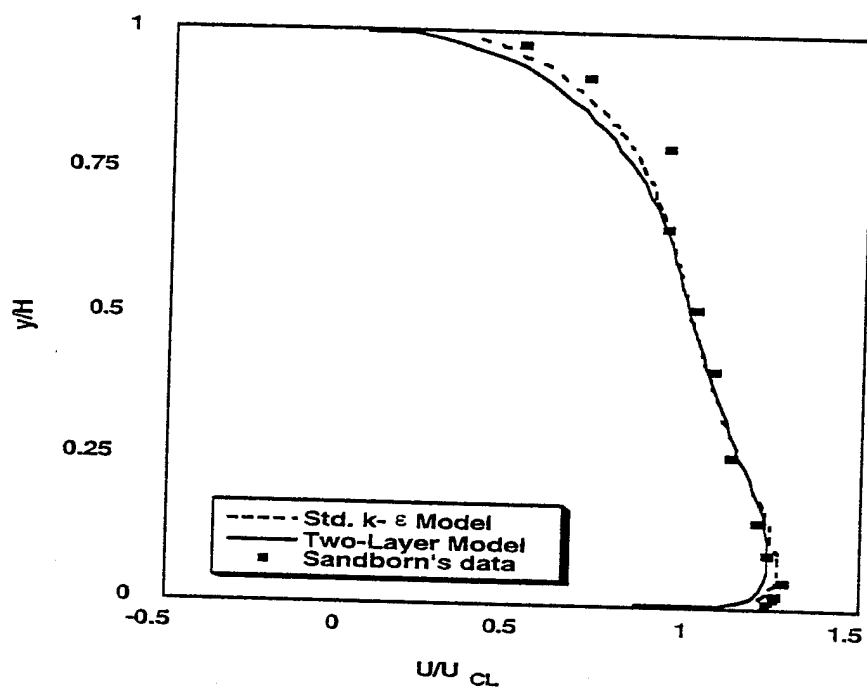


Figure 6-11. Mean Turbulent Velocity Profile at 0

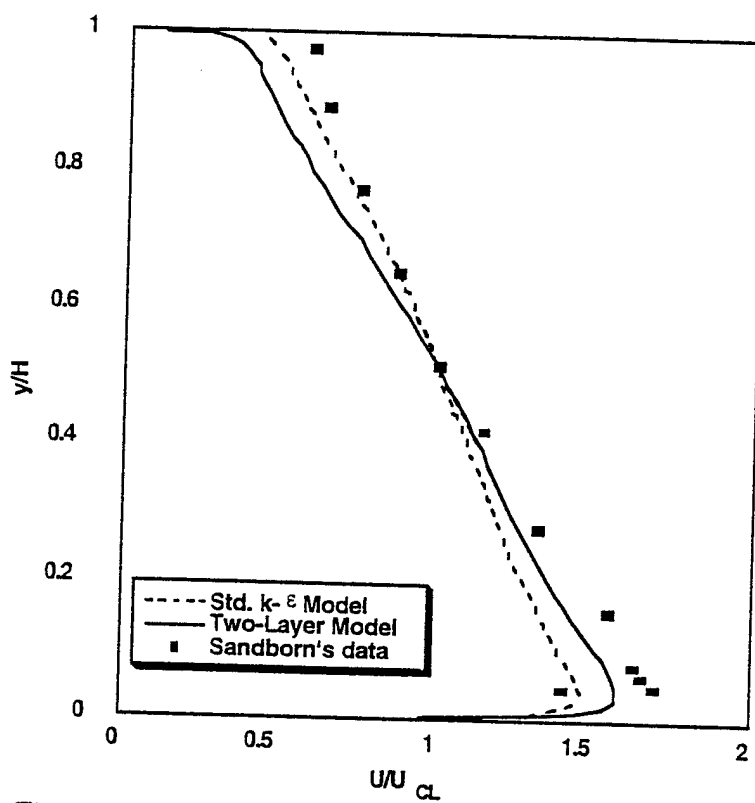


Figure 6-12. Mean Turbulent Velocity Profile at 90

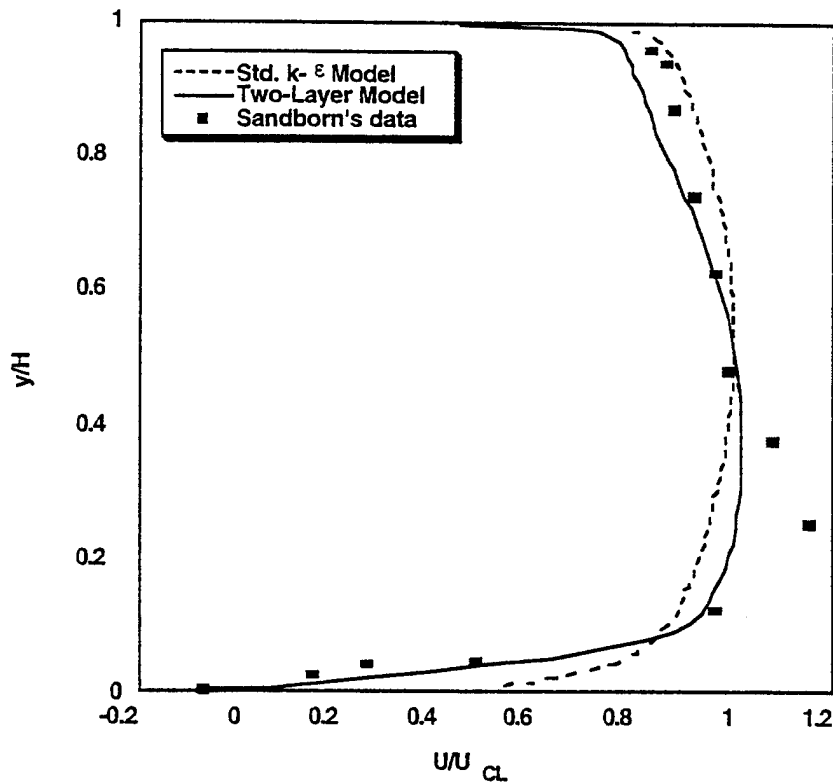


Figure 6-13. Mean Turbulent Velocity Profile at 180

Flow in Rotating Disk Cavity: This case tests the turbulence models for swirling and rotating flows. The flow domain, shown in Figure 6-14 consists of a cavity enclosed by a stator and a rotor in the axial direction and by the shaft and a shroud in the radial direction. Daily and Nece [31] obtained mean velocity data for a disk spacing ratio (ratio of cavity width to outer radius) of 0.0637 at a rotational Reynolds number of 4.4×10^6 . A 40×60 grid clustered near the walls is employed.

The torque coefficient is a measure of the accuracy of the skin friction predictions. Table 6-2 below compares the predictions with the data. Figures 6-15 and 6-16 show the axial variation of radial and tangential velocity components at a radial location (non-dimensional) of 0.765. The predictions are in good agreement with the data.

Table 6-2. Comparison of Torque Coefficient Prediction With Data

Model	Torque Coefficient $\times 10^3$
Data	4.0
Standard k- ϵ	3.6
Two-Layer	4.6

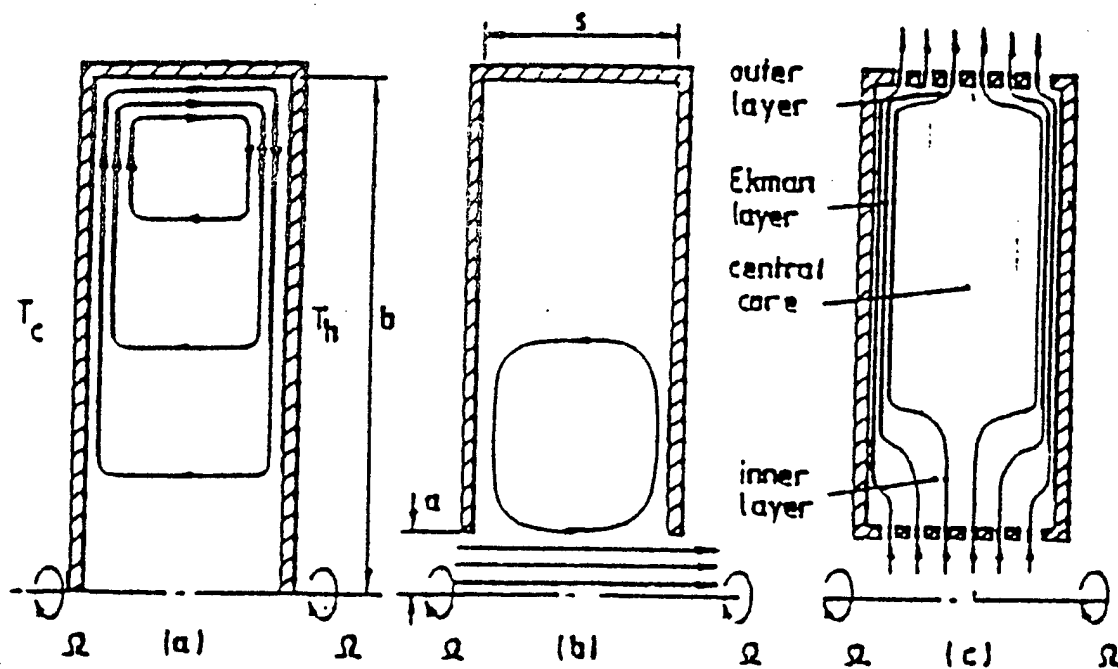


Figure 6-14. Schematic of the Flow in Rotating Disk Cavity (a) sealed cavity; (b) cavity and axial throughflow; (c) cavity with radial outflow

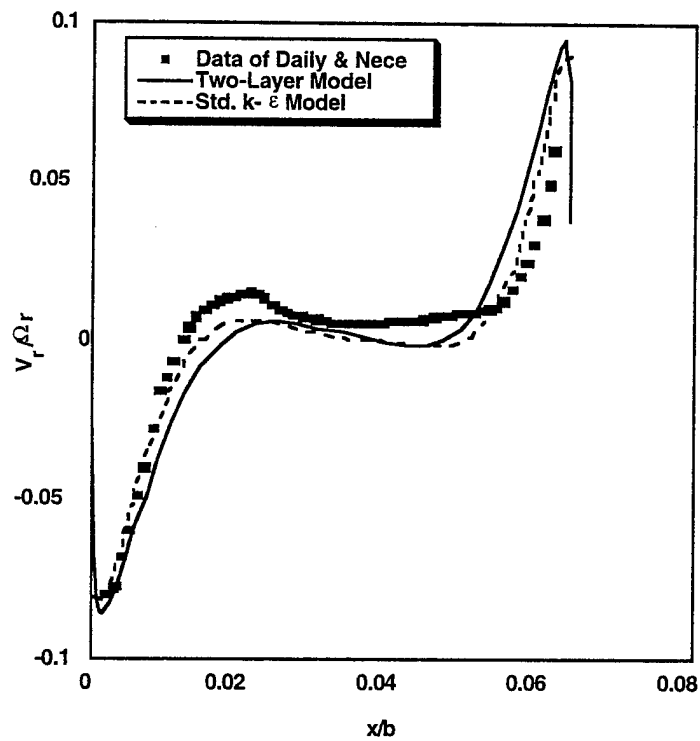


Figure 6-15. Axial Variation of Radial Velocity

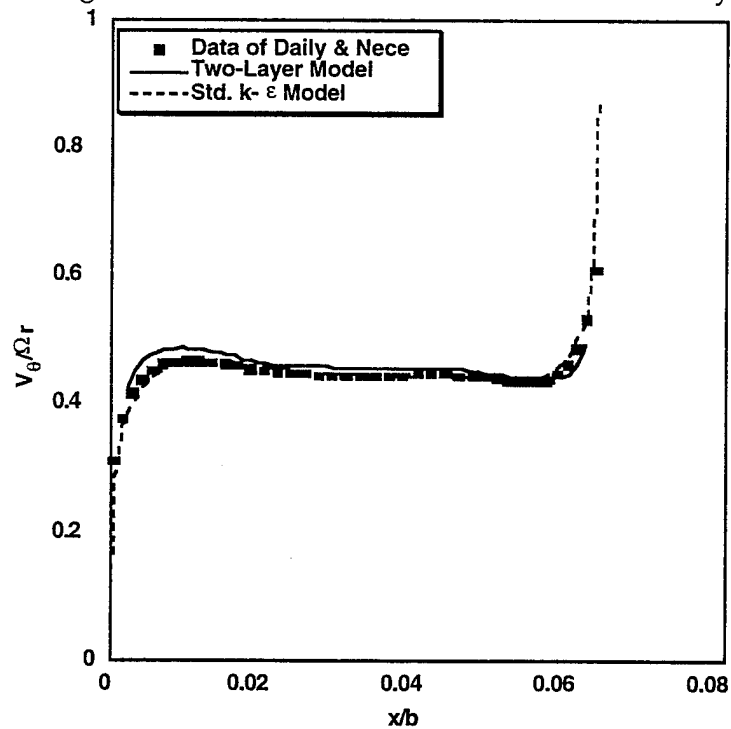


Figure 6-16. Axial Variation of Tangential Velocity

6.2 Comparison of Heat Transfer Predictions

A point to be noted is that the analog of the two-layer model for heat transfer does not exist. Prior applications and validations of this model have been limited to isothermal turbulent flows or to flows with small temperature and property gradients near the wall. Due to this limitation, the thermal wall functions of the standard k - ϵ model were used (in this study) in conjunction with the two-layer model to calculate heat transfer at the wall.

As discussed before, the two-layer model is expected to provide the same level of accuracy as the low Reynolds number model but at a lower computational cost. In other words, it is expected to be more accurate than the standard k - ϵ model without additional computational expense. Therefore, by definition, one would expect the predictions of the two-layer model to lie in between the prediction of the standard k - ϵ model and the low Reynolds number k - ϵ model. The results in the previous section show that this is indeed true for the prediction of pressure coefficient, skin friction coefficient and mean velocity profiles in turbulent incompressible, isothermal flows. The comparisons for heat transfer are shown below.

The flow of CO_2 in a two dimensional channel is considered. The channel pressure is 7.58 MP_a which is above the critical pressure ($P_c = 7.38 \text{ MP}_a$) of CO_2 . The inlet temperature is 288°K which is below the critical temperature ($T_c = 306.1^\circ\text{K}$) of CO_2 . The channel wall is heated and the fluid undergoes transition to the fully supercritical regime in the channel. The flow of CO_2 is upward, i.e., against the direction of gravity. This problem is discussed in greater detail in the next section (see Figure 7-1).

Constant Wall Temperature Case: Figure 6-17a shows the heat flux values predicted by the three turbulence models for a constant wall temperature of 320°K . the computational grid for the two-layer model was the same as that for the standard k - ϵ model. It is observed that the heat transfer rates predicted by the two-layer model do not lie in between the values predicted by the standard and low Reynolds number k - ϵ models.

Constant Heat Flux Case: Another case was simulated with a constant heat flux of 30 kW/m^2 applied to the sidewalls. Again, it is observed (see Figure 6-17b) the predictions of the two-layer model do not lie between those of the standard k- ϵ model and the low Reynolds number model. Two different runs were performed with the two-layer model, one with the same grid resolution as the standard k- ϵ model and the other with the same grid resolution as the low Reynolds number model. Both simulations yielded results that were less accurate than the standard k- ϵ model predictions.

The main reason for this discrepancy appears to be the lack of an appropriate analog for wall heat transfer in the two-layer model. This feature seriously limits the application of the two-layer model to turbulent flow involving heat transfer. Therefore all turbulent flow calculations presented in the following sections of this report were done using the low Reynolds number model. Although the computational expense of this model is relatively high, its ability to resolve near wall property variations as well as the lack of any limiting assumptions (such as wall functions) makes it a good candidate for modeling turbulent flows of supercritical fluids.

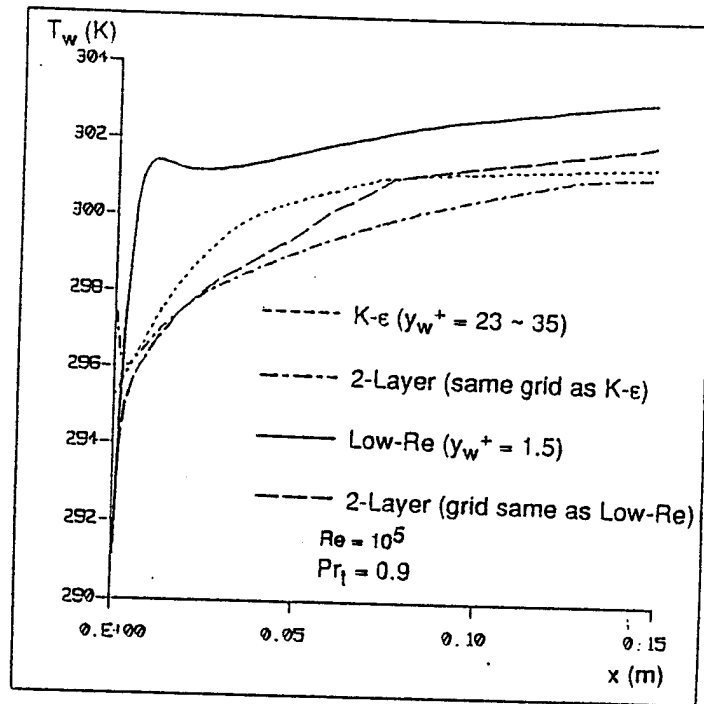


Figure 6-17a. Comparison of Heat Flux Predictions from the Three Turbulence Models for Upward Flow in the 2-D channel with $T_w = 320^\circ\text{K}$

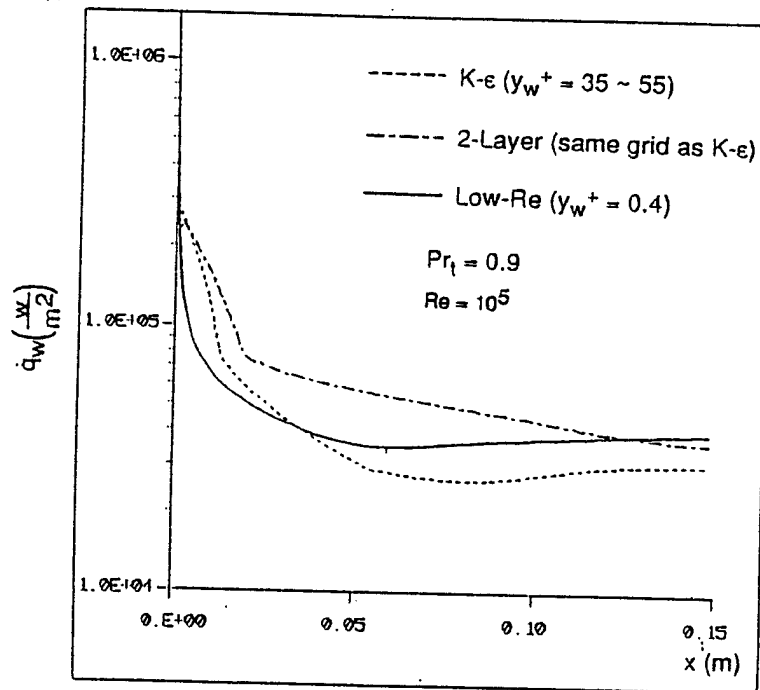


Figure 6-17b. Comparison of Heat Flux Predictions from the Three Turbulence Models for Upward Flow in the 2-D Channel with $q_w = 30\text{KW/M}^2$

7. COMPUTATIONAL RESULTS FOR FLOW AND HEAT TRANSFER

This section describes the flow and heat transfer results obtained for supercritical fluid flow of CO_2 over a range of Reynolds number going from the laminar to the turbulent regime. The effect of buoyancy on laminar and turbulent heat transfer is investigated in detail. Detailed comparisons with experimental data are also presented. A large amount of experimental data are available (for flow of supercritical CO_2) and therefore this study is of significant value in terms of model validation.

7.1 Boundary Conditions

The geometry (and computational grid) that was considered for the two-dimensional channel flow cases is shown in Figure 7-1. Only the lower half of the channel is considered in the simulations with appropriate symmetry boundary conditions. The half channel height (H) is 10 mm and the channel length (L) is 150 mm. The channel pressure was set equal to 7.58 MPa which is above the critical pressure ($P_c = 7.38$ MPa) for CO_2 . The inlet temperature of CO_2 was set to 288°K which is lower than the critical temperature ($T_c = 304.1^\circ\text{K}$) for CO_2 . The wall of the channel is heated ($T_w = 320^\circ\text{K}$) so that the fluid temperature increases beyond the critical point at some intermediate point along the channel. These conditions are representative of the conditions in fuel lines where the fuel (at supercritical pressure and subcritical temperature) enters the heat exchanger and gets heated beyond the critical point.

It is observed from Figure 7-1 that the computational grid is clustered near the heated wall in order to resolve the steep variations in transport properties. Grid independence was checked by progressively refining the grid until the solutions became independent of the grid. Simulations are done for downward flows (in the direction of gravity) and upward flows (against the direction of gravity) and the heat transfer rates are compared with the no-gravity case. This was done primarily to assess the effect of buoyancy in influencing heat transfer process.

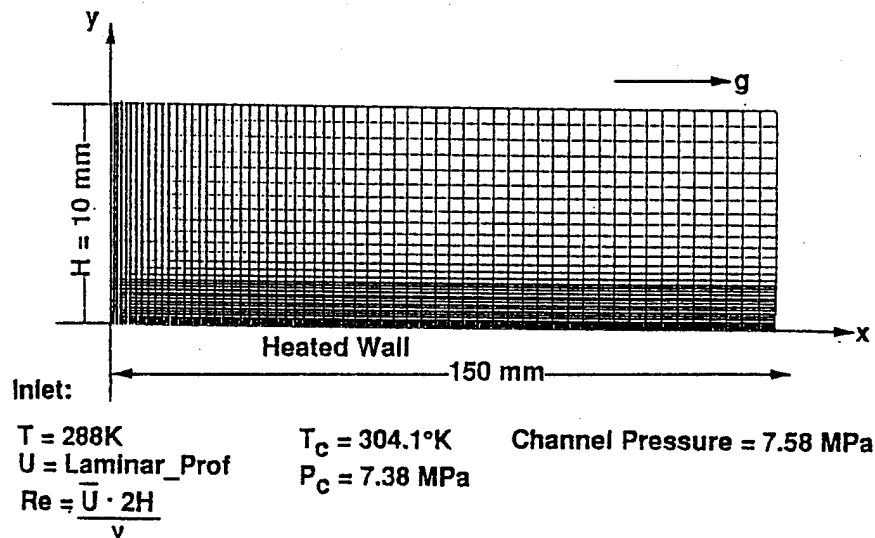


Figure 7-1. Computational Geometry and Grid for the 2-D Channel Flow Problem

7.2 Results for Laminar Heat Transfer

The inlet velocity of CO_2 was taken to be 0.05m/sec . This corresponds to a Reynolds number of 10,000 based on inlet conditions. A laminar flow model was used to calculate the fluid flow and heat transfer in the channel. Upward and downward flows and the corresponding no-gravity cases were simulated. Figure 7-2 shows the transverse profiles of density, velocity and temperature at an axial location corresponding to $x/2H = 4.4$. The dashed lines represent the no-gravity case. The heated wall causes the local fluid temperature at the wall to increase beyond the critical point although the bulk fluid is still at subcritical temperatures. This gives rise to a density gradient near the wall. The density decreases by almost a factor of four in the density boundary layer. For the no-gravity case, the density and temperature boundary layer thicknesses are of the order of 0.25 in non-dimensional distance. Interestingly, the upward flow shows much higher gradients for the same quantities. The boundary layer thicknesses (for the upward flow) for the density and temperature are of the order of 0.05 in non-dimensional distance.

This feature can be better understood by looking at the velocity profiles. The no gravity cases exhibits the typical boundary layer profile with the velocity increasing monotonically from a zero value at the wall to the bulk value outside the boundary

layer. However, for the upward flow, the velocity profile shows a peak near the wall. Also the magnitude of the peak is quite large compared to the bulk value. This is due to the fact that the large decrease in density near the wall gives rise to an upward acceleration of the fluid under the action of gravity. The local acceleration of the low density fluid leads to thinner boundary layers for both temperature and density. The direct result of a thinner boundary layer for the temperature is an increased heat transfer coefficient. This is reflected in Figure 7-4 which shows the local heat flux at the wall along the entire channel length. It is observed that the heat flux values calculated for the upward flow are almost an order of magnitude higher than those computed for the no-gravity case.

Figure 7-3 shows the transverse profiles of density, temperature and velocity for the downward flow at the same axial location. The results for the no-gravity case are shown by dashed lines. Again, it is observed that the effect of buoyancy is to accelerate the low density fluid near the wall in the upward direction (i.e., against the direction of the bulk flow). The density and temperature boundary layer thicknesses for the downward flow case are thinner compared to the no-gravity case. This translates into higher heat transfer rates as shown in Figure 7-4. The heat transfer rates at the inlet (for the downward flow) are lower than those obtained for the upward flow. The two curves cross each other half-way along the length of the channel. This can be explained by the fact that the upward acceleration due to buoyancy counteracts the mean downward flow at the inlet leading to local flow stagnation and decreased heat transfer rates. However, at locations far downstream of the inlet, the upward flow due to buoyancy overwhelms the effect of the bulk flow leading to increased heat transfer rates.

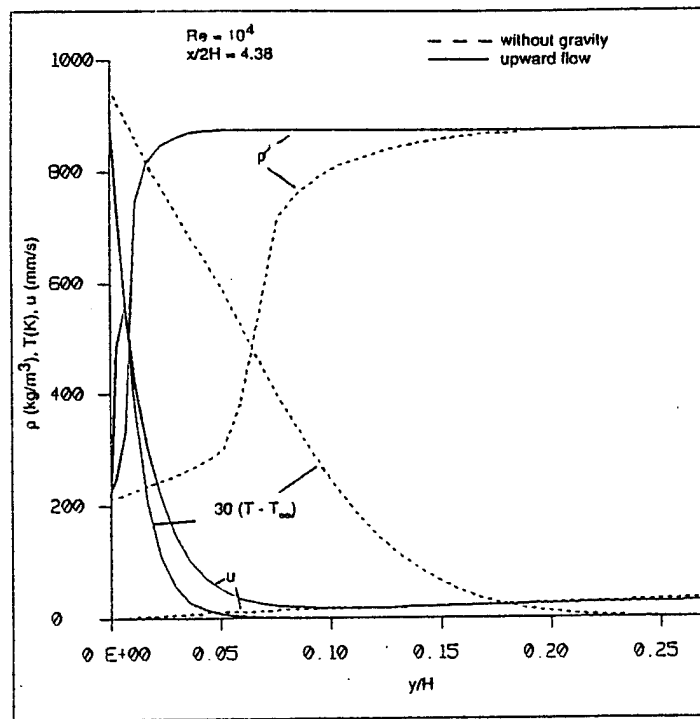


Figure 7-2. Predicted Profiles of Density, Velocity and Temperature in Channel for the Upward Flow ($Re = 1,000$)

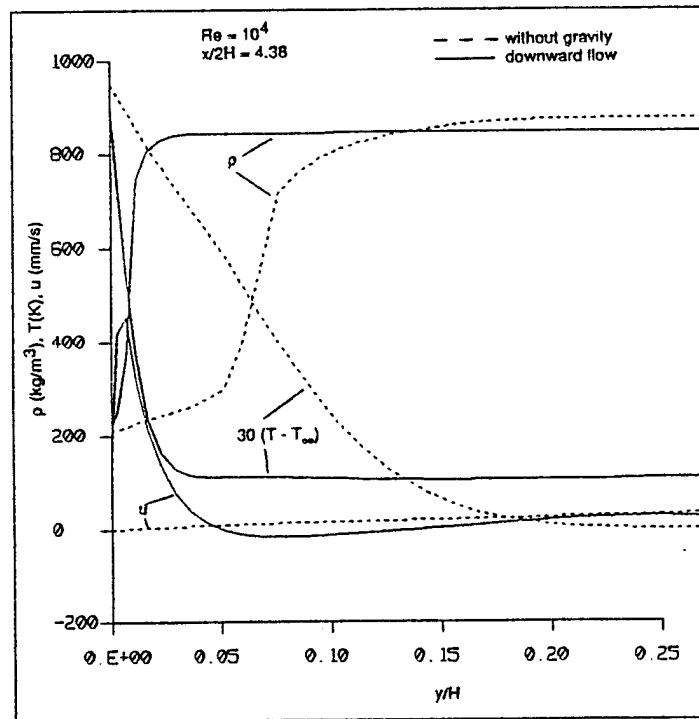


Figure 7-3. Predicted Profiles of Density, Velocity and Temperature in the Channel for the Downward Flow ($Re = 10,000$)

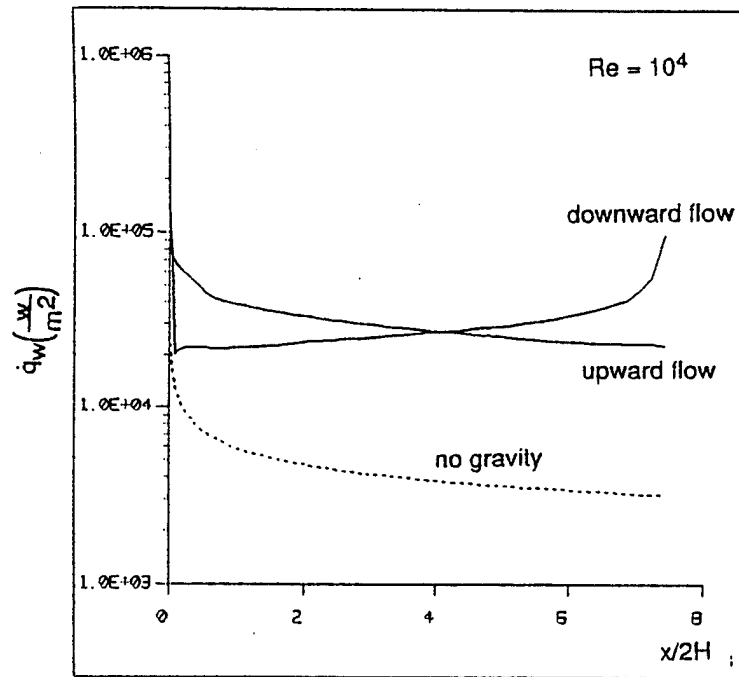


Figure 7-4. Local Heat Flux Along the Channel Wall for the Upward Flow, the Downward Flow and the No-Gravity Case ($Re = 10,000$)

7.3 Discussion of Laminar Heat Transfer Results

It is observed that the effect of buoyancy is to increase local heat transfer rates for both upward and downward flows. This is mainly due to the local upward acceleration of the low density fluid near the heated wall under the action of gravity. Since the heat transfer rates in this flow regime are largely influenced by the local density gradients, it is a fair assumption that ideal gas models would not be able to predict heat transfer in such flows mainly due to the inability of ideal gas models in predicting the large density decrease near the heated wall.

Figure 7-5 shows the comparison between predicted heat transfer rates and measured values for laminar free convection of supercritical CO_2 adjacent to a heated wall. The surrounding pressure is 8.11 MPa and the ambient temperature is 310.16°K. Heat transfer measurements [32] were made while the flow was still in the laminar regime. The heat flux is plotted as a function of wall temperature in Figure 7-5. It is observed that the model predictions are in good agreement with the data.

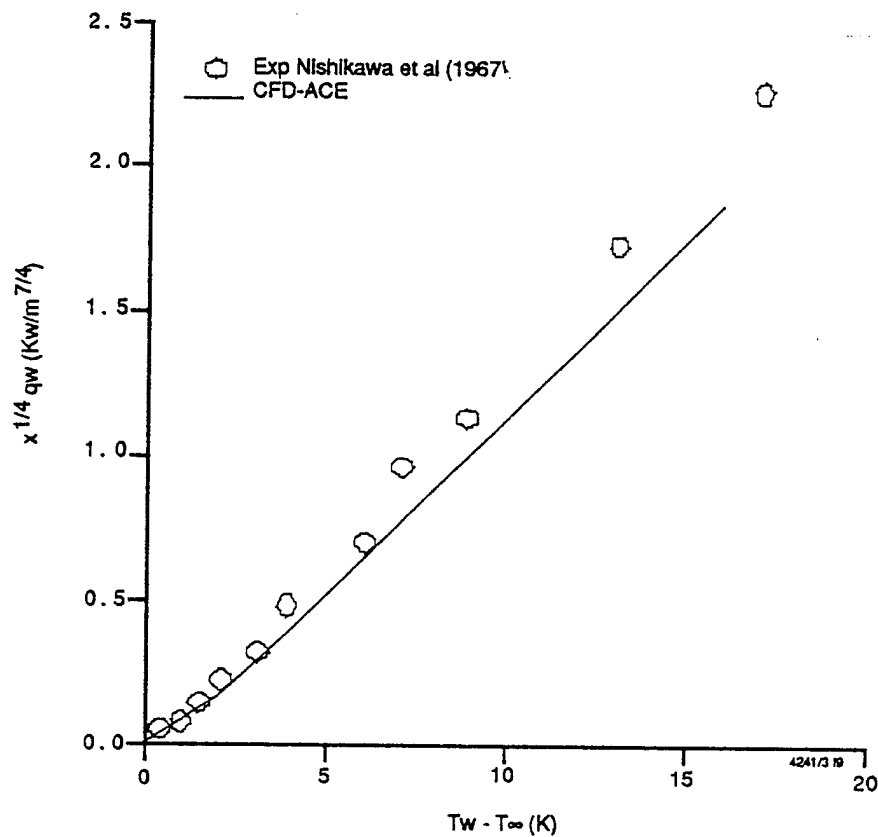


Figure 7-5. Comparison of Measured and Predicted Heat Flux Values for Free Convection of Supercritical CO_2

7.4 Results for Turbulent Heat Transfer

The turbulent flow simulations were done using the low Reynolds number $k-\epsilon$ model [20]. The case of laminar flow in the two-dimensional channel was repeated using the turbulent flow model. The heat transfer rates predicted by the laminar model and the turbulent model are compared for the upward flow, the downward flow and the no-gravity case (see Figure 7-6). It is observed that both models essentially predict the same heat transfer values thus indicating that the effect of turbulence was minimal for this problem.

The inlet velocity was increased by a factor of ten, i.e., the effective Reynolds number was increased to 100,000. Figure 7-7 shows the turbulent heat transfer rates predicted along the channel wall (for a wall temperature of 320°K) for the upward flow, the downward flow and the no-gravity case. In contrast to the laminar case, it is observed that the heat transfer rates for the upward flow are lower than those for

the no-gravity case which are in turn lower than the heat transfer rates predicted for the downward flow. These findings are contrary to the results obtained for $Re = 10,000$ where the predicted heat flux values for the upward flow and the downward flow are higher than those for the no-gravity case. This rather curious behavior can be explained based on the following arguments.

Figures 7-8a and 7-8b show the velocity profiles at different locations in the channel for the upward and downward flow, respectively. The dashed lines indicate the results for the no-gravity case. For the upward flow, it is observed that the upward acceleration of the low density fluid near the wall due to gravity gives rise to velocity peaks or maxima near the wall. The net effect of the velocity maxima is to increase the velocity gradient at the wall and to decrease the velocity gradient (compared to the no-gravity case) a little distance away from the wall. In turbulent boundary layers, a shear layer exists in the vicinity of the wall that is essentially responsible for the turbulent transport of mass momentum and energy from the bulk flow to the boundary layer. But the occurrence of velocity maxima reduces the velocity gradient in the region of the shear layer thus reducing the turbulence kinetic energy and hence the turbulent transport. For the downward flow (Figure, 7-8b) it is observed that the velocity gradients in the shear layer region are actually increased (compared to the no-gravity case) due to the acceleration of the low density fluid and thus leading to increased turbulent transport.

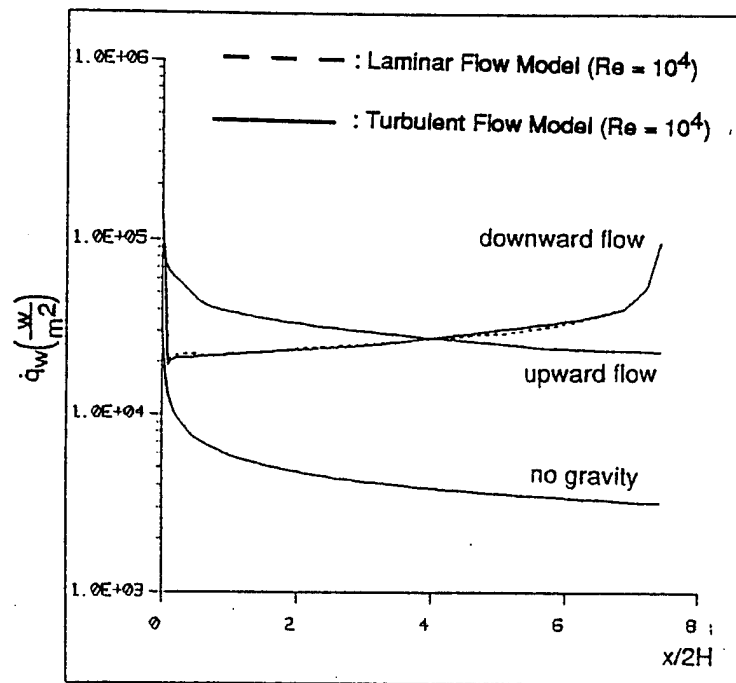


Figure 7-6. Comparison of Predictions of Heat Flux from Laminar and Turbulent Flow Models for $Re = 10,000$

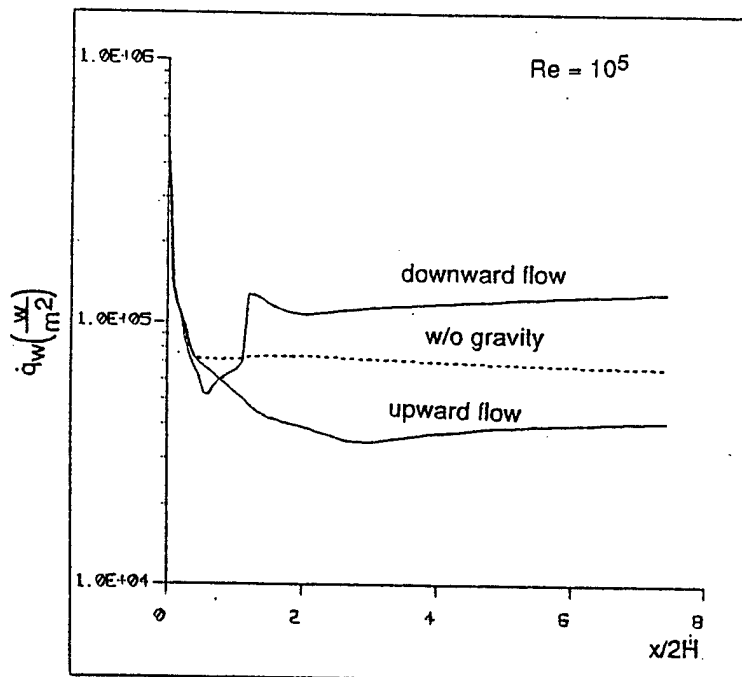


Figure 7-7. Turbulent Heat Flux Prediction Along Channel Wall at $Re = 100,000$

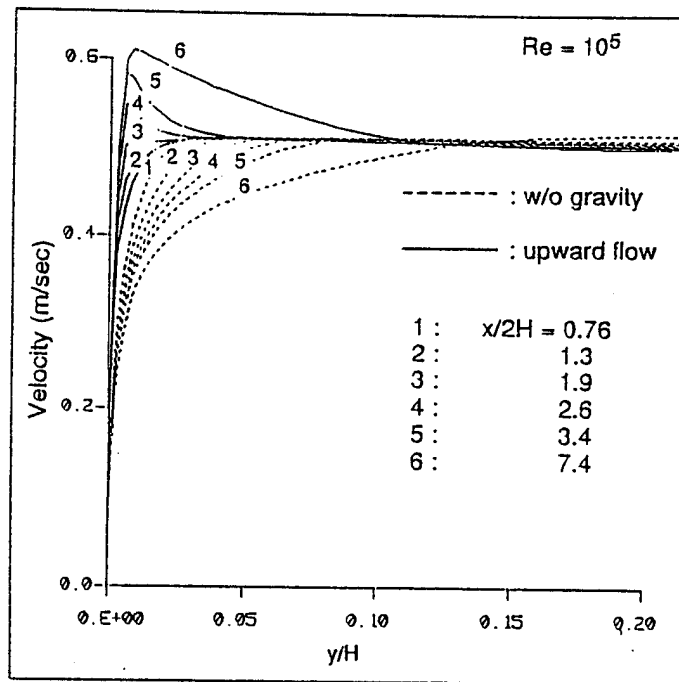


Figure 7-8a. Comparison of Mean Velocity Profiles for the Upward Flow and the No-Gravity Cases for $Re = 100,000$

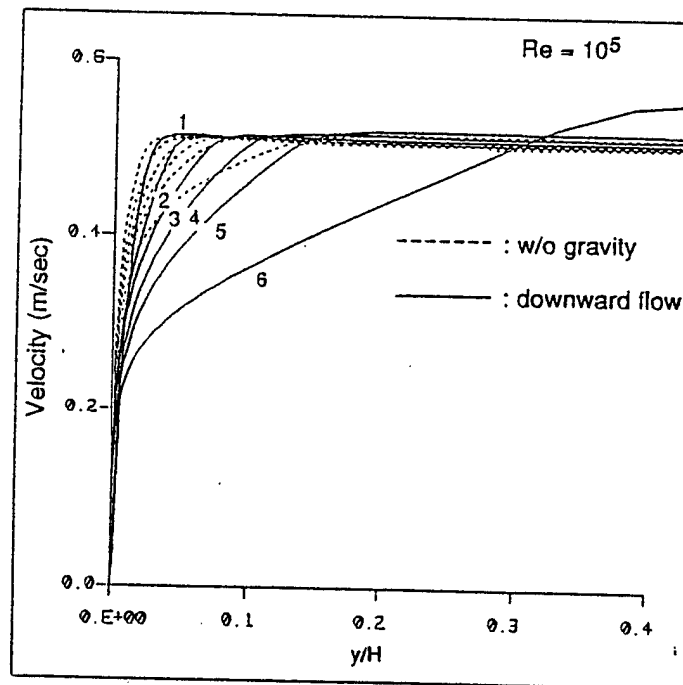


Figure 7-8b. Comparison of Mean Velocity Profiles for the Downward Flow and No-Gravity Cases for $Re = 100,000$

Figures 7-9a and 7-9b show the turbulent viscosity profiles (calculated by the low Reynolds number k- ϵ model) for the upward and the downward flows respectively. For the upward flow, it is observed that the calculated turbulent viscosity near the wall (in the shear layer region) is lower than those predicted for the no-gravity case. Correspondingly, the turbulent viscosity for the downward flow is higher than those obtained for the no-gravity case. Figures 7-10a and 7-10b show the temperature profiles in the channel for the upward flow and the downward flow respectively. For the upward flow, it is observed that the temperature gradients at the wall are lower than those predicted for the no-gravity case. This is a direct result of reduced turbulent transport (due to velocity maxima) and leads to reduced heat transfer rates or increased heat transfer resistance at the wall. Correspondingly, the temperature gradients for the downward flow are larger than the gradients for the no-gravity case thus leading to increased heat transfer at the wall.

7.5 Discussion of Turbulent Heat Transfer Results

It is observed that the upward acceleration of low density fluid near the heated wall (due to gravity) affects the local velocity profile thus influencing the turbulent transport near the wall. The trends in heat transfer are also changed depending on the direction of the mean flow with respect to gravity. Similar phenomena have been observed in experiments [4] involving the turbulent flow of CO₂ in pipes.

Figures 7-11a and 7-11b show the results for heat transfer calculated in a pipe (1.9 cm in diameter) with a specified heat flux condition. The Reynolds number for these cases are approximately equal to 100,000. Figure 7-11a shows the computed wall temperatures predicted for a heat flux condition of 3.09 W/cm². The symbols represent experimental measurements [4] with the downward triangles representing downflow data and the upward triangles representing the upflow data. For a heat flux value of 3.09 W/cm², both the data and the model indicate that the wall temperatures for the upward flow are slightly higher than those for the downward flow. Again, this is a direct consequence of increased heat transfer resistance for the upward flow. The model results appear to be in reasonable agreement with the data.

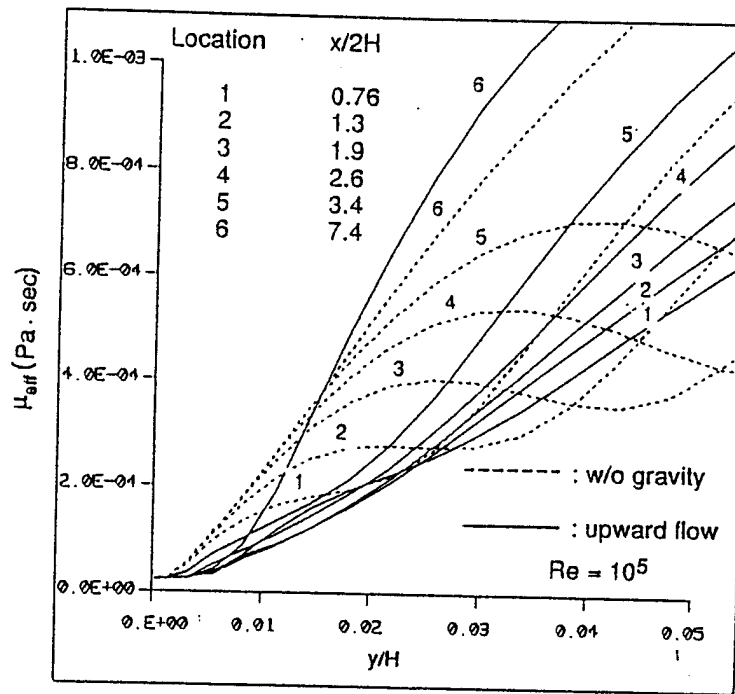


Figure 7-9a. Comparison of Turbulent Viscosity Profiles for the Upward Flow and No-Gravity Cases for $Re = 100,000$

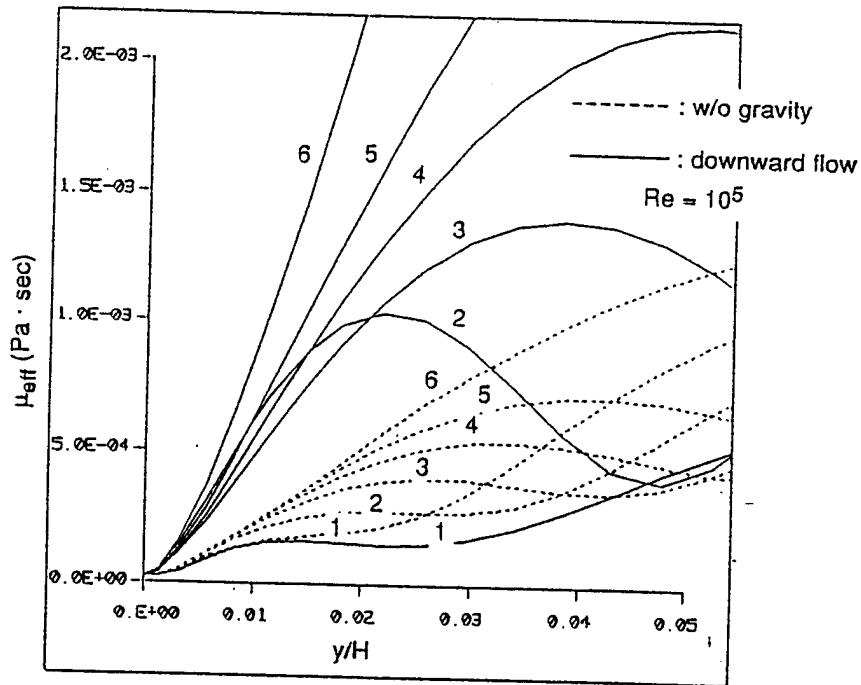


Figure 7-9b. Comparison of Turbulent Viscosity Profiles for the Downward Flow and No-Gravity Cases for $Re = 100,000$

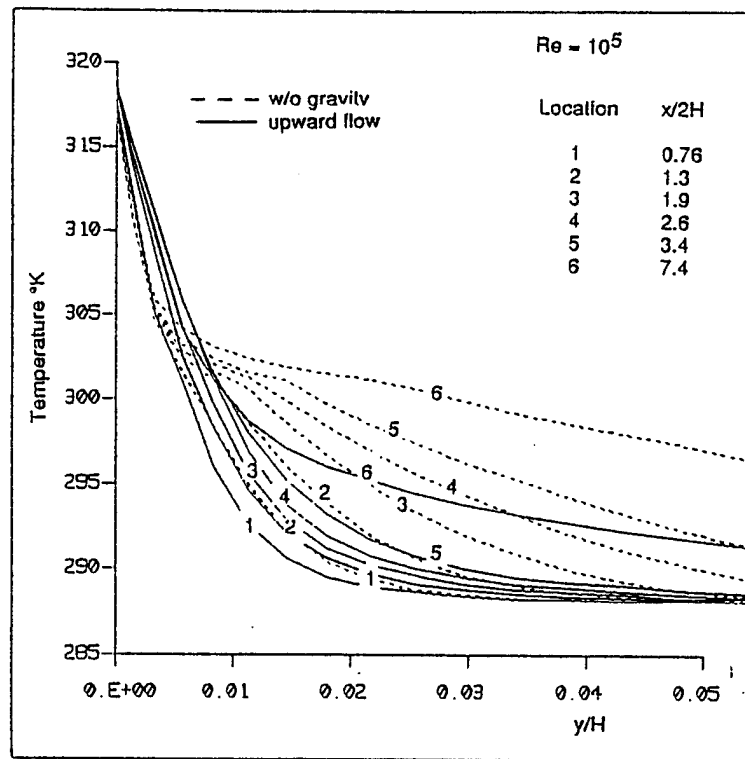


Figure 7-10a. Comparison of Temperature Profiles for the Upward Flow and No-Gravity Cases for $Re = 100,000$

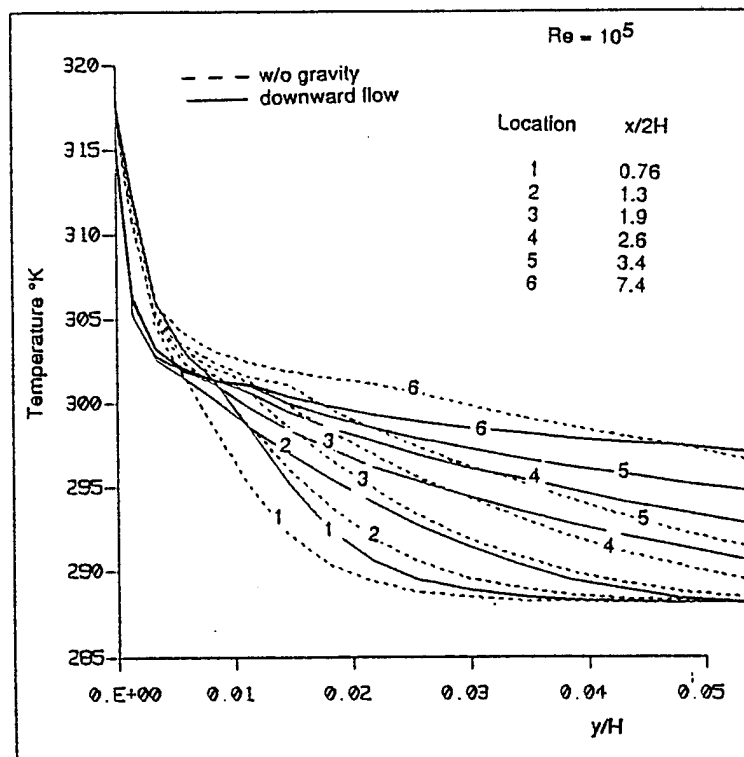


Figure 7-10b. Comparison of Temperature Profile for the Downward Flow and No-Gravity Cases for $Re = 100,000$

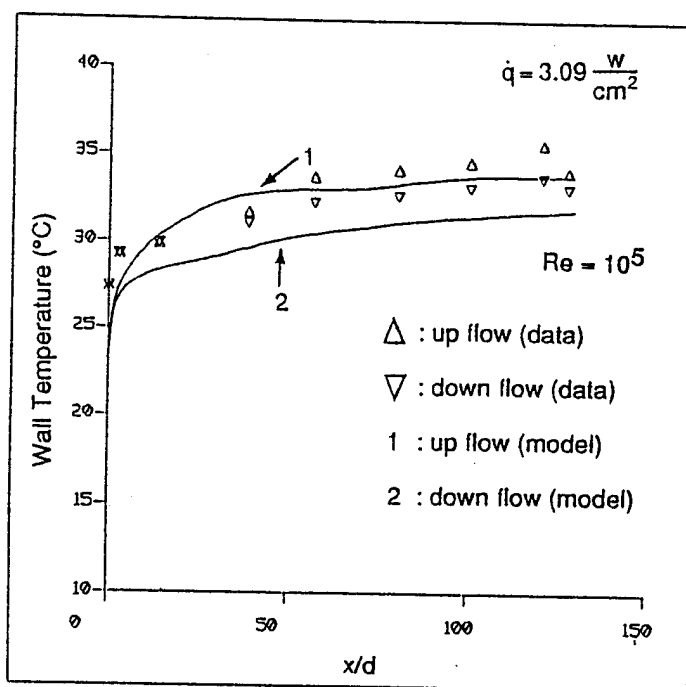


Figure 7-11a. Measured and Predicted Wall Temperatures in Pipe Flow of CO_2

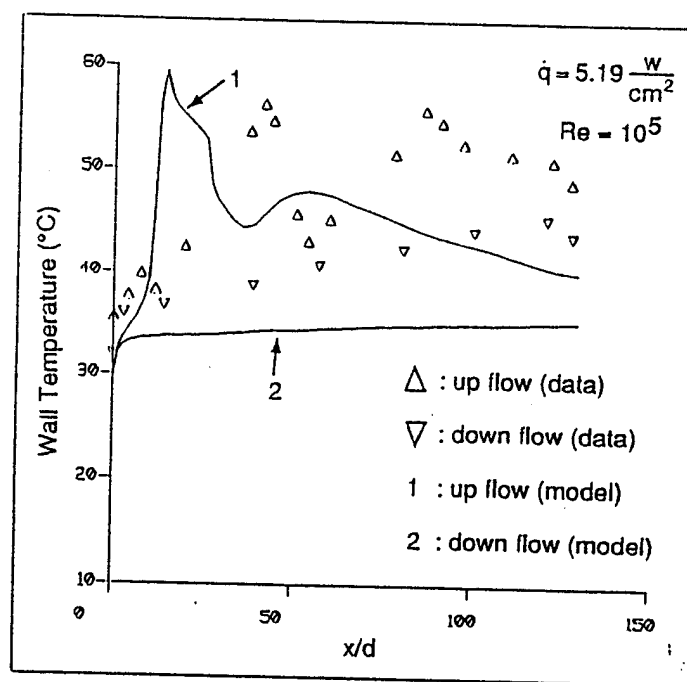


Figure 7-11b. Measured and Predicted Wall Temperatures in Pipe Flow of CO_2

Figure 7-11b shows the results for a higher heat flux value of 5.19 W/cm². The predicted wall temperatures for the upward flow show a dramatic increase compared to the downward flow. This is reflected by both the model and the data. Although the trends are correctly predicted by the model, there are some differences in the actual magnitude of wall temperatures between the model and the data. The reason for this discrepancy is not clear. However, the experimental data itself has significant error bars (or standard error) for the high heat flux conditions [4] reflecting the difficulty of making accurate measurements in this regime. But there is no mistaking the trends portrayed by both the data and the model predictions.

For the low heat flux case, the heat addition is not sufficient to create a significantly thick low density layer near the wall (by increasing the fluid temperature beyond its critical point) and hence only small differences are observed between the upflow and downflow results. However, in the high heat flux case, the buoyancy driven flow is of sufficient magnitude to drastically increase the heat transfer resistance for the upflow case thus resulting in increased wall temperatures and local hot spots in the tube.

7.6 Non-Dimensional Analysis of the Problem

One of the main observations from the above simulations is that buoyancy plays an important role in influencing heat transfer (in supercritical flows) even at Reynolds numbers as high as 100,000. This is of particular concern for aircraft heat exchangers which operate in this range of Reynolds numbers. In order to better understand the influence of buoyancy, the following non-dimensional analysis is performed.

The Grashof number is a non-dimensional number that is a ratio of the effect of buoyancy forces over viscous forces in a flow. The Grashof number is defined as follows:

$$Gr = \frac{\rho g \Delta p L^3}{\mu^2}$$

where L is a typical length scale for the problem. For the operating conditions

described for the two-dimensional channel flow and the pipe flow, a representative Grashof number can be calculated as follows based on inlet conditions:

$$\begin{aligned}\rho &\approx 860 \text{ kg/m}^3 (\text{at } 288^\circ\text{K}) \\ g &= 9.81 \text{ m/sec}^2 \\ \mu &\approx 1 \times 10^{-4} \text{ N-sec/m}^2 \\ \Delta\rho &= \rho(288^\circ\text{K}) - \rho_w(320^\circ\text{K}) \\ &\approx 860 \text{ kg/m}^3 - 200 \text{ kg/m}^3 = 660 \text{ kg/m}^3 \\ L &\approx 0.15 \text{ m}\end{aligned}$$

The calculated Grashof number turns out to be:

$$G_r \approx 10^{12}$$

The non-dimensional ratio that describes the effectiveness of natural convection over forced convection is:

$$\frac{G_r}{(\text{Re})^2}$$

For a Reynolds number value of 100,000, the ratio is still of the order of 100 indicating that buoyancy will play an important role. This has been confirmed by detailed simulations of the channel flow and pipe flow cases.

However, for a Reynolds number of 1,000,000, the above ratio will be of the order of unity and the effect of buoyancy should be considerably smaller. In order to verify this, additional simulations were performed (for wall temperatures of 320°K and 600°K) for the two-dimensional channel with increased inlet velocity corresponding to a Reynolds number of 1,000,000. Figure 7-12 shows the calculated heat transfer rates for the two wall temperature cases. It is observed that the heat transfer rates predicted for the upward flow are exactly the same as those predicted for the no-gravity case, i.e., gravitational effects are negligible.

For most cases, however, the evaluation of a representative Grashof number becomes extremely difficult since the density, the density gradient and the viscosity become complex functions of the reduced pressure and temperature, the g value and flow characteristics. Especially for problems with specified heat flux conditions (which is representative of many practical problems as opposed to the constant wall temperature condition), a non-dimensional analysis of the kind shown above is no trivial task. The local density gradient influences the flow field (through buoyancy effects) which in turn influences heat transfer (by affecting boundary layers and heat transfer coefficients) which in turn influences the local temperature distribution which in turn affects the local density distribution. This is illustrated schematically in Figure 7-13. The link between temperature and density (as illustrated in Figure 7-13) is crucial. For incompressible flows with low heat transfer rates, the link is very weak. For low speed flows of gases (in the range of pressures where the ideal gas assumption is valid) the density is proportional to the reciprocal of the temperature. For supercritical flows, the density is a highly non-linear function of temperature in the vicinity of the critical point.

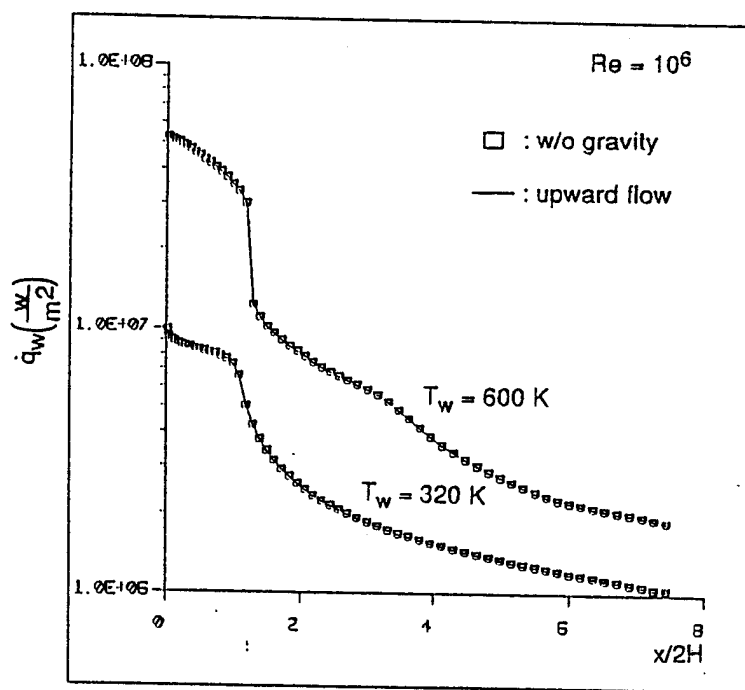


Figure 7-12. Predicted Heat Flux Values Along the Channel Wall for $Re = 1,000,000$

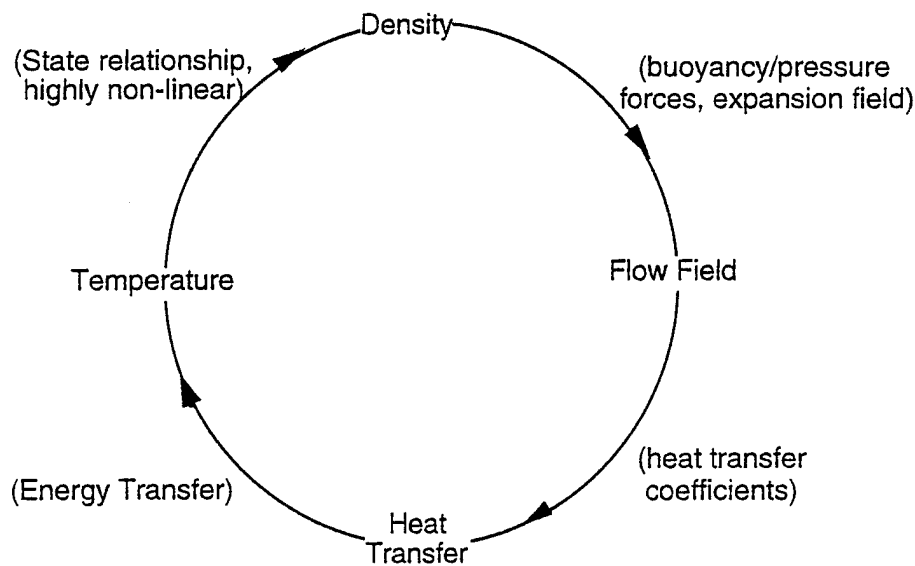


Figure 7-13. Illustration of the Coupling between Various Physical Phenomena

This highly non-linear coupling between temperature and density (in the supercritical regime) makes the a priori determination of buoyancy effects extremely difficult. If the heat flux is sufficient to increase the fluid temperature beyond the critical value, the corresponding Grashof numbers will be large. On the other hand, if the heat flux is not strong enough to increase the fluid temperature beyond its critical value, local Grashof numbers will be relatively small. Therefore depending on the heat flux value, Grashof numbers can differ by orders of magnitude. For example, if the wall temperature were to be reduced from 320°K to 300°K, the calculated Grashof number is of the order of 10^{11} , i.e., a decrease of 20°K (~ 6%) in temperature has reduced the Gr value by one order of magnitude. These difficulties emphasize the need for advanced models that can simulate local effects in supercritical flows.

8. ASSESSMENT OF THE THERMAL STABILITY/DEPOSITION MODEL

This section presents the results from the application of the thermal stability models discussed in Section 2. The model predictions are compared with experimental data. These comparisons are used to further refine and recalibrate the models in order to improve their generality.

8.1 Jet-A Experiments

The Jet-A experiments are described in detail in the article by Katta et al. [23]. The near isothermal cases were considered for the simulation because it eliminates any uncertainties arising from inaccuracies in the calculation of the temperature. The operating conditions of the experiments are shown below:

Fuel Type: Jet-A

Flow Rate: 0.5 cc/min

Inlet Temperature: 288K

Tube Wall Temperature: 458K

Inlet Reynolds Number: $Re = \left(\frac{\rho u D}{\mu} \right) = 2$

Two tube sizes were considered for this study, the first one (the standard size) has an inner diameter of 2.159 mm and the other (the large size) has an inner diameter of 4.32 mm. The 9-step Katta model (described in Section 2) was applied to simulate these experiments. Figures 8-1a and 8-1b show the results for the deposition rate and the species distributions in the tubes. The dashed lines indicate the results predicted by the 9-step Katta model incorporated in CFD-ACE. Figure 8-2 shows the results from the article by Katta et al. [23]. It is observed that the CFD-ACE predictions are in good agreement with the results reported by Katta et al. However, it is observed that the model is not able to predict correctly the location of the deposition peaks compared with experimental data. This is a characteristic feature of the 9-step model that is prevalent in all of the cases analyzed during this study.

Although the results are in good agreement with the values reported in the

publication by Katta et al. [23], the current model shows small discrepancies from Katta's results. These deficiencies were attributed to the sensitivity of the Katta model to the value of τ_w used in the deposition model (Equation (48) in Section 2). In the original calculations reported in Katta et al., a standard k- ϵ model was used for the simulations and τ_w was based on the velocity of the first cell from the wall. However for large values of τ_w , (i.e. for turbulent flows) the model accuracy deteriorates. Katta et al. corrected for this effect by placing a limiter on τ_w . However, this procedure limits the generality of the model.

This is demonstrated by applying the model to a fuel flow experiment described in Section 3. The fuel flows through a heated tube with a wall temperature distribution as shown in Figure 8-3b. The model predictions are compared with measured data (see Figure 8-3a) on the deposition rate. It is observed that the model (see Figure 8-3a) underpredicts the total deposition rate as well as the distribution. In order to improve its generality, the surface reactions in the Katta model were recalibrated (see Section 2). The results of the recalibrated model are shown by the dark curves in Figures 8-1 and 8-3a. It is observed that the recalibrated model yields about the same results for the lowspeed isothermal tube cases (Figures 8-1a and 8-1b) as well as better agreement in deposition rate for the high speed fuel case shown in Figure 8-3a. However, the location of the deposition peaks are not predicted correctly. This is to be expected since the original 9-step model shows the same behavior. All of the Jet-A deposition studies reported in the subsequent sections of the report were done using the recalibrated Katta model.

8.2 JP-5 Experiments

The details of the JP-5 experiment conducted by Marteney and Spadaccini [33] are described below:

Fuel Type: JP-5
Flow Rate: 2.13 m/s
Inlet Temperature: 300°K
Wall Heat Flux: 395 kw/m²
Inlet Reynolds Number: ~3,000

The flow of JP-5 in a channel with a specified heat flux at the walls was considered. The low Reynolds number $k-\epsilon$ model was used to simulate the turbulence in the flow field. The 9-step model (for Jet-A) as well as the 4-step Krazinski model for JP-5 (see Section 2) were applied to simulate this case. The results are shown in Figures 8-4a and 8-4b. Figure 8-4a shows the wall and bulk temperature distributions in the tube. It is observed that the temperature distribution is predicted reasonably well by the low Re $k-\epsilon$ model. The standard $k-\epsilon$ model is unable to predict the initial bump in the wall temperature distribution due to the inherent assumption of a fully developed turbulent flow profile at the inlet.

The results for deposition rate indicate that the 4-step model for JP-5 shows good agreement with the data. The 9-step model (for Jet-A) underpredicts the deposition rate. The surface reactions in the 9-step model were further recalibrated (see Section 2) for JP-5 in order to improve the agreement. The recalibrated 9-step model for JP-5 shows better agreement with data. It is expected that further recalibration of gas phase reactions for JP-5 will result in better agreement with data.

8.3 Conclusions

It was determined that the original 9-step Katta model had to be recalibrated to improve its generality especially for higher fuel flow rates. The recalibrated model showed good agreement with the Katta model for low speed flows as well as for high flow rate fuel experiments. The 9-step model needed further recalibration for JP-5 in order to match the deposition rate data.

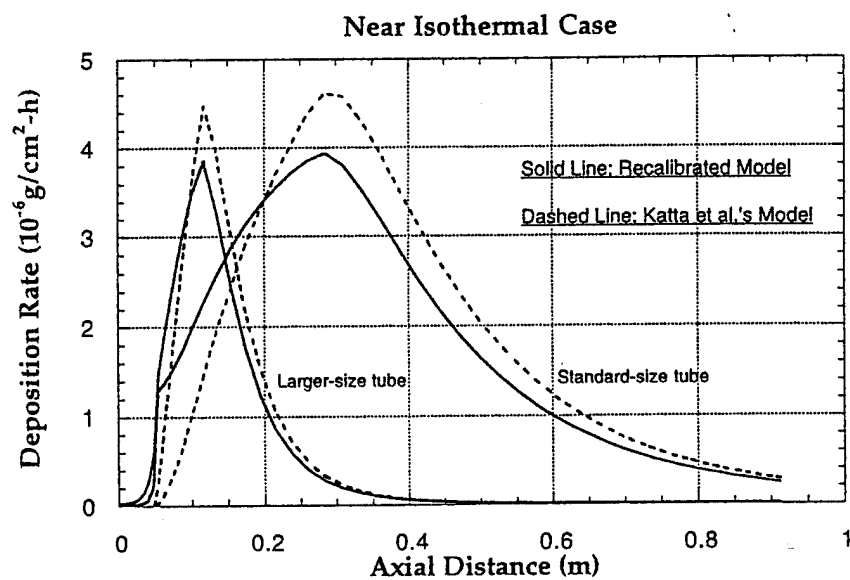


Figure 8-1a. Deposition Rate Distribution Along the Tube

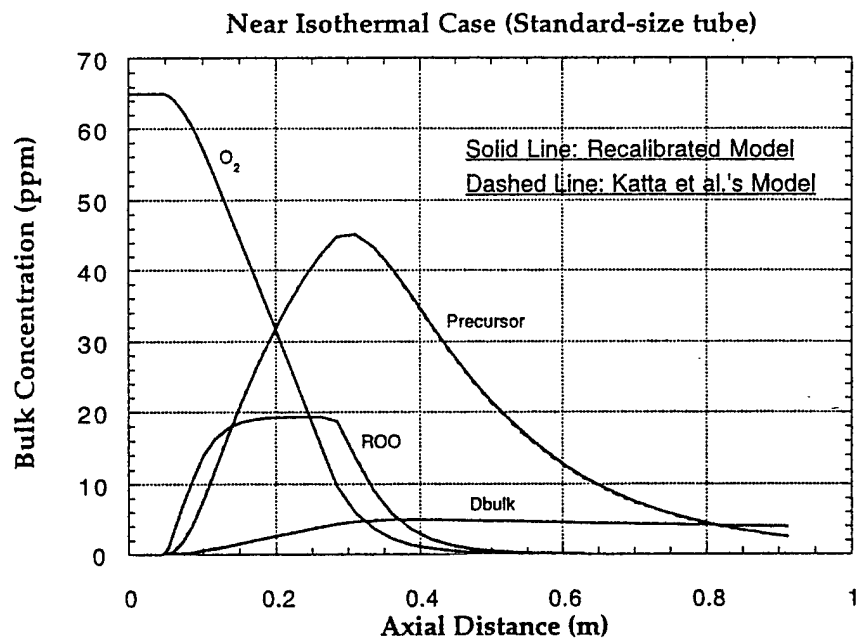


Figure 8-1b. Species Concentration Distribution Along the Tube

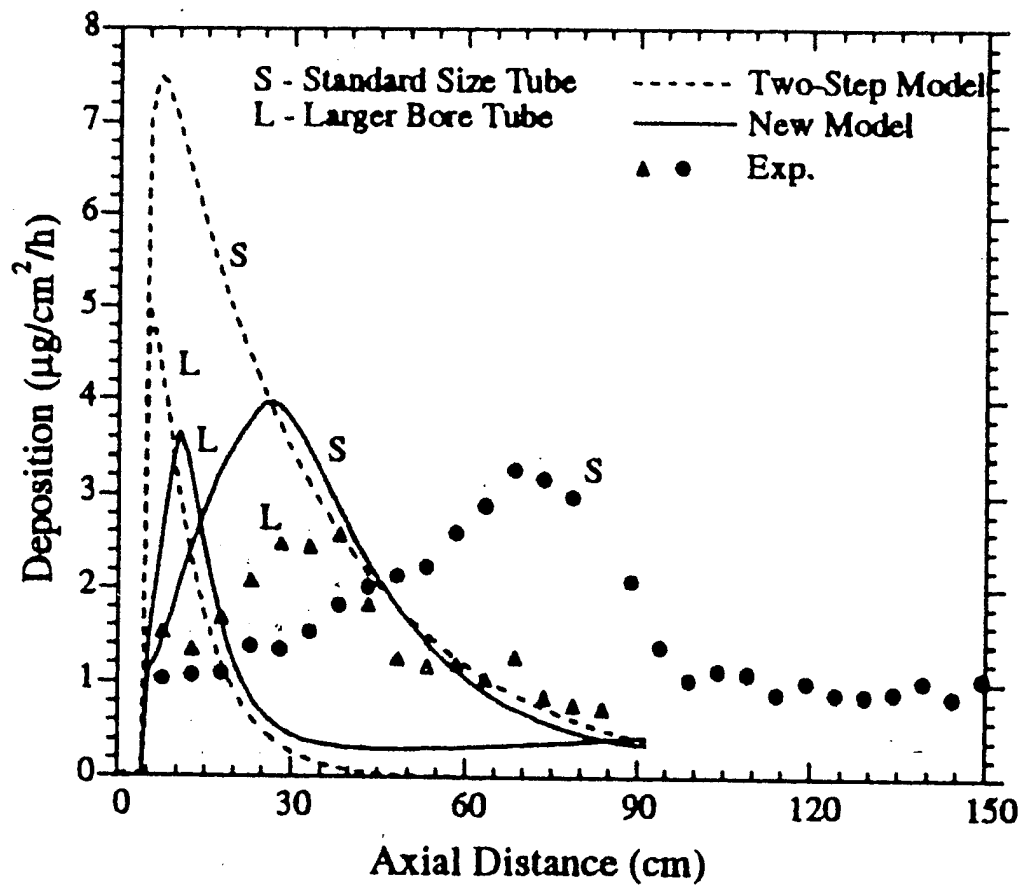


Figure 8-2. Predicted and Measured Deposition in Near-Isothermal (458K) Heated-Tube Experiment Using Two Different Bore Sizes [23]

Comparison of Deposition Rates for Jet-A Case 7/94-6

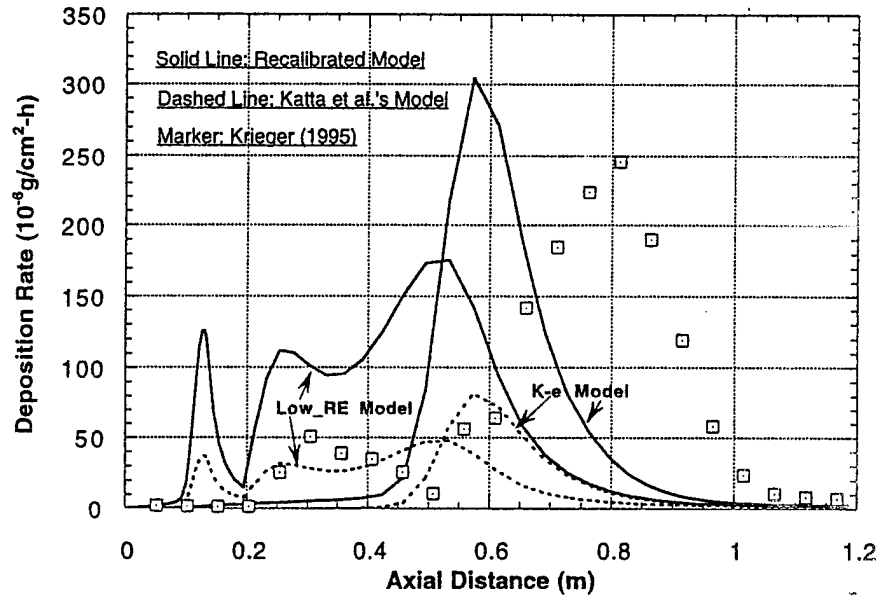


Figure 8-3a. Deposition Rate Distribution Along the Tube

Comparison of Wall Temperatures for Jet-A Case 7/94-6

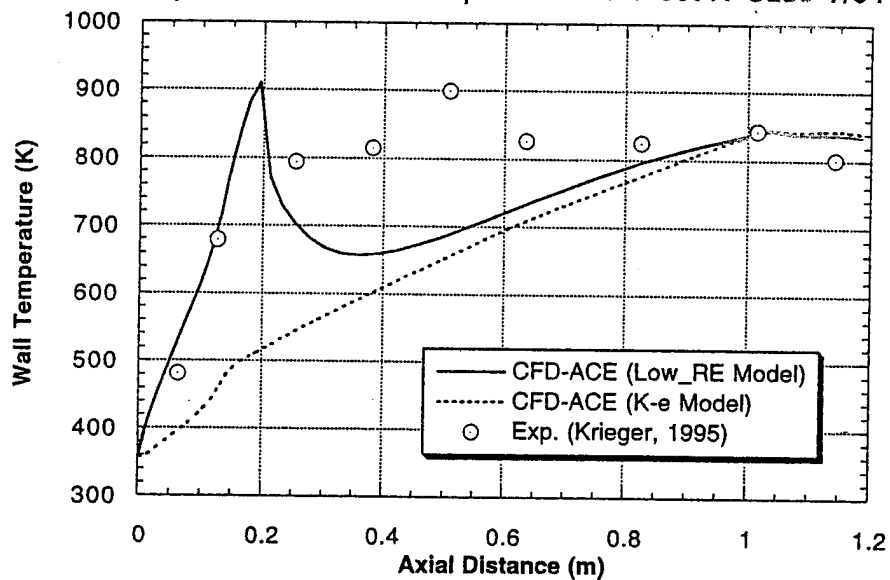


Figure 8-3b. Wall Temperature Distributions Along the Tube

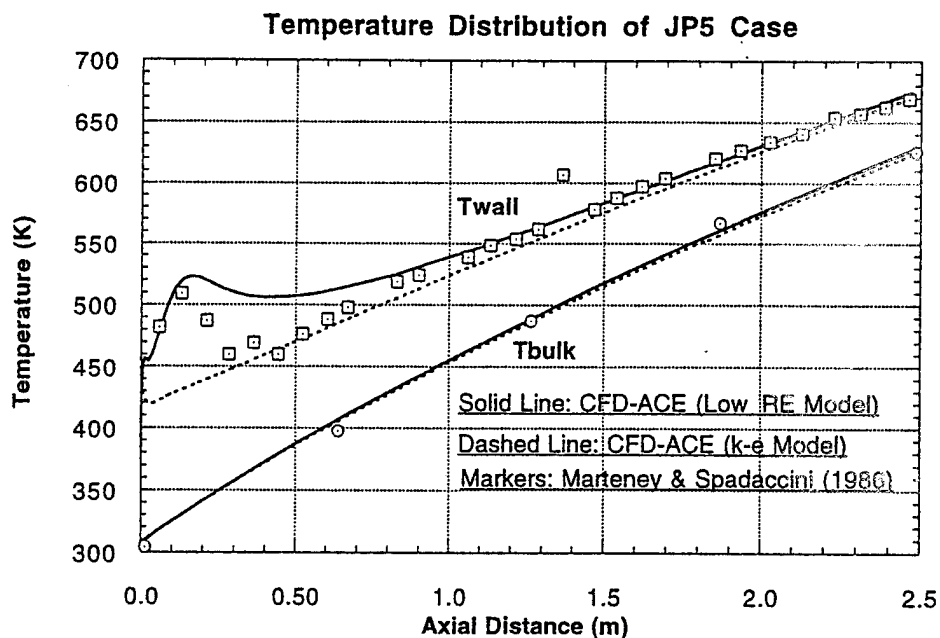


Figure 8-4a. Wall and Bulk Temperature Distributions Along the Tube

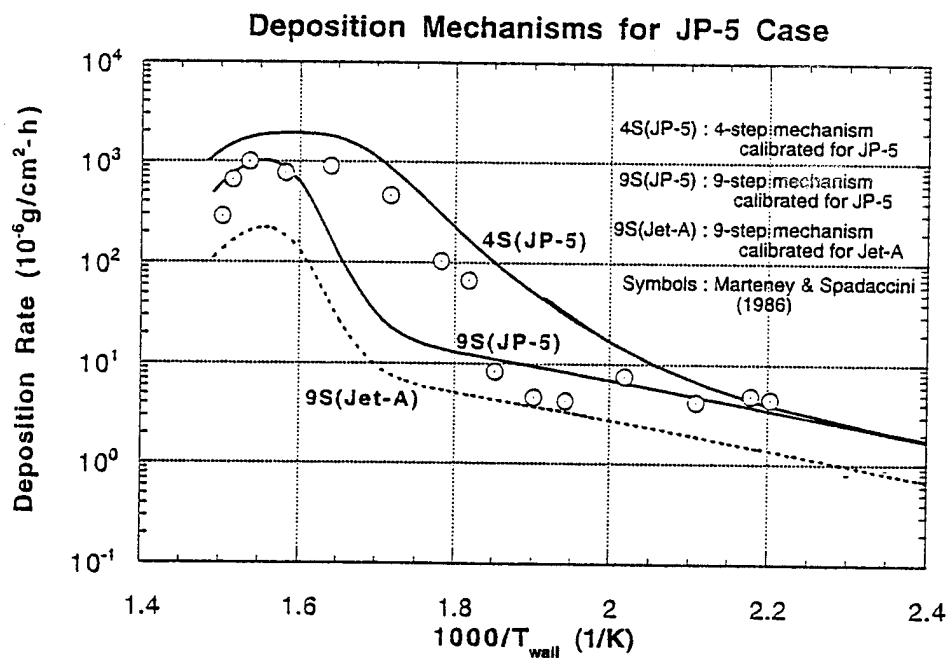


Figure 8-4b. Deposition Rate as a Function of Wall Temperature for Different Chemistry Models

9. BENCHMARK VALIDATION STUDY FOR THE DEPOSITION MODEL

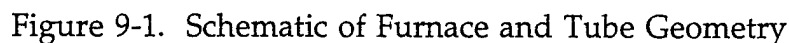
This section presents the comparisons between model predictions and data obtained at Wright Laboratory during the summer months (June to August) of 1994. Heat transfer and deposition experiments were conducted with air saturated Jet-A 2926 as the test fuel. The details of the experimental conditions and apparatus are described in Section 3. Three test cases (covering two operating pressures and two flow rates) were chosen (from all the sets of experiments) as benchmark cases for the validation study. These cases are as follows:

- a. Case 7/94-6 (Pressure = 650 psia, flow rate = 102 cc/min)
- b. Case 7/94-10 (Pressure = 400 psia, flow rate = 105 cc/min)
- c. Case 7/94-2 (Pressure = 650 psia, flow rate = 190 cc/min)

These were short duration experiments of 5 hours. Numerical simulations of the above experiments were performed and the model predictions of outer wall temperature and fuel deposition rate were compared with measured data.

9.1 Description of the Computational Model

The schematic of the computational domain is shown in Figure 9-1. The top surface is the hot furnace wall. The space between the furnace wall and the steel tube consists of stationary air. The heat is transferred from the furnace to the steel tube by means of radiation as well as conduction through the air. The steel tube is of finite thickness and offers conduction resistance to the flow of heat. The fuel flow in the steel tube is turbulent.



111

9.2 Model Predictions and Comparisons with Data

A grid independence study was performed to assess the sensitivity to grid refinement. Two grid sizes (75x64 and 120x90) were considered. The finer grid had a greater clustering of points in the vicinity of the temperature peak. The predicted wall temperatures and the deposition rates of the two grids are almost the same indicating that grid independence has been achieved (Figures 9-2a and 9-2b). The calculations described hereafter have been done on the 75x64 grid.

Case 7/94-6: The calculated wall temperatures and deposition rates for this case are shown in Figures 9-3a and 9-3b, respectively. The trend and order of magnitude of the predictions compare well with experimental data. However, the predicted temperature and deposition peak are sharper and occur further upstream (close to the furnace collar) than the measured data. There may be a number of reasons for this discrepancy such as (i) the difficulty in modeling the boundary conditions for energy accurately near the ends of the furnace, (ii) the current axisymmetric assumption precludes the consideration of 3-dimensional turbulence effects in the tube, and (iii) the validity of the deposition model at these temperatures may be in question since the calibration was done for much lower temperatures. However, there is good qualitative and to some extent, good quantitative agreement between the model predictions and data.

Case 7/94-10: This case is similar to the earlier one except that the operating pressure is reduced to 400 psia. The results are shown in Figures 9-4a and 9-4b. The wall temperature predictions are similar to results for the earlier case. The peak in deposition rate is still predicted further upstream than the measured data. However, the magnitudes of the temperatures and deposition rates agree well with the data.

Case 7/94-2: For this case, the flow rate is increased to 190 cc/min. The results are shown in Figures 9-5a and 9-5b. Again, the results are in qualitative agreement with data. The temperature and deposition rate peaks are predicted to be further upstream as compared with data.

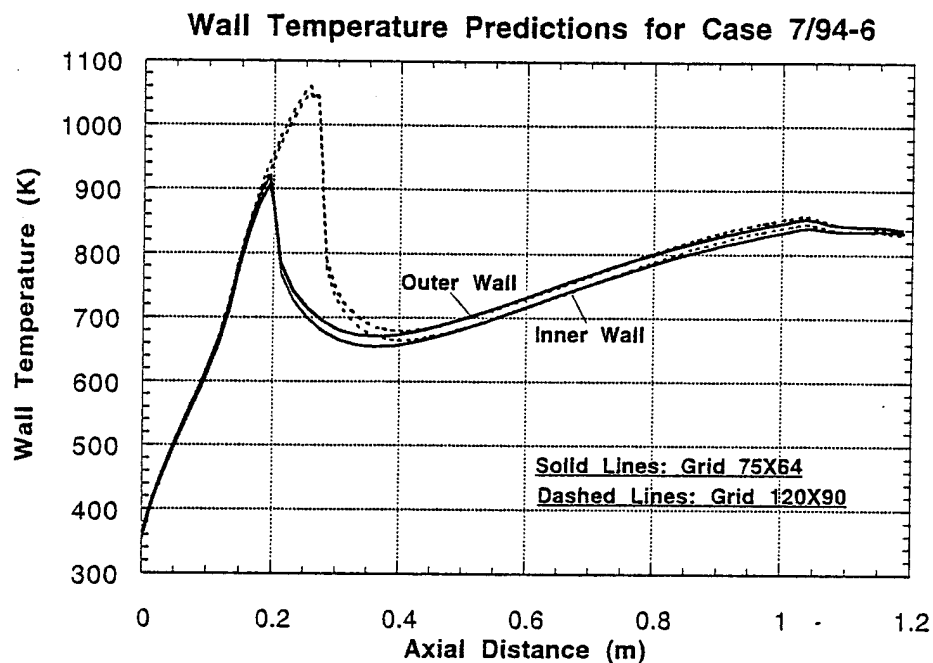


Figure 9-2a. Predicted Wall Temperature for the (75x64) Grid and the(120x40) Grid

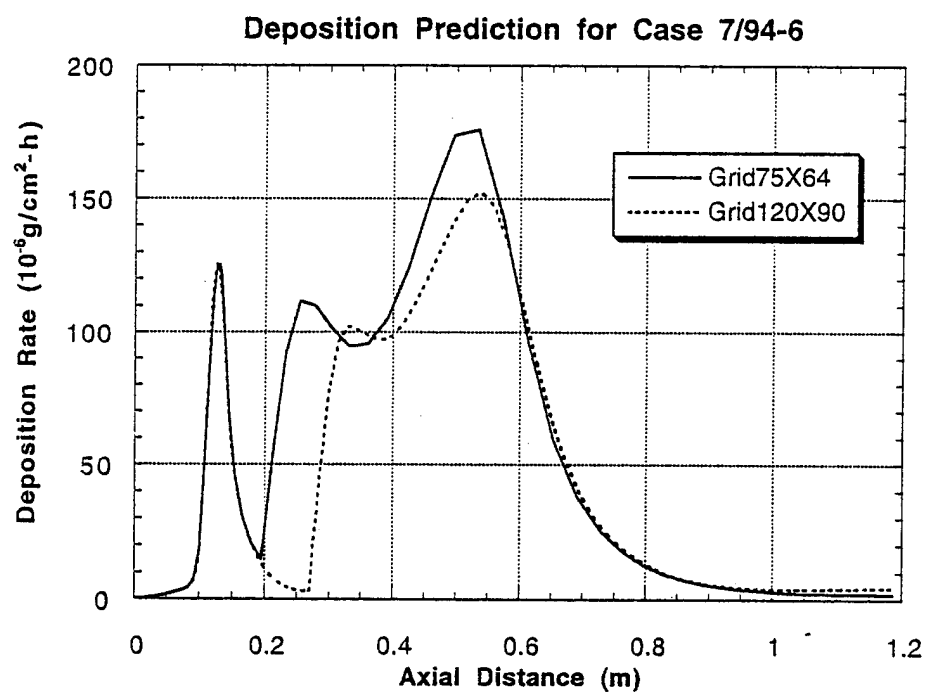


Figure 9-2b. Predicted Deposition Rates for the (75x64) Grid and the (120x90) Grid

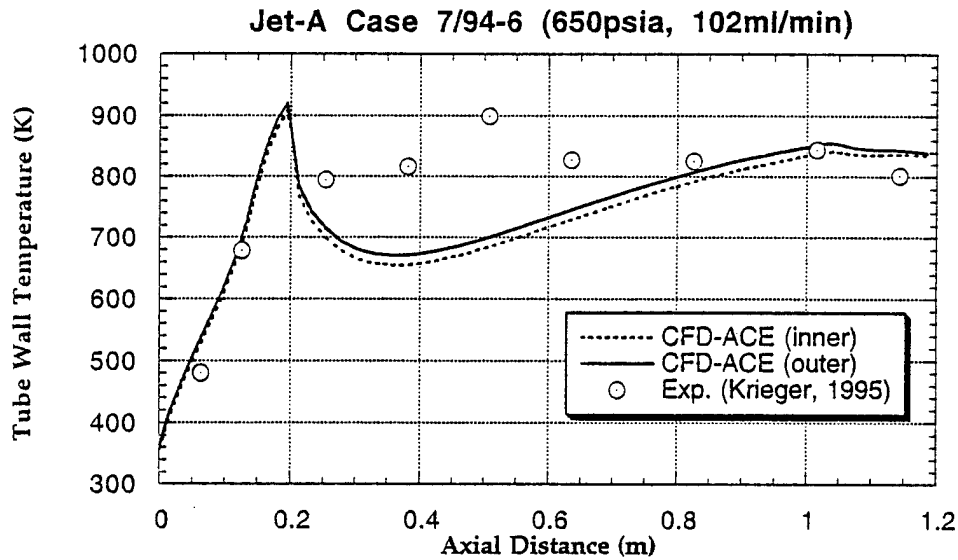


Figure 9-3a. Comparison of Predicted Wall Temperatures for Case 7/94-6 with Data

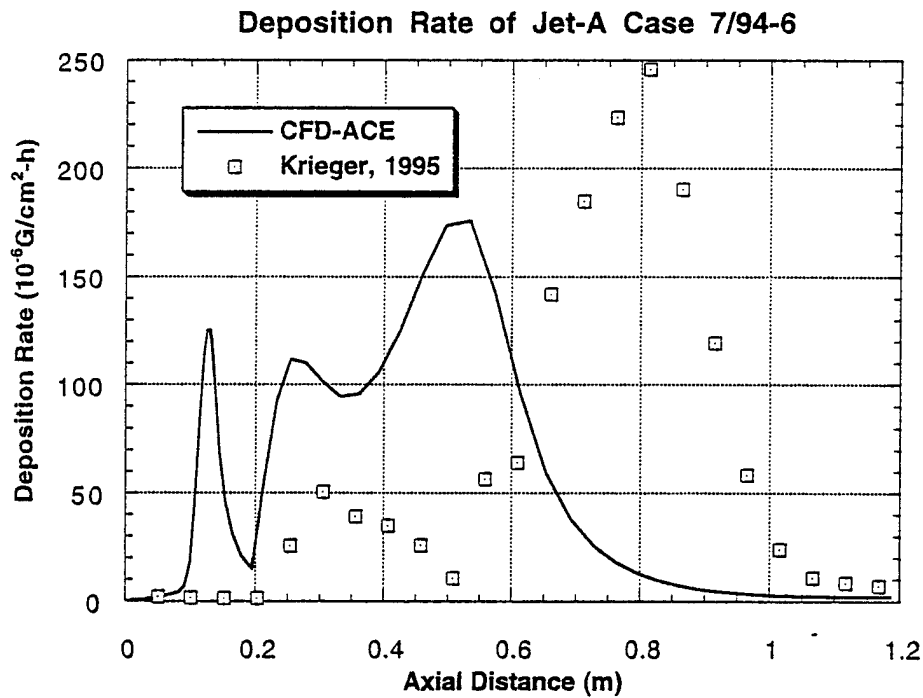


Figure 9-3b. Predicted Deposition Rates for Case 7/94-6 with Data

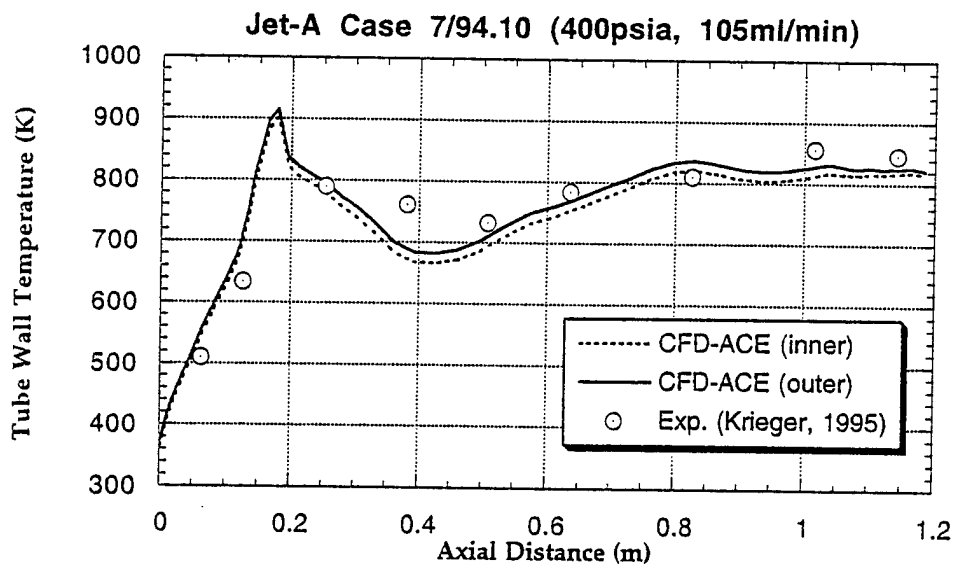


Figure 9-4a. Predicted Wall Temperatures for Case 7/94-10

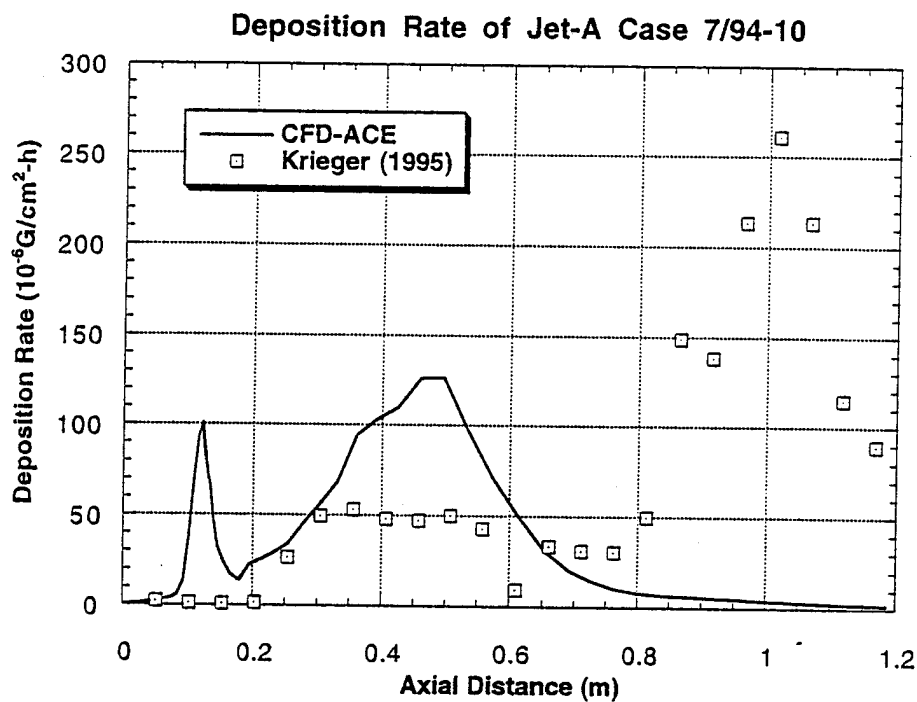


Figure 9-4b. Predicted Deposition Rates of Case 7/94-10

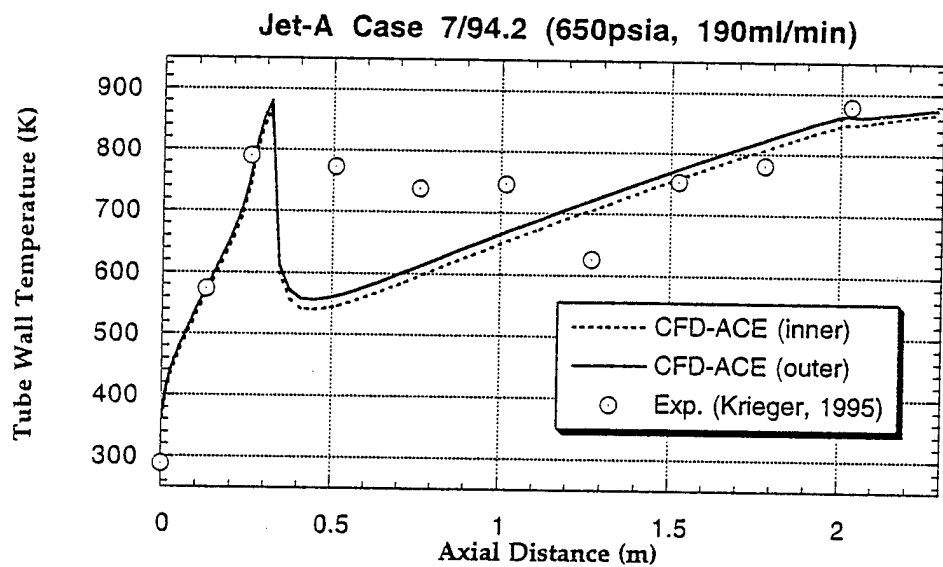


Figure 9-5a. Predicted Wall Temperatures for Case 7/94-2

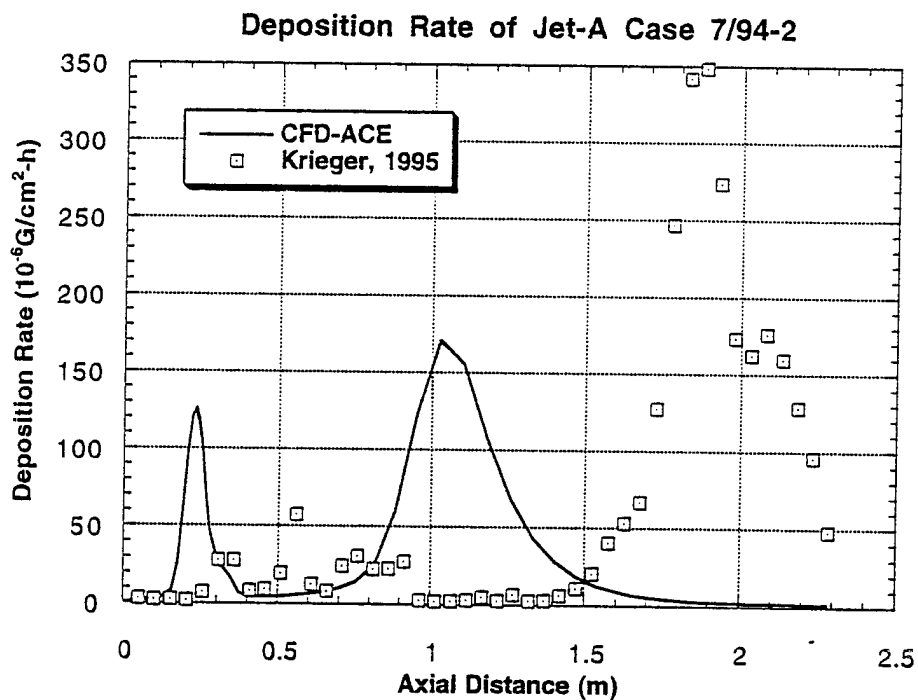


Figure 9-5b. Predicted Deposition Rates for Case 7/94-2

9.3 Discussion of Results

It is important to understand the precise reason for the discrepancies between predictions and the measured data. One significant problem has been the determination of the accuracy of the measurements. In some instances the measured values of wall temperature exceeded the furnace temperature which is physically unrealistic. However, the models also need further improvement in the following areas: (i) three-dimensional effects due to buoyancy induced turbulence need to be considered, (ii) the chemistry model needs to be recalibrated for the high temperature regime, and (iii) the original Katta model did not correctly predict the location of the deposition peaks (see Figure 8-2) which indicates that further improvement in the chemistry model is necessary.

Analyses of the experimental data show multiple peaks in deposition rate along the fuel tube during the experiments. This phenomenon is also predicted by the models used in the study. The following discussion presents an explanation for the multiple peaks by examining the local values of temperatures, oxygen concentration and turbulent kinetic energy.

The operating conditions are chosen to correspond to the experimental case 7/94-6 except that a uniform heat flux is assumed at the tube wall. The heat flux is treated as a parameter in this study. Three different simulations corresponding to heat flux values of 200, 300, and 400 KW/m² are performed. A laminar velocity profile is assumed at the inlet.

Figure 9-6a shows the wall and bulk fluid temperatures along the length of the tube for the three cases. It is observed that all cases show a sharp peak in the wall temperature a short distance downstream of the inlet. The reason for this peak is that the flow is essentially laminar in the inlet region and the smaller diffusion transport causes the wall temperatures to increase sharply (see also Figures 9-7a, 9-8a, and 9-9a). However, as the flow becomes turbulent (see turbulent kinetic energy distributions in Figures 9-7c, 9-8c, and 9-9c) the diffusion transport increases and the wall temperatures show an abrupt decrease from the peak value and a gradual increase along the tube. Figure 9-6b shows the deposition rate (on the wall) along the tube for the three cases. It is observed that there is a peak close to the inlet

followed by another peak at a downstream location. Comparing Figures 9-6a and 9-6b it is obvious that the first peak is caused by the sudden rise in the temperature near the inlet. The local hot spot will result in the reaction of the dissolved O_2 (see Figures 9-7b, 9-8b and 9-9b) to form the deposition precursor very near the wall to give rise to the first deposition peak.

The formation of the second peak however, is more dominated by what happens in the bulk flow, i.e., it is not a local process. As the flow becomes turbulent and the bulk fluid gets heated, the reaction in the bulk fluid gives rise to precursors. These precursors are transported to the wall by turbulent diffusion giving rise to the second peak. Figures 9-7b, 9-8b and 9-9b illustrate the occurrence of the deposition peaks by looking at gradients in oxygen concentration. It is obvious from the figures that the first peak is a local phenomena while the second peak corresponds to oxygen concentration gradients in the bulk fluid.

Figures 9-10a and 9-10b show the computed results for a heat flux of 300 kW/m^2 for three different surface reaction models. The first model considers only reaction 7 on the surface, the second model considers only reactions 8 and 9 on the surface and the third model considers reactions 7, 8 and 9. It is observed from Figure 9-10a that reaction 7 by itself is unable to predict the deposition peaks. The model with reactions 8 and 9 only is very close to the full model indicating that these reactions are the dominant mechanisms for deposition. Figure 9-10b shows the deposition rates on a log scale. It is observed that at deposition rates smaller than $1.0 \mu\text{g/cm}^2\text{-hr}$, reaction 7 is dominant. For higher deposition rates, reactions 8 and 9 (reaction 8 in particular) are the major contributors to the bulk production of the precursor.

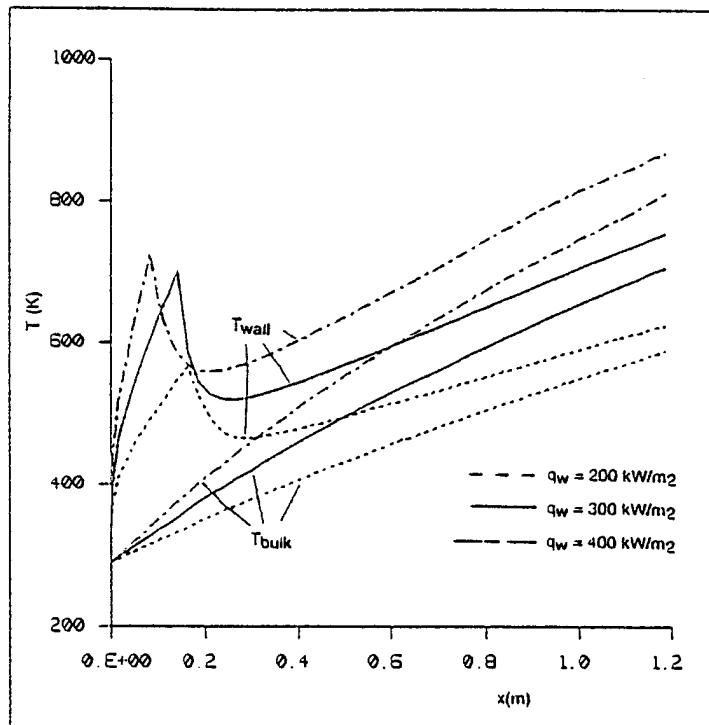


Figure 9-6a. Wall/Bulk Fluid Temperatures Along the Tube

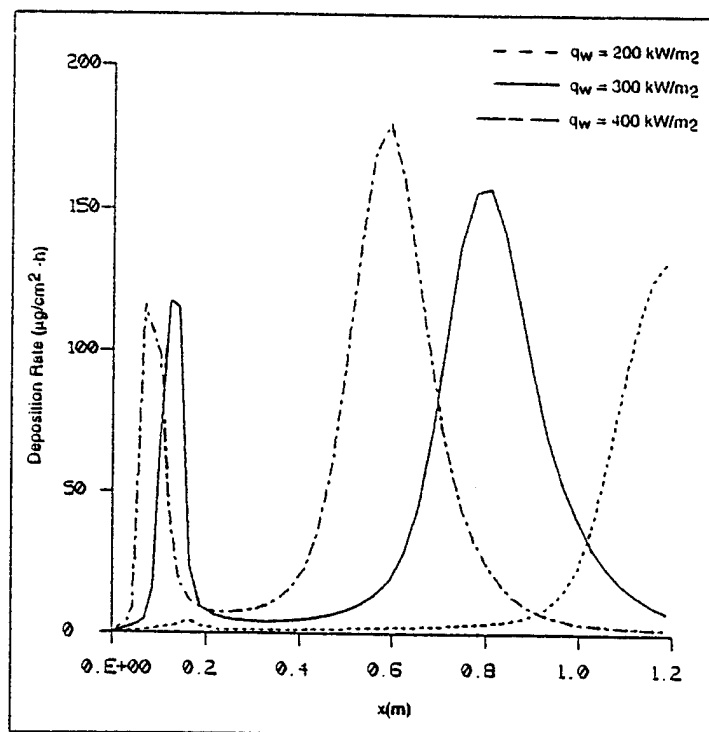
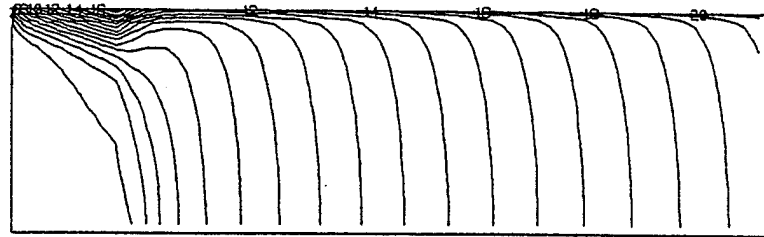


Figure 9-6b. Deposition Rate Along the Tube

```

TEMP  CONTOURS
FMIN  2.878E+02
FMAX  6.251E+02
CONTOUR LEVELS
 2    3.046E+02
 4    3.384E+02
 6    3.721E+02
 8    4.059E+02
10    4.396E+02
12    4.733E+02
14    5.071E+02
16    5.408E+02
18    5.745E+02
20    6.083E+02
OK>

```

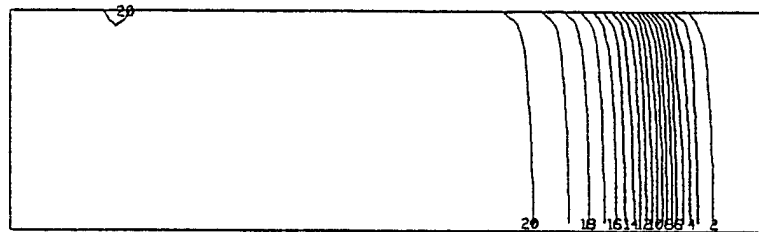


(a) temperature distribution

```

F1    CONTOURS
FMIN  9.177E-09
FMAX  5.000E-05
CONTOUR LEVELS
 2    2.509E-06
 4    7.508E-06
 6    1.251E-05
 8    1.751E-05
10    2.251E-05
12    2.750E-05
14    3.250E-05
16    3.750E-05
18    4.250E-05
20    4.750E-05
OK>

```

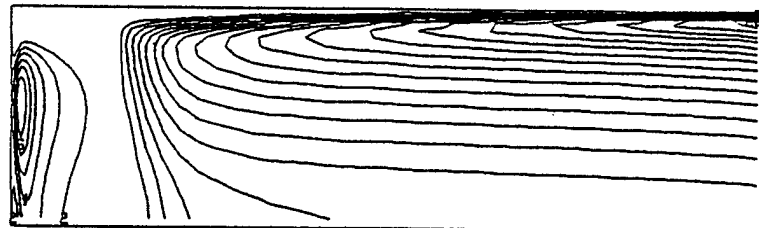


(b) oxygen mass fraction distribution

```

TKE1  CONTOURS
FMIN  2.071E-12
FMAX  4.432E-02
CONTOUR LEVELS
 2    2.216E-03
 4    6.649E-03
 6    1.108E-02
 8    1.551E-02
10    1.995E-02
12    2.438E-02
14    2.881E-02
16    3.324E-02
18    3.768E-02
20    4.211E-02
OK>

```



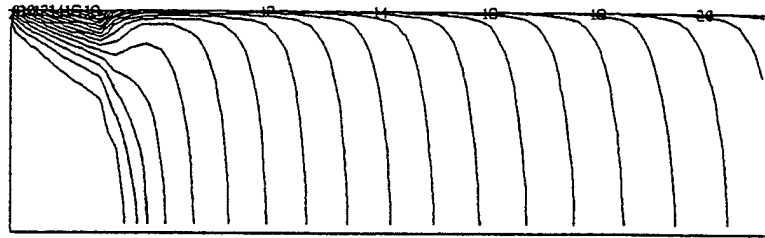
(c) turbulent kinetic energy distribution

Figure 9-7. Results for $q_w = 200 \text{ kW/m}^2$

```

TEMP  CONTOURS
FMIN   2.878E+02
FMAX   7.531E+02
CONTOUR LEVELS
  2    3.110E+02
  4    3.576E+02
  6    4.041E+02
  8    4.507E+02
 10    4.972E+02
 12    5.437E+02
 14    5.903E+02
 16    6.368E+02
 18    6.833E+02
 20    7.299E+02
OK>

```

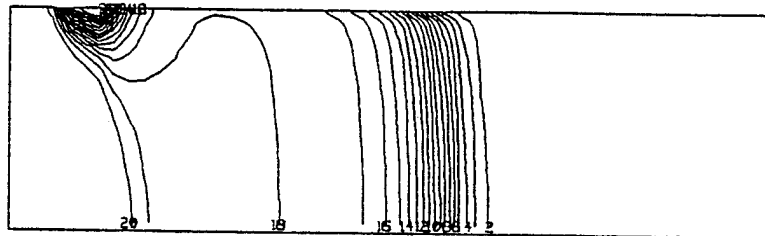


(a) temperature distribution

```

F1     CONTOURS
FMIN   2.162E-23
FMAX   5.000E-05
CONTOUR LEVELS
  2    2.500E-06
  4    7.500E-06
  6    1.250E-05
  8    1.750E-05
 10    2.250E-05
 12    2.750E-05
 14    3.250E-05
 16    3.750E-05
 18    4.250E-05
 20    4.750E-05
OK>

```

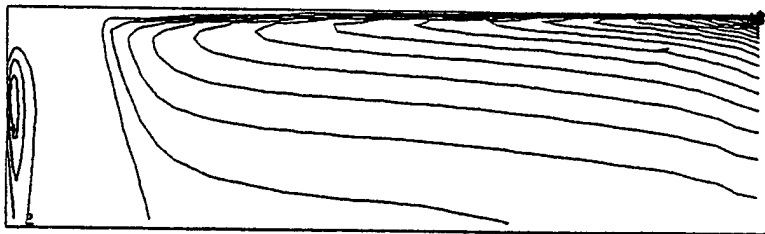


```

TKE1   CONTOURS
FMIN   4.737E-12
FMAX   8.704E-02
CONTOUR LEVELS
  2    4.352E-03
  4    1.306E-02
  6    2.176E-02
  8    3.046E-02
 10    3.917E-02
 12    4.787E-02
 14    5.658E-02
 16    6.528E-02
 18    7.398E-02
 20    8.269E-02
OK>

```

(b) oxygen mass fraction distribution



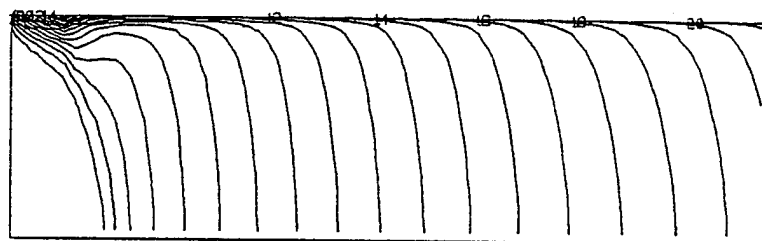
(c) turbulent kinetic energy distribution

Figure 9-8. Results for $q_w = 300 \text{ kW/m}^2$


```

TEMP  CONTOURS
FMIN  2.878E+02
FMAX  8.676E+02
CONTOUR LEVELS
  2    3.168E+02
  4    3.748E+02
  6    4.327E+02
  8    4.907E+02
 10    5.487E+02
 12    6.067E+02
 14    6.647E+02
 16    7.227E+02
 18    7.807E+02
 20    8.386E+02
OK>

```

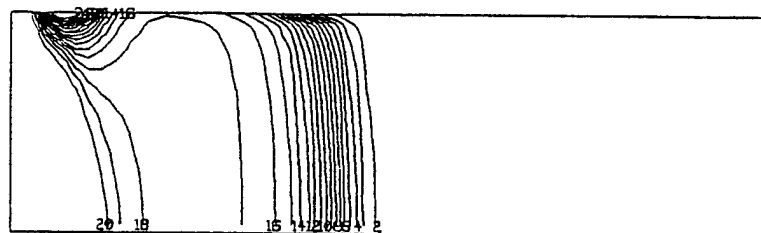


(a) temperature distribution

```

F1  CONTOURS
FMIN  4.598E-25
FMAX  5.000E-05
CONTOUR LEVELS
  2    2.500E-06
  4    7.500E-06
  6    1.250E-05
  8    1.750E-05
 10    2.250E-05
 12    2.750E-05
 14    3.250E-05
 16    3.750E-05
 18    4.250E-05
 20    4.750E-05
OK>

```

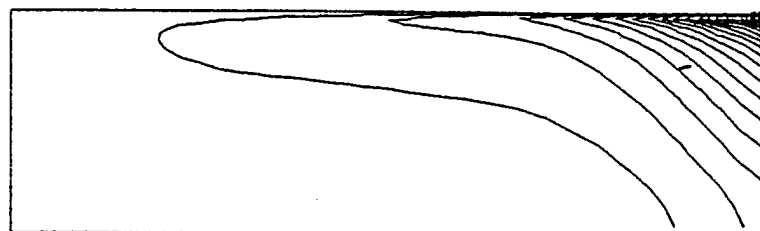


(b) oxygen mass fraction distribution

```

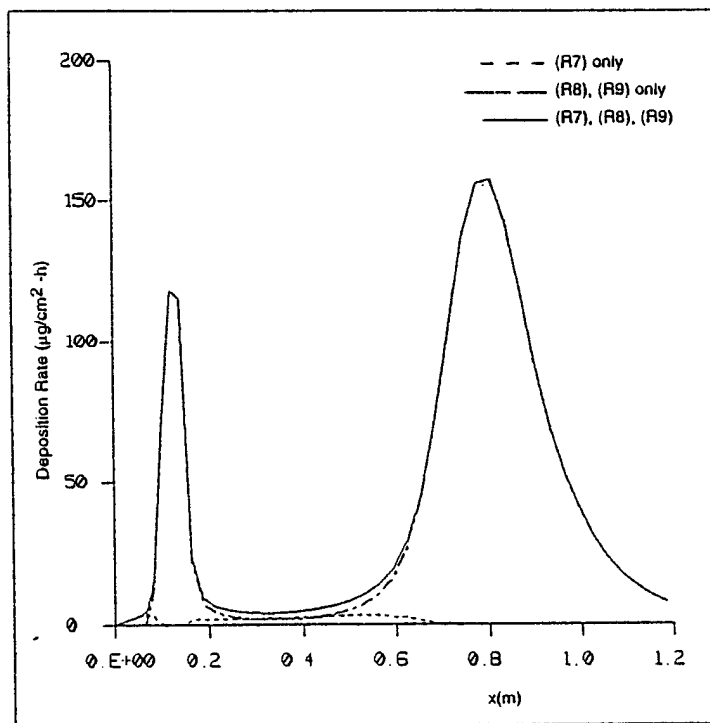
TKE1 CONTOURS
FMIN  9.531E-12
FMAX  3.802E-01
CONTOUR LEVELS
  2    1.901E-02
  4    5.703E-02
  6    9.504E-02
  8    1.331E-01
 10    1.711E-01
 12    2.091E-01
 14    2.471E-01
 16    2.851E-01
 18    3.231E-01
 20    3.612E-01
OK>

```

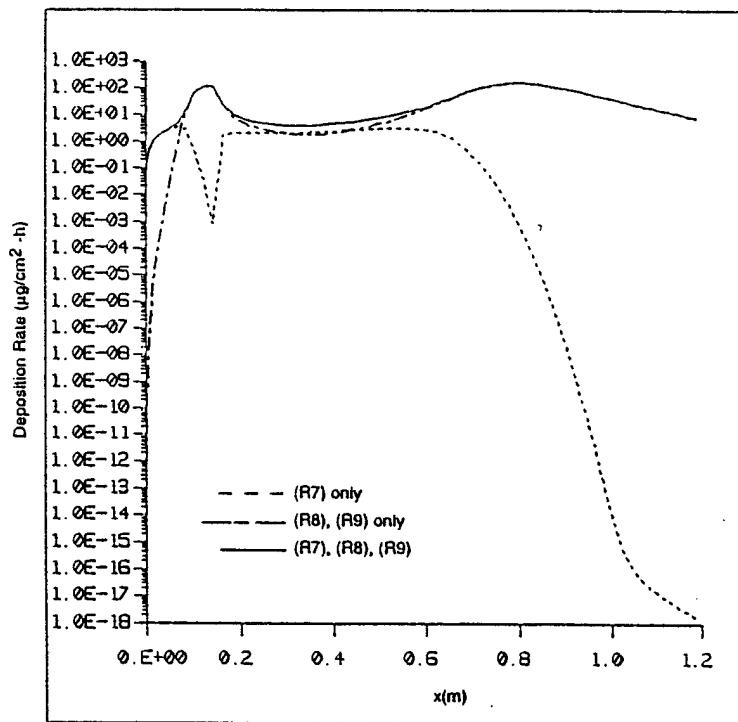


(c) turbulent kinetic energy distribution

Figure 9-9. Results for $q_w = 400 \text{ kW/m}^2$



(a) temperature distribution



(b) oxygen mass fraction distribution

Figure 9-10. Computational Results with 3 Different Surface Reaction Models

10. BENCHMARK VALIDATION STUDY FOR HEAT TRANSFER MODEL

This section presents the results from a series of simulations done to model the experiments conducted at the University of Iowa on heat transfer in SF_6 flow.

10.1 SF_6 Experiments

In the experiment, pressurized SF_6 enters a thin stainless steel tube, which is heated by radiation from a furnace. Test conditions included two flow rates and reduced pressures ranging from 0.75 to 1.5. The details of the experiment are described in Section 4. Test cases corresponding to flow rates of 150 and 450 ml/min, at pressures of 400, 531 and 700 psia are simulated. The predictions of tube wall and bulk fluid temperature at the flow exit are compared with the measurements.

The set-up of the numerical problem is illustrated in Figure 10-1. The chamber is assumed to be filled with stationary air and heat transfer is accomplished by radiation (zero absorptivity) and thermal conduction (conductivity of 0.05 W/mK and specific heat is 1000 J/kgK). Conjugate heat transfer is modeled at air/tube, and tube/ SF_6 interfaces. The thermal properties of the tube are assumed as conductivity = 20 W/mK and specific heat = 550 J/kgK. The turbulence is modeled by the low Reynolds number k- ϵ model and a turbulent Prandtl number of 0.9 is assumed.

10.2 Computational Results

The computational results and comparison with data are described below for the two flow rates.

Flow Rate 150ml/min: This flow rate corresponds to an inlet Reynolds number of about 2,000. The results for temperature at flow exit vs. furnace temperature are presented in Figure 10-2. From the enthalpy curve for SF_6 (see Figure 5-4d), it is observed that a large amount of energy input is needed to get the temperature over the pseudo-critical point for pressures of 400 and 531 psia. This is reflected in the bulk temperature predictions (Figures 10-2 and 10-3) which are flat at 30 and 45°C (302 and 318°K), the pseudocritical temperatures for 400 and 531 psia, respectively.

However, the measured bulk temperatures show an increasing trend. For a pressure of 700 psia (see Figure 10-4), the enthalpy curve shows a continuous increase, and the predicted bulk temperature is increasing steadily, but still lower than the measured value.

For wall temperatures, the predictions show similar trends as the data (for 400 and 531 psia), except that the predicted wall temperatures are higher than the data. At 700 psia, however, the predicted values are lower than the data. This may be accounted for by the trend of increasing laminar thermal conductivity with increase in pressure.

Flow Rate 450 ml/min: This flow rate corresponds to an inlet Reynolds number of about 10,000 and the turbulent transport effect is more dominant than in the previous cases. Figures 10-5, 10-6 and 10-7 show the results for pressures of 400, 531 and 700 psia, respectively. These results also show lower bulk temperature predictions compared to the data but the increasing trend is captured. For the wall temperature, the predicted values are lower than the measured data, for furnace temperatures higher than 600°C. It needs to be pointed out that in the experiment, the thermo-couples attached to the steel tube acted as extra conductive wires for heat transfer to the tube. Also, it was found the temperature readings from thermo-couples were higher (up to 50%) than the actual value, especially at high temperatures. Considering the uncontrolled experimental conditions and measurement error, the predicted temperature curves are quantitatively comparable to the experimental results.

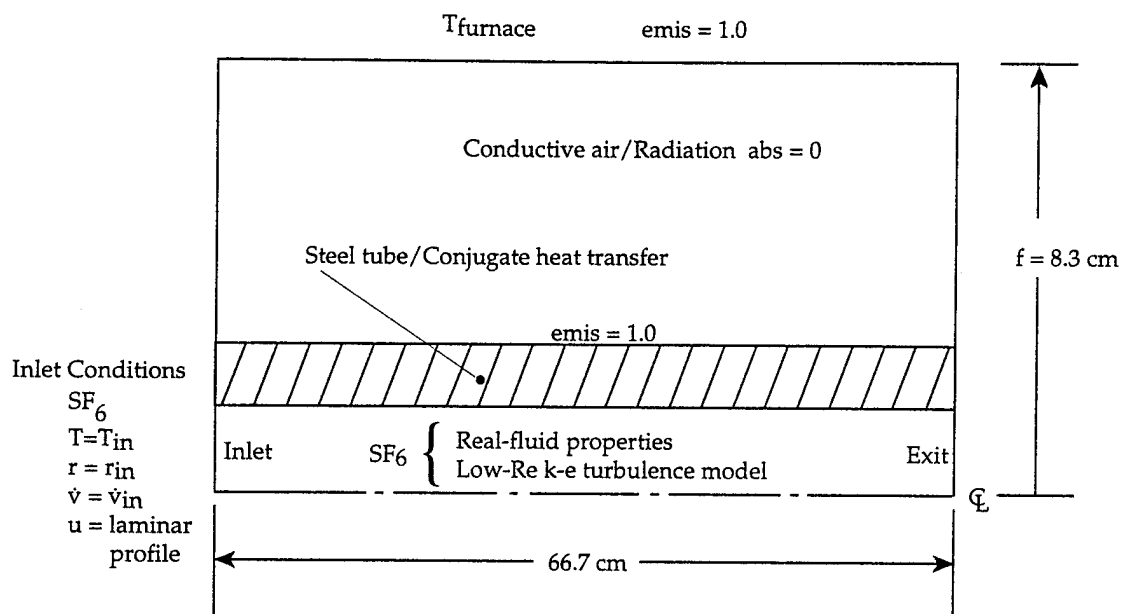


Figure 10-1. Schematic of Numerical Problem

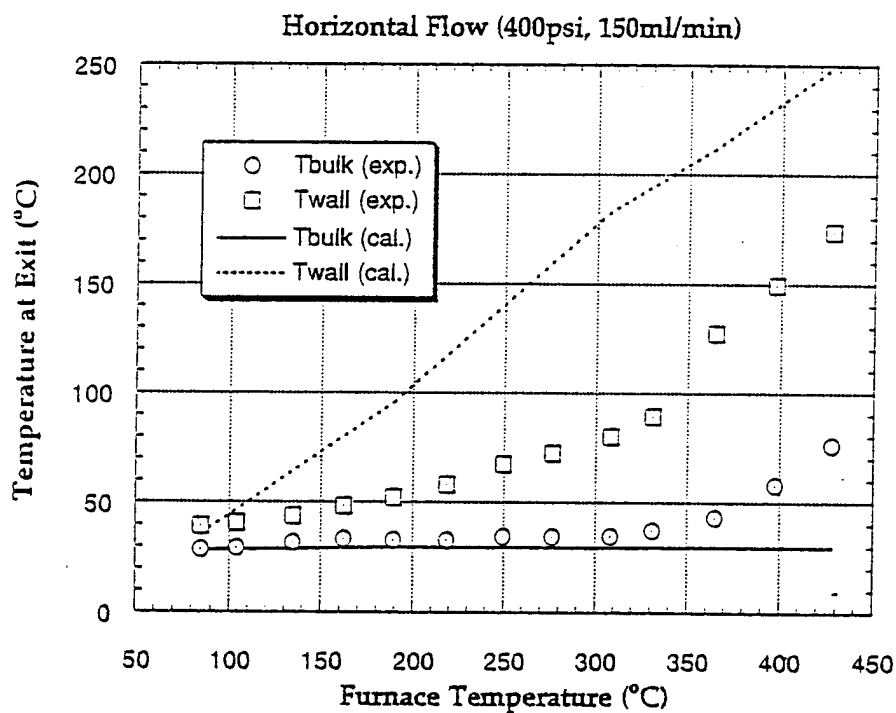


Figure 10-2. Results for $p = 400 \text{ psia}$ and $Q = 150 \text{ ml/min}$

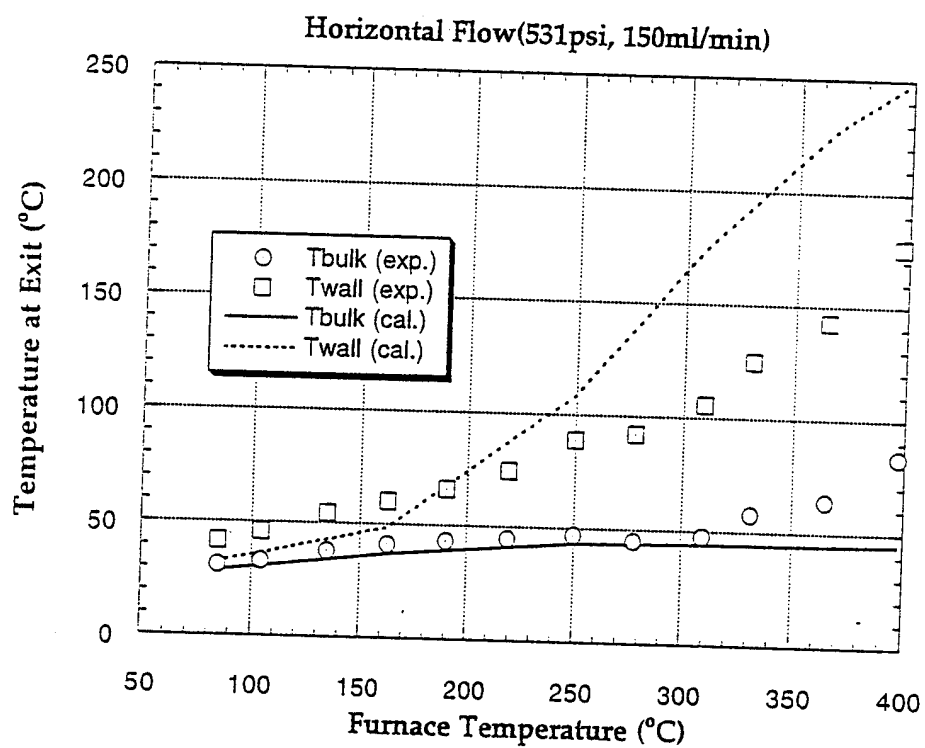


Figure 10-3. Results for $p = 531$ psia and $Q = 150$ ml/min

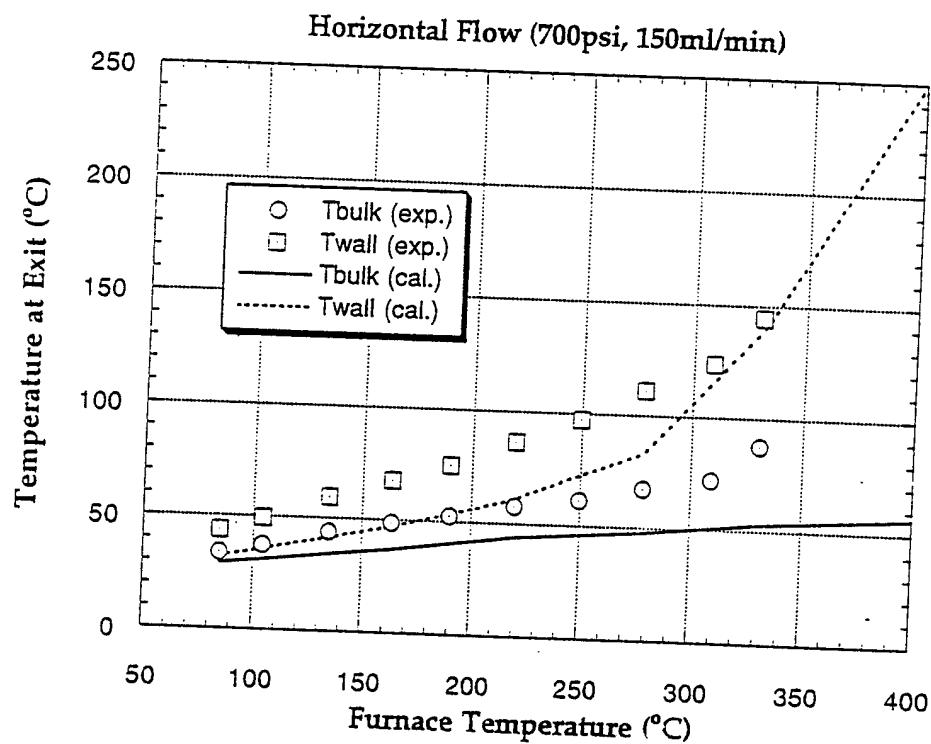


Figure 10-4. Results for $p = 700$ psia and $Q = 150$ ml/min

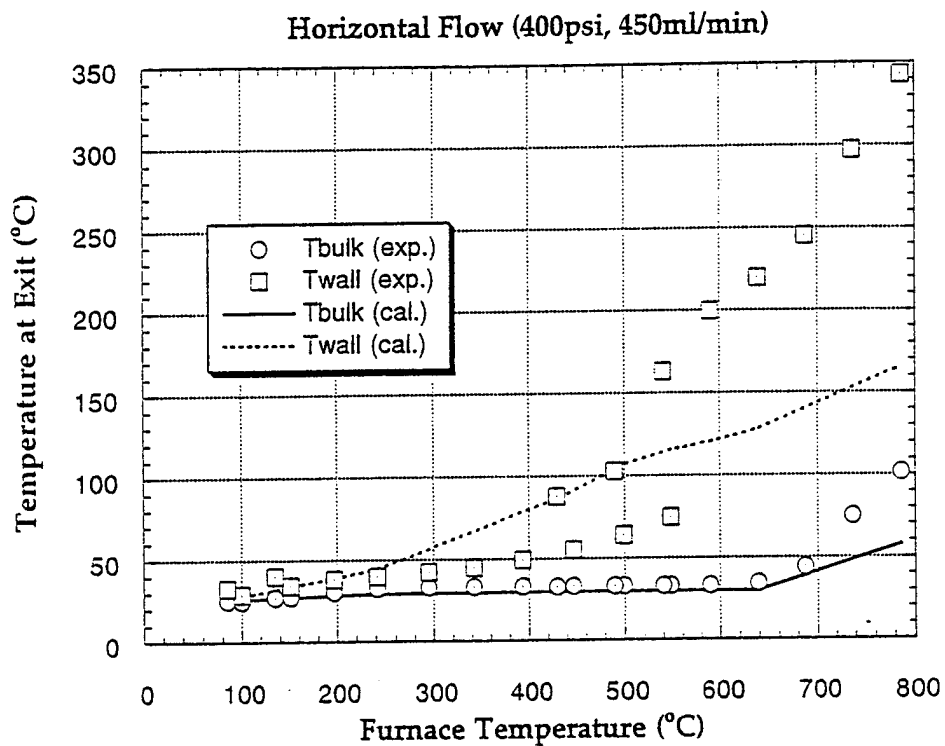


Figure 10-5. Results for $p = 400$ psia and $Q = 450$ ml/min

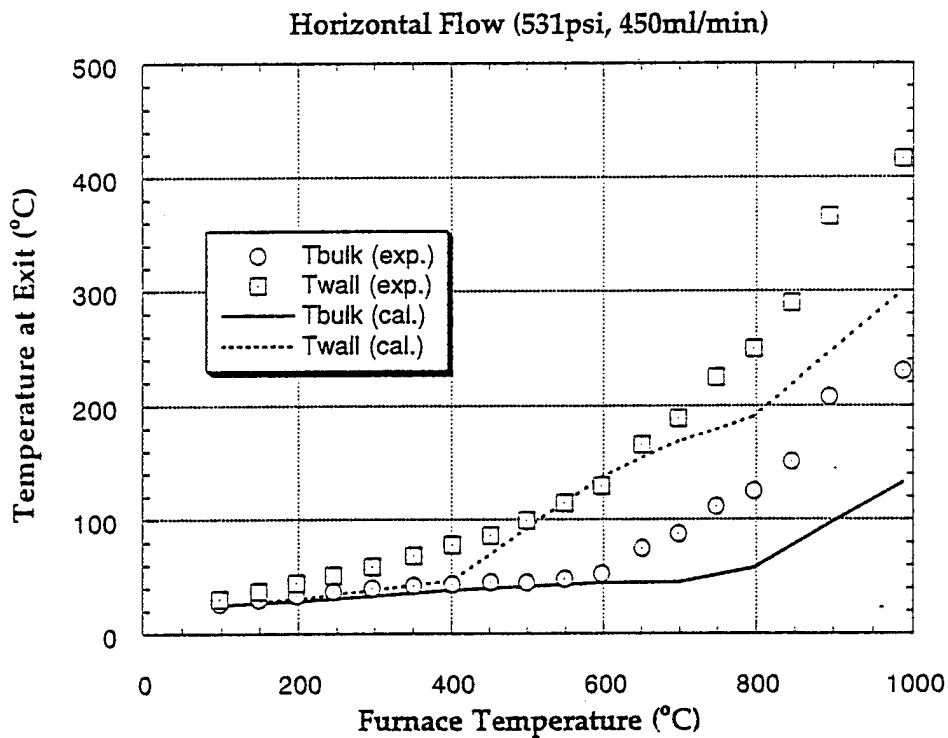


Figure 10-6. Results for $p = 531$ psia and $Q = 450$ ml/min

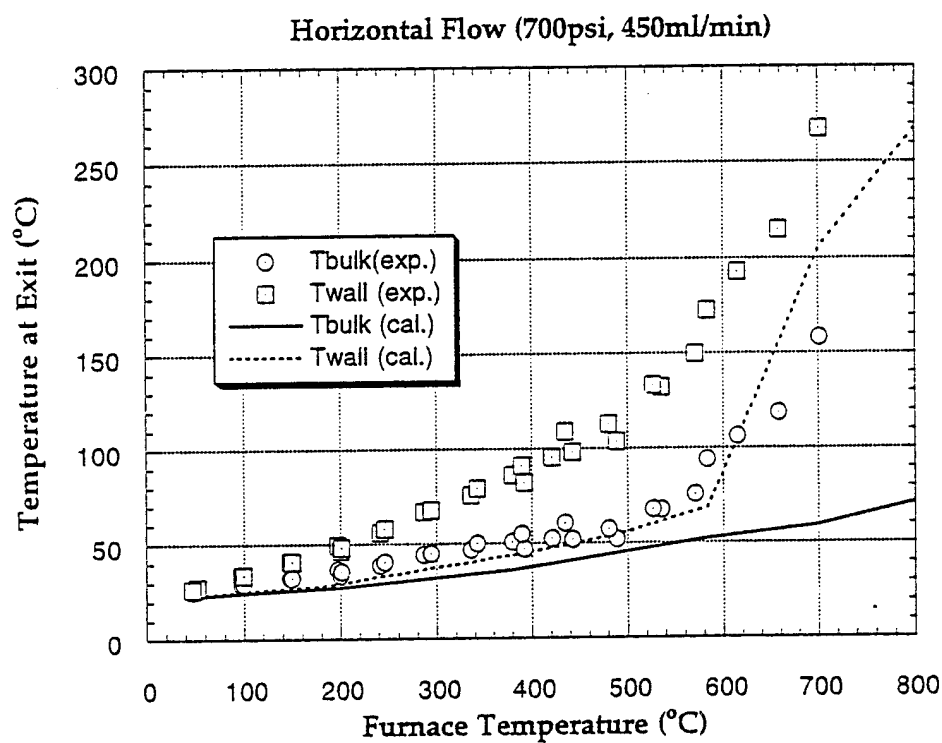


Figure 10-7. Results for $p = 700$ psia and $Q = 450$ ml/min

11. COMPUTATIONAL RESULTS FROM THE LES STUDY

This section presents the computational results obtained from the Large Eddy Simulation (LES) study of the flow of supercritical CO₂ in a tube. The main objective of this study was to resolve inherent unsteadiness (if any) in flows of supercritical fluids.

11.1 Problem Definition

The problem of CO₂ flow in a channel is considered (see schematic in Figure 11-1a). This problem has been described in detail in Section 7. The pressure in the channel is above the critical pressure of CO₂. The inlet temperature is below the critical temperature. However, heating from the constant temperature wall causes the fluid temperature to increase beyond the critical value. This flow was studied in detail (see Section 7) for a range of Reynolds numbers and for upward as well as downward flow configurations (with respect to gravity).

The computational grid for the LES study is shown in Figure 11-1b. The grid is made considerably finer (compared to the one used in the earlier study described in Section 7) in order to resolve any inherent unsteadiness (due to small scale structures) in these flows. The transient governing equations (i.e., with the time dependent terms) are solved for this problem with a time step of $\Delta T = 0.01$ secs. In addition, the temperature is monitored at several locations in the channel to determine the nature of time dependence. Figure 11-1c shows the monitoring locations. The locations 1, 2, and 3 are placed very close to the wall to monitor near wall effects.

11.2 Results from the LES Study

A series of simulations were performed for three Reynolds numbers of 10,000, 100,000 and 1,000,000, respectively. For each Reynolds number, three cases corresponding to upward flow (flow against gravity), downward flow (flow in the direction of gravity) and horizontal flow (flow perpendicular to gravity) were analyzed.

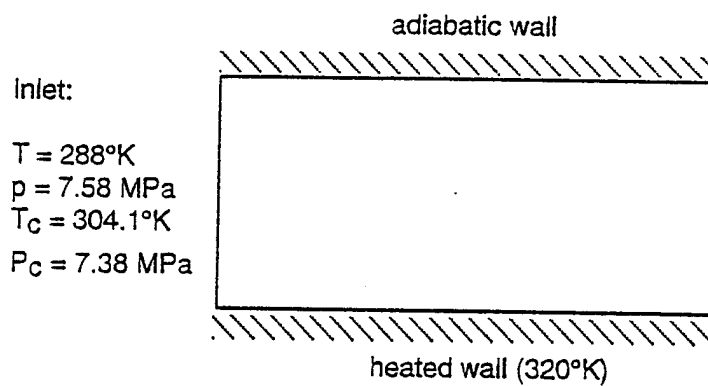


Figure 11-1a. Schematic of the Problem

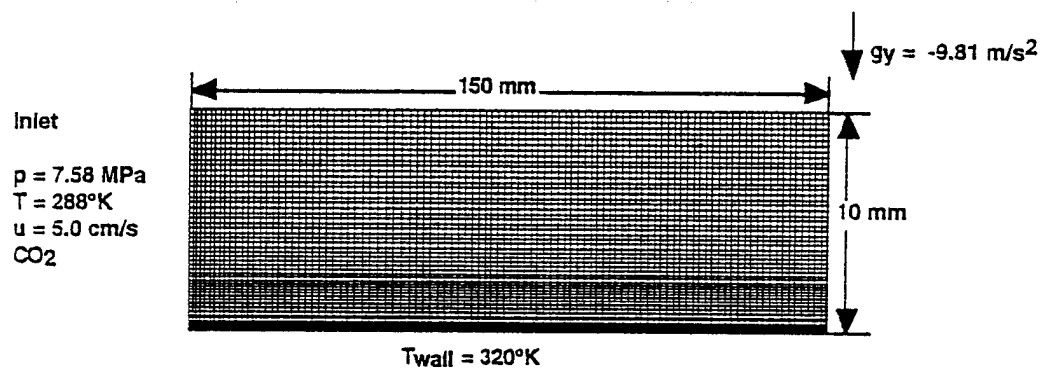


Figure 11-1b. Computational Grid (100x60) for the Problem

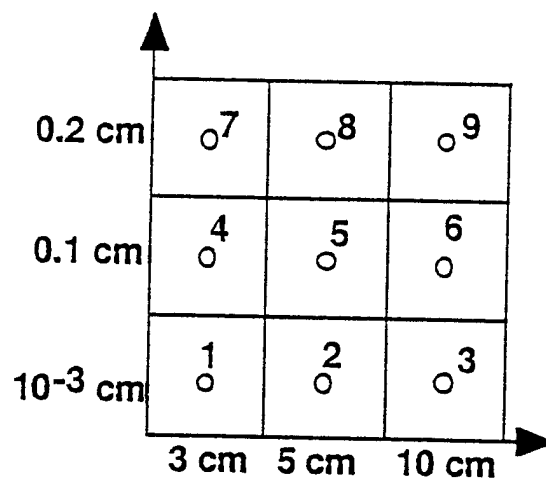


Figure 11-1c. Schematic of Monitoring Locations

Figure 11-2 shows the computed heat flux along the wall (for $Re = 10,000$) for the three flow configurations. The upward and downward flow cases converged to steady state solutions and the predicted values of heat flux compared exactly with the values obtained earlier (see Section 7) with the steady state (coarse grid) model. However, the case of horizontal flow shows a significant amount of flow unsteadiness and the computed heat flux (in Figure 11-2) shows large spatial oscillations. Figure 11-3 shows the instantaneous temperature distribution in the channel. It is observed that mushroom shaped structures emanating from the wall give rise to flow unsteadiness. This has been observed in experiments where the large density gradient near the wall (due to the fluid becoming supercritical) interacts with gravity to produce buoyancy driven structures. Figure 11-4 shows the density distribution in the channel. It is observed that the density near the wall is lower (by almost a factor of four) than the bulk density due to the fluid becoming supercritical.

Figures 11-5a-c show the calculated temperatures as functions of time at the different monitoring locations. It is observed that the buoyancy driven flow causes small scale eddies to be shed off the wall. The monitoring locations near the wall (Figure 11-5a) show a significant amount of intermittency. However, the temperatures at locations 4, 5 and 6 (0.1 cm above the wall) shown in Figure 11-5b indicate that the frequency of intermittency at these locations is approximately half that of locations 1, 2 and 3. This indicates that the small scale eddies near the wall undergo pairing (or merging) a certain distance away from the wall to give rise to the lower frequencies. Figure 11-5c shows the temperature locations 7, 8 and 9 (0.2 cm from the wall). The frequency of intermittency is approximately the same as what was observed at locations 4, 5, and 6.

The cases corresponding to $Re = 100,000$ and $Re = 1,000,000$ did not show any transient behavior irrespective of the flow orientation, i.e., they converged to steady state solutions that matched exactly with the results obtained from the steady state model.

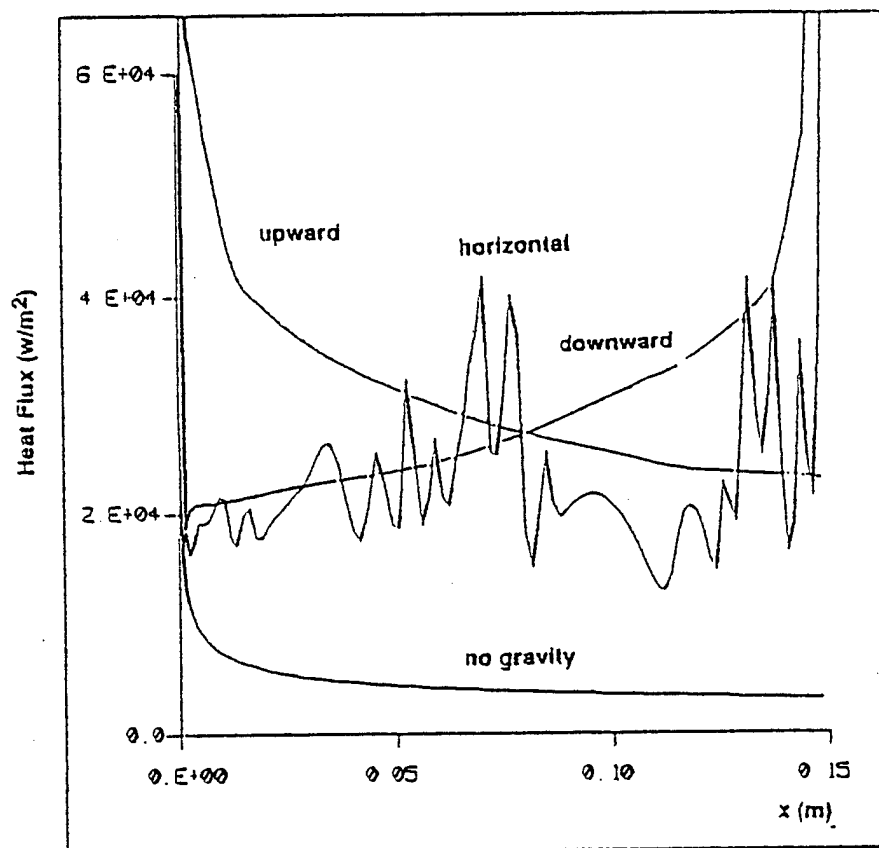


Figure 11-2. Predictions of Heat Flux Along the Heated Wall of the Channel

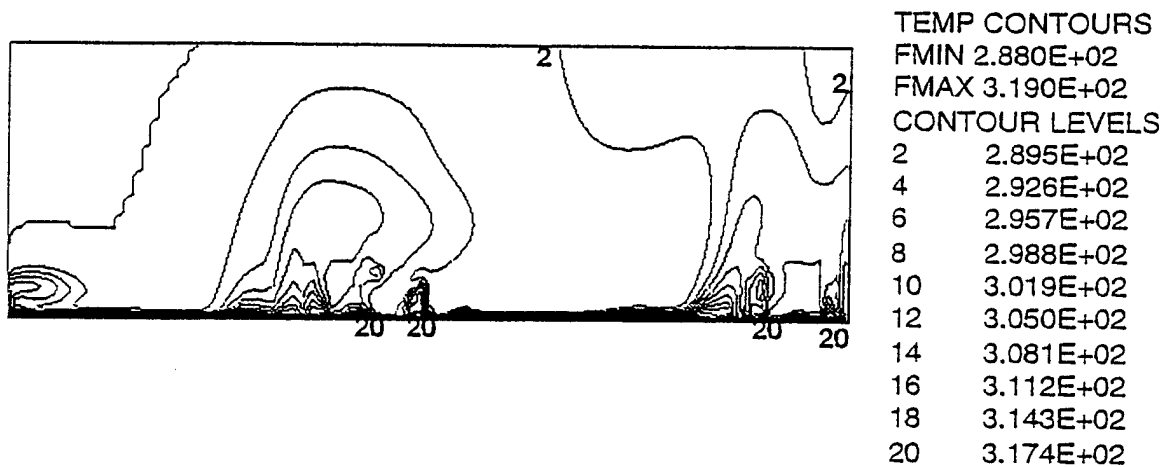


Figure 11-3a. Temperature Distribution in the Channel

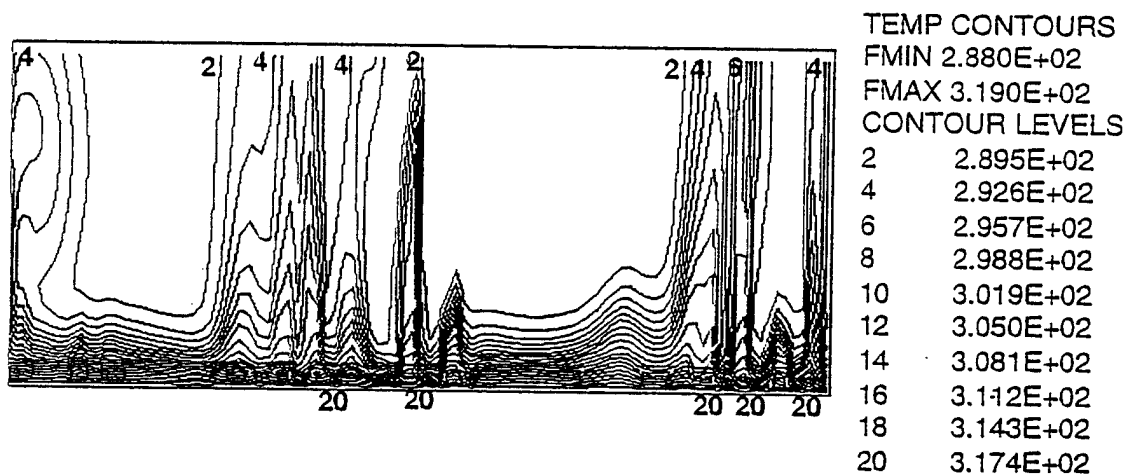


Figure 11-3b. Magnified View of Temperature Distribution Near the Heated Wall

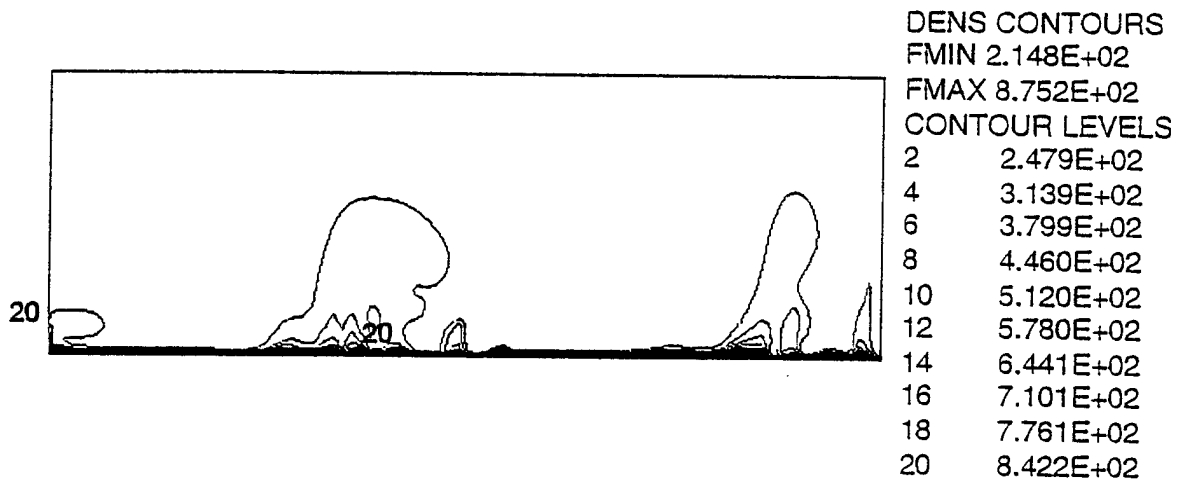


Figure 11-4a. Density Distribution in the Channel

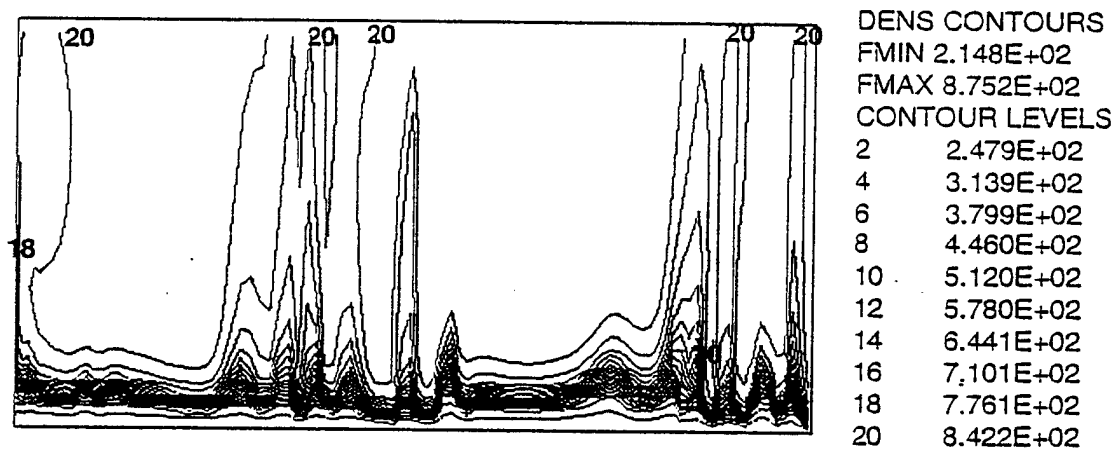


Figure 11-4b. Magnified View of Density Distribution Near the Heated Wall

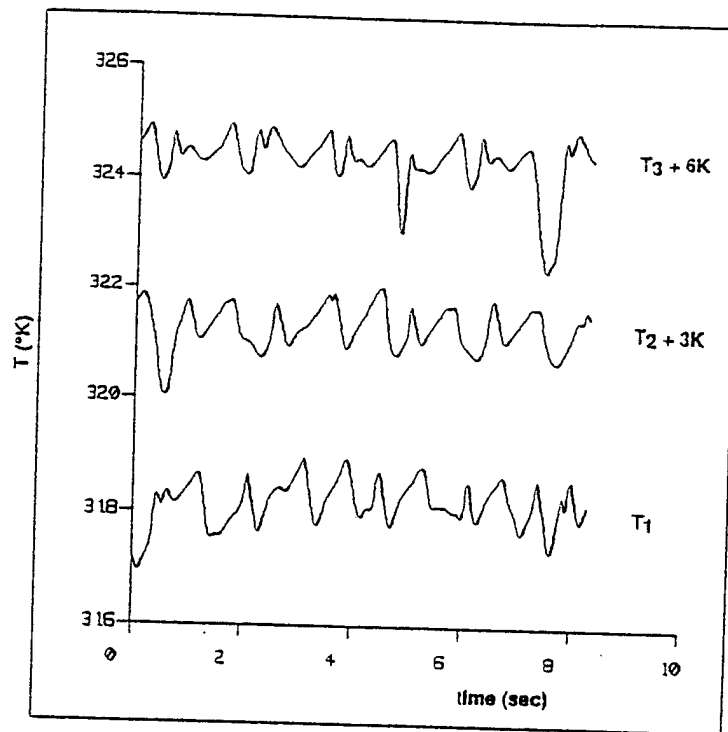


Figure 11-5a. Transient Temperature Behavior at Locations (1, 2, and 3) 1 mm Above the Heated Wall

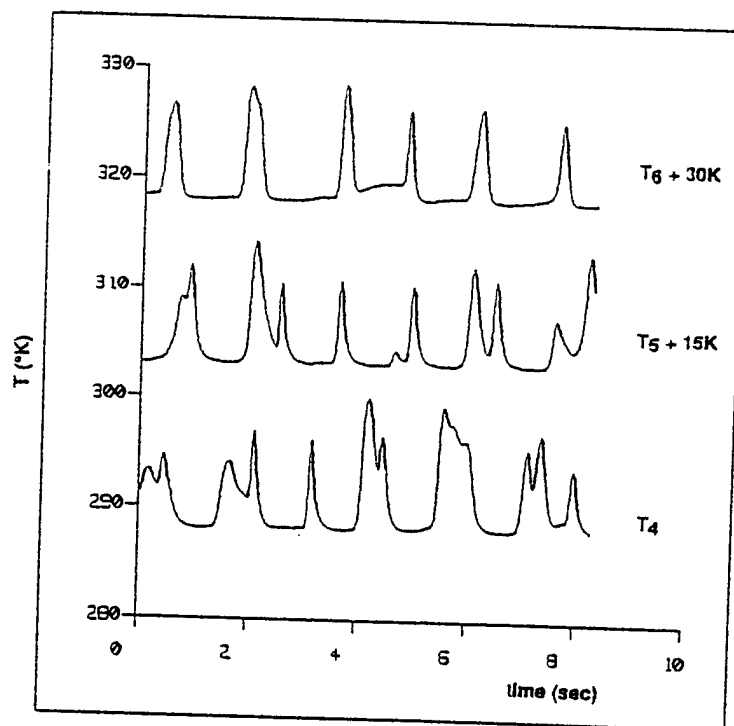


Figure 11-5b. Transient Temperature Behavior at Locations (4, 5, and 6) 0.1 cm Above the Heated Wall

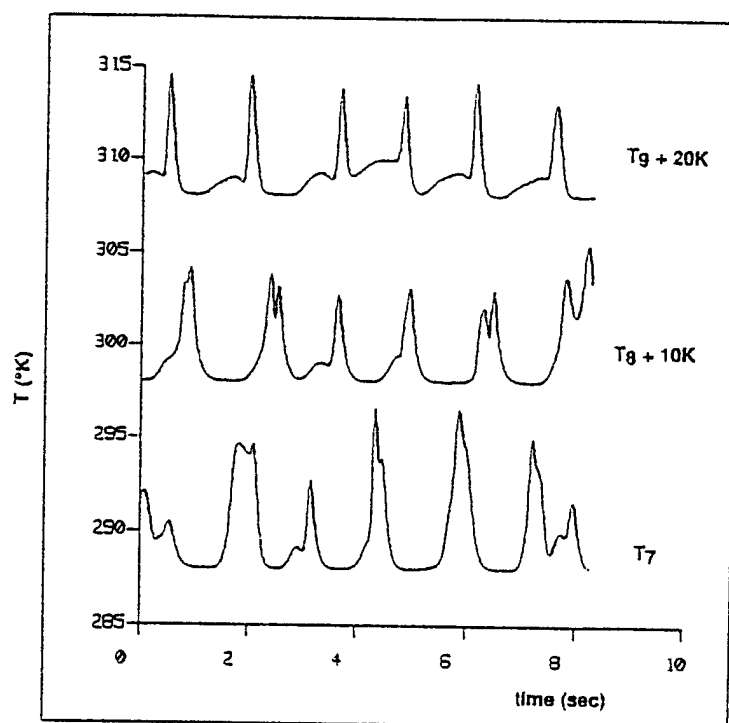


Figure 11-5c. Transient Temperature Behavior at Locations (7, 8 and 9) 0.2 cm Above the Heated Wall

11.3 Discussion

The results show that the only unsteadiness that was observed in the simulations was that produced by buoyancy effects. Also, the unsteadiness was observed only at low Reynolds numbers (of the order of 10,000) and for horizontal flow configurations. For higher Reynolds numbers and for upward/downward flow configurations, the transient model converged to steady state solutions that matched the results produced by the steady state model.

Therefore, the transient simulations do not show any inherent unsteadiness in supercritical flows other than buoyancy effects. Also, it is clear that it is not necessary to invoke the transient model if the steady state model yields a converged solution. Only for cases where the steady state model fails to yield a converged solution (i.e., for the case of $Re = 10,000$ and horizontal flow) will the transient model be useful in terms of predicting intermittency and the local frequency of unsteady behavior.

12. CONCLUSIONS

This section presents the conclusions from the Phase II study and plans for future extensions and applications of the models developed during this study.

12.1 Summary of Phase II Work

The completion of the Phase II study has resulted in the following accomplishments:

Incorporation of a Real Fluid Transport Model: Models for computation of thermophysical properties of real fluids were incorporated into a general purpose CFD code. These models facilitate the computation of local thermodynamic and transport properties as a function of pressure, temperature and composition. Steep variations in these properties at the critical (or pseudo-critical) point can be resolved reasonably well by this model. A detailed database has been incorporated into the code to handle a range of fluids including a number of hydrocarbon fuels. The CFD code, CFD-ACE, is a general purpose transport code that solves the fluid flow, heat transfer and chemistry in complex engineering systems. The turbulence models in CFD-ACE were modified appropriately to account for the flow of supercritical fluids.

Computation of Heat Transfer in Supercritical Fluids: The models were applied to analyze heat transfer in supercritical fluids over a range of flow conditions from the laminar to the turbulent regime. The effect of turbulence and buoyancy was studied in detail. The predictions of the model were compared with experimental data. It was demonstrated that buoyancy may play a significant role in influencing heat transfer even at Reynolds numbers as high as 100,000. The direction of body forces with respect to flow direction was also found to be very important in determining heat transfer in the intermediate range of Reynolds numbers.

Computation of Thermal Stability in Jet Fuels: Advanced thermal stability models developed at Wright Laboratory were incorporated into the code. The models were tested for physical accuracy as well as numerical stability. The model predictions were compared with deposition data in the literature as well as data obtained from an experimental study conducted under this project. The comparisons were used to

further refine and calibrate the models.

Experimental Study: A detailed experimental study was performed at the University of Iowa as well as Wright Laboratory to obtain benchmark validation data for the models. The experiments were done on jet fuels (Jet-A) as well as simulant fluids such as SF_6 . The experiments on fuels yielded data on temperature distributions as well as deposition rates and the experiments on SF_6 yielded data on wall temperature distributions. These data were used to assess the validity of the model and to refine and calibrate model constants.

The completion of the Phase II study has resulted in a code that will enable the computation of heat transfer and fuel thermal stability in complex aircraft heat management systems. The code can be used to study the effects of various operating conditions on the performance of the system.

12.2 Plans for Future Work

An immediate extension of the Phase II work has been in the application of these models to analyze endothermic chemistry in aircraft fuel systems. This is a project that CFDRC is currently executing for the US Air Force in collaboration with organizations such as Wright Laboratory and Pratt & Whitney. CFDRC is also exploring the potential of commercializing this code to organizations developing aircraft fuel system components such as Pratt & Whitney, Delavan, AlliedSignal, GEAE, etc.

The current Phase II work has also laid the foundation for developing a general purpose capability for the analysis of supercritical fluids. Many engineering applications (such as cleaning solvents, high pressure systems, etc.) involve the use of supercritical fluids. CFDRC will pursue these and other opportunities for applying the models developed during this study.

12.3 Publications Resulting from the Phase II Study

The publications resulting from the Phase II study are listed below.

- a. N. Zhou and A. Krishnan, "Calibration of a Global Mechanism for Jet Fuel Deposition," to be presented as AIAA-96-3238, at the 32nd AIAA/ASME/SAE/ASEE Joint Propulsion Conference, Lake Buena Vista, FL, July 1-3, 1996
- b. N. Zhou and A. Krishnan, "Numerical Simulation of Coupled Heat Transfer Characteristics for Flows at Supercritical Pressure," to be presented as paper 96-178, at the 31st Intersociety Energy Conversion Engineering Conference, Washington DC, August 11-16, 1996.
- c. N. Zhou and A. Krishnan, "Laminar and Turbulent Heat Transfer in Supercritical Fluids," presented at 1995 National Heat Transfer Conference, Portland, OR, Aug. 5-8, 1995
- d. N. Zhou and A. Krishnan, "Supercritical Heat Transfer in Aircraft Fuel Systems," presented at the 31st AIAA/ASME/SAE/ASEE Joint Propulsion Conference, San Diego, CA, July 10-12, 1995.
- e. N. Zhou, A. Krishnan and A.J. Przekwas, "A Numerical Method for Reacting Flows with Multi-Step Stiff Chemical Kinetics," presented at the 31st AIAA/ASME/SAE/ASEE Joint Propulsion Conference, San Diego, CA, July 10-12, 1995.
- f. A. Krishnan, N. Zhou and M. Giridharan, "Transport Phenomena in Supercritical Fluids," presented at 26th AIAA Fluid Dynamics Conference, San Diego, CA, June 19-22, 1995.
- g. N. Zhou and A. Krishnan, "Heat Transfer Characteristics of Supercritical Fluids," presented at Fourth ASME/JSME Thermal Engineering Joint Conference, Hawaii, March 19-24, 1995.
- h. T. Edwards and J. Krieger, "The Thermal Stability of Fuels at 480°C (900°F). Effect of Test Time, Flow Rate and Additives," presented at the 1995 International Gas Turbine Conference and Exposition, 1995.

12.4 Conclusions

In summary, the current Phase II study has resulted in the first commercial CFD code that has advanced models to simulate flow, heat transfer and chemistry in supercritical fluid systems. All of these models have been validated against benchmark experimental data obtained during the study.

The models and code are ready to be applied for the design analysis of complex aircraft fuel systems components. The application of these models will help optimize performance of aircraft thermal management systems.

13. REFERENCES

1. Edwards, T., "USAF Supercritical Hydrocarbon Fuels Interests", AIAA 93-0807, Aerospace Sciences Meeting, Jan. 11-14, 1993.
2. Edwards, T., "Deposition During Vaporization of Jet Fuel in a Heated Tube", AIAA 92-0687, Aerospace Sciences Meeting, Jan. 6-9, 1992.
3. Edwards, T., "Supercritical Fuel Deposition Mechanisms", *Ind. Eng. Chem. Res.*, v. 32, pp. 3117-3122, 1993.
4. Hall, W.B., "Heat Transfer Near the Critical Point", *Advances in Heat Transfer*, pp. I-86, 1971.
5. Hsu, Y.Y., Graham, R.W., Transport Processes in Boiling and Two Phase Systems, Hemisphere Publishing Corporation, Washington, 1976.
6. Hall, W.B., and Jackson, J.D., "Heat Transfer Near the Critical Point", Proceedings of the Sixth Int. Heat Transfer Conference, v. 6, pp. 377-392, 1978.
7. Polyakov, A.F., "Heat Transfer under Supercritical Pressures", *Advances in Heat Transfer*, pp. 1-53, 1991.
8. Carey, V.P., Liquid-Vapor Phase-Change Phenomena, Hemisphere Publishing, 1992.
9. Goldman, K., "Heat Transfer to Supercritical Water at 5000 psi Flowing at High Mass Flow Rates through Round Tubes", *International Developments in Heat Transfer*, pp. 561-568, 1961.
10. Kurganow, V.A., and Kaptilnyi, A.G., "Flow Structure and Turbulent Transport of a Supercritical Pressure Fluid in a Vertical Heated Tube under the Conditions of Mixed Convection", *Experimental Int. J. Heat Mass Transfer*, v. 36, pp. 3383-3392, 1993.
11. Stewart, E., Stewart, P., and Watson, A., "Thermo-Acoustic Oscillations in Forced Convection Heat Transfer to Supercritical Pressure Water", *Int. J. Heat Transfer-Soviet Research*, v. 25, No. 2, 1993.
12. Kreith, F., and Summerfield, M., "Heat Transfer to Water at High Flux Densities With and Without Surface Boiling", *ASME Transactions*, v. 71, 1949, pp. 805-815, 1949.
13. Hines, W.S., and Wolf, H., "Pressure Oscillations Associated with Heat Transfer to Hydrocarbon Fluids at Supercritical Pressures and Temperatures", *ARS Journal*, v. 32, pp. 361-366, 1962.
14. Malkina, L.I., Maksimova, G.P., Kafengaus, N.L., and Fedorov, M.I., Heat

- Transfer-Soviet Research, v. 4, pp. 23-26, 1972.
15. Kalbaliew, F.I., and Verdiev, CH. M., "Heat Transfer to Toluene at Supercritical Pressure", *Heat Transfer Research*, v. 25, no. 2, 1993.
 16. Avva, R.K., Smith, C.E., and Singhal, A.K., "Comparative Study of High and Low Reynolds Number Versions of K- ϵ Models", AIAA 90-0246, Aerospace Sciences Meeting, 1990.
 17. Zhou, N., Krishnan, A., and Przekwas, A.J., "A Numerical Method for Reacting Flow and Multi-Step Stiff Chemical Kinetics," Presented at the 31st AIAA/ASME/SAE/ASEE Joint Propulsion Conference, San Diego, CA., July 10-12, 1995.
 18. Reid, R.C., Prausnitz, J.M., and Poling, B.E., The Properties of Gases & Liquids, 4th edition, McGraw-Hill, New York, 1987.
 19. Rodi, W., "Experience with Two-Layer Models Combining the K- ϵ Model with a One-equation Model Near the Wall", AIAA Paper 91-0216, 1991.
 20. Chein, K.Y., "Predictions of Channel and Boundary-Layer Flows with a Low-Reynolds Number Turbulence Model", *AIAA Journal*, Vol. 20, pp. 33-38, Jan. 1982.
 21. Kays, W.M., and Crawford, M.E., Convective Heat and Mass Transfer, McGraw-Hill, 1980.
 22. Krazinski, J.L., Vanka, S.P., Pearce, J.A., and Roquemore, W.M., "Computational Fluid Dynamics and Chemistry Model for Jet Fuel Thermal Stability", 35th ASME Int. Gas Turbine and Aeroengine Congress Exposition, June 1990.
 23. Katta, V.R., Jones and Roquemore, W.M., "Development of Global Chemistry Model for Jet Fuel Thermal Stability Based on Observations from Static and Flowing Experiments", AGARD Meeting on Fuels and Combustion Technology for Advanced Aircraft Engines, May 1993.
 24. ASHREA Handbook, 1995 Fundamentals, SI ed.
 25. Tevalde and Glickstein, "Heat Transfer and Thermal Stability of Alternate Aircraft Fuels", NAPC-PE-87C, 1983.
 26. Horvath, A.L., Physical Properties of Inorganic Compounds, Crane, New York, 1975.
 27. Laufer, J., "Investigation of Turbulent Flow in a Two-Dimensional Channel", NACA Report 1053, 1951.
 28. Laufer, J., "The Structure of Turbulence in Fully Developed Pipe Flow",

- NACA TN 2954, 1953.
29. Driver, D.M., and Seegmiller, H.J.L., "Features of a Reattaching Turbulent Shear Layer in Divergent Channel Flow", *AIAA Jl.* Vol. 23, No. 2, pp. 163-171, 1985.
 30. Sandborn, V.A., "Recent Measurements in the 180 Degree Turn, Small Radius of Curvature Water Channel", Presented at the 6th SSME CFD Workshop, NASA Marshall Space Flight Center, Huntsville, AL. 1988.
 31. Daily, J.W., and Nece, R.E., "Chamber Dimension Effects on Induced Flow and Frictional Resistance of Enclosed Rotating Disks", *Trans. ASME, Jl. of Basic Eng.*, Vol. 82, pp. 217-232, 1960.
 32. Nishikawa, K., et al., Tech Rep, Kyushu Univ. (In Japanese) vol. 40, p. 986, 1967.
 33. Marteney, P.J., and Spadaccini, L.J., "Thermal Decomposition of Aircraft Fuel", *ASME J. Of Engineering for Gas Turbines and Power*, Vol. 108, pp. 648-653, 1986.

APPENDIX A

SURFACE DEPOSITION DATA

Table A-1. Flowrate at 100 ml/min

Carbon Deposition (μg) per 2-inch section						
<i>Tube number</i>	7/94-5	7/94-6	7/94-7	7/94-8	7/94-10	7/94-11
1	32	24	42.7	12.5	22.9	37.8
2	29.2	18.1	23.7	13.9	11.3	26.2
3	21.9	16	25.6	10.8	9.53	14.2
4	24.5	15.8	19.4	14.5	14.9	19.2
5	1050	286	22	27.9	294	15.7
6	1620	563	23.6	29.4	550	17.6
7	1350	435	16.8	25.9	593	18.2
8	1420	388	43.5	22.1	535	20.5
9	1590	287	33.8	23.7	526	17.6
10	573	119	52.3	17	559	29.9
11	1190	628	189	19.3	478	27
12	219	714	103	18.8	103	32.5
13	3683	1580	286	22.1	374	35.4
14	3800	2060	239	60.2	344	30.5
15	5397	2490	474	120	338	34.4
16	6160	2740	869	202	553	27.4
17	7320	2120	1570	510	1660	20.5
18	5833	1330	1780	614	1540	17.4
19	3781	649	2080	599	2380	19.6
20	2040	267	1780	832	2910	21.3
21	932	121	1930	1430	2380	30.3
22	689	94.3	1680	920	1280	22.4

23	320	78.5	1220	890	1000	28.4
24	204	59	403	544	589	20.6
<i>Tube number</i>	<i>8/94-1</i>	<i>8/94-2</i>	<i>8/94-3</i>	<i>8/94-4</i>	<i>8/94-5</i>	
1	17.9	28	0.219	15.6	18.2	
2	9.93	53.1	19.4	14.2	18.3	
3	10.5	18.2	16	15.6	14	
4	11.7	17.9	58.5	13.1	39	
5	643	765	1670	1110	3000	
6	saved	saved	saved	2840	6200	
7	1000	885	622	2070	4600	
8	615	661	946	2700	2810	
9	747	575	1340	2520	2710	
10	479	511	365	1870	2510	
11	546	1250	222	2210	2490	
12	944	838	166	1470	6440	
13	2120	2070	201	1330	13080	
14	2650	2270	152	1130	13500	
15	2320	saved	548	3370	12980	
16	saved	4267	1510	6570	10160	
17	4203	4622	976	5150	7020	
18	964	4034	541	3350	4820	
19	1750	2820	saved	1320	3550	
20	804	1740	140	375	2660	
21	122	479	129	289	1260	

22	97.7	176	104	216	649	
23	106	150	101	155	385	
24	saved	saved	saved	95.9	193	

Table A-2. Flowrate at 200 ml/min

Carbon Deposition (μg) per 2-inch section				
<i>Tube number</i>	7/94-1	7/94-2	7/94-3	7/94-4
1	13.2	33.9	33.8	26
2	47.1	24.4	19.3	20
3	35.6	27.8	16.7	31.4
4	21.6	21.4	19.4	30.5
5	24.5	80.3	20.6	20.4
6	25.7	309	89.9	17.9
7	23.3	310	150	18.8
8	43	90	305	17.7
9	155	104	394	18.3
10	452	217	531	17.2
11	243	640	126	20.9
12	28.7	140	56.4	17.3
13	31	92.5	42.2	16.8
14	44.2	273	21	18.4
15	62.2	341	26.1	25.2
16	37.4	249	22.6	44.5
17	43.8	256	26.9	23.1
18	50.1	307	29.7	26.7
19	71.1	26.6	42.5	39.7
20	73.5	20.9	68.8	47.3
21	116	23.7	49.9	48.8
22	193	32.8	38	42.8

23	126	56.3	55.9	42
24	87.9	28.2	53.6	55.1
25	175	73.7	56.2	25.9
26	415	29.2	59.9	22
27	770	31.4	73.2	42.7
28	1060	69.6	111	184
29	1820	119	188	342
30	4419	229	340	642
31	6560	450	316	1030
32	8180	591	424	64.8
33	10770	745	564	161
34	11510	1420	871	252
35	8870	2750	1340	809
36	5010	3810	1460	1120
37	4230	3881	1550	432
38	4510	3050	1300	172
39	4580	1930	960	19.6
40	3960	1810	814	19.2
41	2140	1960	704	25.7
42	743	1780	486	27.1
43	389	1430	333	26.2
44	298	1070		26.6
45	140	537		33.9

Table A-3. Flowrate at 300 ml/min

300 ml/min Carbon Deposition (μg) per 2-inch section				
<i>Tube Number</i>	7/94-9		<i>Tube Number</i>	7/94-9
1	43.9		32	14.3
2	114		33	13.3
3	31		34	13.8
4	13.6		35	16.7
5	13.8		36	14.6
6	13.2		37	15.8
7	11.1		38	15.4
8	11.9		39	18.7
9	13		40	14.4
10	14.9		41	20.5
11	13.4		42	19.2
12	13.4		43	20.4
13	14.5		44	18.4
14	30.5		45	21.8
15	16.5		46	24.6
16	15.5		47	27.8
17	20.3		48	31.3
18	19.9		49	77.7
19	19.6		50	23.1
20	16.6		51	21.6
21	23		52	22.1
22	48.1		53	26.8

23	70.6		54	138
24	25.1		55	1850
25	28.3		56	2640
26	26.7		57	3250
27	22.2		58	3830
28	18.9		59	3530
29	19.7		60	2980
30	15		61	3100
31	15.3			

APPENDIX B

EXIT FILTER DEPOSITION DATA

<i>Test Name</i>	<i>Filter</i>	<i>Deposition (μg)</i>	<i>Notes</i>
7/94-1	inlet	533	
	outlet	791	first 5 3/4 hours
	outlet	584	second 4 1/4 hour
7/94-2	inlet	341	
	outlet	724	
7/94-3	There are no filters for this test.		
7/94-4	inlet	483	
	outlet	4300	first 4 1/2 hours
	outlet	4460	second 5 hours
7/94-5	inlet	374	
	outlet	4280	first 5 hours, dirty filter case
	outlet	3660	second 5 hours
7/94-6	inlet	229	
	outlet	1890	
7/94-7	inlet	348	
	outlet	4820	first 7 hours
	outlet	2650	second 3 hours
7/94-8	inlet	480	
	outlet	24260	test ended with pump failure
7/94-9	inlet	838	
	outlet	10590	7 μm filter
7/94-10	inlet	252	
	outlet	1280	

7/94-11	inlet	183	
	outlet	76.7	
8/94-1	inlet	1270	
	outlet	1040	first 5 hours
	outlet	3030	second 3 1/2 hours, power failure
8/94-2	inlet	538	
	outlet	460	first 2 1/2 hours
	outlet	saved	
8/94-3	inlet	893	
	outlet	2290	first 6 hours
	outlet	1360	second 4 hours
8/94-4	inlet	887	
	outlet	1790	first 7 1/2 hours
	outlet	1680	second 5 hours, power failure
8/94-5	inlet	2670	
	outlet	1240	first 4 hours
	outlet	2730	second 10 hours
	outlet	2270	next 6 hours

APPENDIX C
WALL TEMPERATURE DATA

Table C-1. Flowrate at 200 ml/min

Wall Temperatures (°F)						
<i>Distance along tube (in.)</i>	<i>7/94-1</i>	<i>day 2</i>	<i>7/94-2</i>	<i>7/94-3</i>	<i>7/94-4</i>	<i>day 2</i>
5	399	347	573	384	188	185
10	814	821	963	828	538	557
20	883	918	932	939		687
30	806	839	670	673	692	721
40	818	835	885	801	673	699
50	844	858	668	846	481	472
60	915	965	895	899	800	813
70	1002	1140	945	917	609	815*
80	1055	1119	1121	809	569	590
92	820	840	782	921	745	794
92 (fuel)	727	753	683	682	485	497

Table C-2. Flowrate at 300 ml/min

Wall Temperatures (°F)						
<i>Distance along tube (in.)</i>	7/94-9					
6	530					
12	597					
18	713					
24	670					
36	692					
48	740					
60	706					
72	727					
84	751					
96	844					
108	970					
120	834					
124	942					
124(fuel)	671					

Table C-3. Flowrate at 100 ml/min

Wall Temperatures (°F)						
<i>Distance along tube (in.)</i>	7/94-5	<i>day 2</i>	7/94-6	7/94-7	<i>day 2</i>	7/94-8
2.5	372	512	406	338	401	341
5	663	689	763	546	599	673
10	978	997	970	708	736	930
15	1156	1179	1009	746	755	1055
20	1052	1076	1159	765	776	1101
25	915	947	1029	745	743	1062
32.5	943	1012	1026	923	929	1072
40	985	1034	1059	932	931	1145
45	944	941	983	881	904	974
50	1151	1064	1071	853	910	1108
50 (fuel)	750	747	776	513	523	738
<i>Distance along tube (in.)</i>	<i>day 2</i>	7/94-10	7/94-11	8/94-1	<i>day 2</i>	8/94-2
2.5	376	459	402	448	306	
5	687	681	718	532	560	529
10	923	963	977		1102	1001
15	1048	969	1038	951	990	1089
20	1101	911	1038	1174	1202	1317(?)
25	1074	859	1075	1004	1050	914
32.5	1079	952	885	1098	1146	
40	1149	999	1040	974	1038	979

45	979	1083	955			
50	1107	1065	1132	1106	1107	1108
50 (fuel)	761	704	738	740	770	754
<i>Distance along tube (in.)</i>	<i>day 2</i>	<i>8/94-3</i>	<i>day 2</i>	<i>8/94-4</i>	<i>8/94-5</i>	<i>day 3</i>
2.5		397	380	212	393	355
5	531	570	535	451		
10	1025	954	931	940		840
15	1101	1153		954		1007
20	1375(?)	1124	1116	1020	1090	945
25	972	1212	1210	1015	914	1003
32.5	1071	1033	1035	1115	1042	1150
40	1021	1041	1032	1078	1000	1024
45	977	1015	1030	940	1015	999
50	1047	1102	1132	1031	943	946
50 (fuel)	765	785	808		760	800